

# **Characterization of Polymer Nanocomposites based on Layered Double Hydroxide and Carbon Nanotubes**

Vorgelegt von  
M.Sc. in Polymer Science  
Purv J. Purohit  
aus Mumbai, Indien

von der Fakultät III - Prozesswissenschaften  
der Technischen Universität Berlin  
zur Erlangung des akademischen Grades

Doktor der Ingenieurwissenschaften  
Dr.–Ing.

genehmigte Dissertation

Promotionsausschuss:

Vorsitzende: Prof. Dr.–Ing. Claudia Fleck (TU Berlin)

Gutachter: Prof. Dr. rer. nat. Andreas Schönhals (BAM Berlin)

Gutachter: Prof. Dr.–Ing. Manfred H. Wagner (TU Berlin)

Tag der wissenschaftlichen Aussprache: 23<sup>rd</sup> November 2012

Berlin 2012  
D83

***To my Grandparents and my Father***

*.....for being “Mentors” of my Life.*

## Acknowledgements

---

Firstly, I would like to express my sincere gratitude to Prof. Dr. A. Schönhals for his help and guidance throughout my work at BAM. This thesis would not have been completed successfully without him. It was his patience and co-operation that has helped me enrich my scientific knowledge, and also develop as an individual researcher. I will never regret the decision of pursuing my PhD under his guidance. I would like to thank Prof. Dr. M. H. Wagner (TU Berlin) for the encouragement, the general support for carrying out the work outside the university and supervision.

I would like to also take this opportunity to express my sincere thanks to Prof. Dr. M. Hennecke and Prof. Dr. J. Friedrich for their efforts on the organization and administration of my stay at BAM. Also, I would like to thank Ms. G. Otten-Walther and Mr. R. Saling for all the administrative help.

Besides, I would like to convey my regards to all the staff of the group BAM-6.10 and also the administration staff at BAM for helping me in all ways possible. I would also like to thank Mr. B. Audi for taking care that Liquid Nitrogen was always available for the dielectric measurements.

I would like to gratefully acknowledge Prof. Dr. D. Y. Wang (IPF, Dresden) and Prof. Dr. G. Heinrich (IPF, Dresden) for a very successful collaboration and technical support by providing the samples and also any other related information instantly.

A special thanks to PD Dr. A. F. Thünemann, Dr. F. Emmerling for fruitful discussions in X-ray scattering. Also, I would like to thank Ms. S. Rolf for her help with scattering measurements and Mr. D. Neubert for DSC measurements. Also, Prof. Dr. C. Schick and Dr. A. Wurm (University of Rostock) for help with TMDSC measurements.

Last but not the least, I would like to thank my fellow colleagues and friends Maalolan, Kishore, Sanjeeva reddy, Huajie, Alaa, Jesus Sanchez, Christina, Marieke, Mohammad, Kirti, Ranjit for enjoyable discussions between work and also scientific help whenever required. I would like to also thank Frank for his help to scan documents and at times also coffee breaks.

This thesis would not have been a success without the loving support of my Father; my success is the result of his hardwork and patience. I would like to convey my regards to my grandparents (Baa and Dada) and my family, Pratiksha aunt, Pranay uncle, Disha, Kanan for always believing in me. Finally, I would like to thank Veena, for being the moral support and encouragement in times of despair. She was always there to help and support me.

## Abstract

---

Polymer based nanocomposites by melt blending of synthesized ZnAl-Layered Double Hydroxide (ZnAl-LDH) and Polyolefines [Polypropylene (PP) and Polyethylene (PE)] and also Polylactide (PLA) with MgAl-LDH and multi-walled Carbon Nanotubes (MWCNT) were investigated. The LDH was organically modified by using a surfactant sodium dodecylbenzene sulfonate (SDBS) to increase the interlayer spacing of the LDH, so that polymer chains can intercalate the inter layer galleries. Some amount of maleic anhydride grafted PP and PE were incorporated in the nanocomposites based on PP and PE respectively to enable the interaction of the non polar polymers (PP and PE) with the LDH. The resulting morphology was investigated by a combination of Differential Scanning Calorimeter (DSC), Small and Wide-angle X-ray scattering (SAXS and WAXS) and broadband dielectric relaxation spectroscopy (BDS).

In case of LDH based nanocomposites (PP, PE and PLA), the homogeneity of the nanocomposites and the average number of stack size (4 – 7 layers) were determined using scanning micro focus SAXS (BESSY II). DSC investigations of PP and PE based LDH nanocomposites showed a linear decrease in crystallinity as a function of filler concentration. The extrapolation of this decreasing dependence to zero estimates a limiting concentration of 40 wt% and 45 wt% respectively. Above this amount of LDH the crystallinity of the polymers is completely suppressed. This finding is in agreement with WAXS investigations where the area below the crystalline reflections and amorphous halo were calculated and used to estimate the degree of crystallinity. PLA/LDH nanocomposites presented a little different behavior, the crystallinity of the polymer at first increases and then decreases as a function of LDH concentration. In this case the crystallinity will be suppressed at around 15 wt%. The dielectric spectra of the nanocomposites based on PP/LDH and PE/LDH show several relaxation processes which are discussed in detail. The intensity of the dynamic glass transition increases with the concentration of LDH. This is attributed to the increasing concentration of the exchanged anion dodecylbenzene sulfonate (SDBS) which is adsorbed at the LDH layers. Therefore, a detailed analysis of the  $\beta$ -relaxation provides information about the structure and the molecular dynamics in the interfacial region between the LDH layers and the polymer matrix which is otherwise dielectrically invisible (low dipole moment, non-polar). In case of PLA/LDH, three relaxation processes related to dynamic glass transition and one localized fluctuations were identified and analyzed in detail to understand the morphology. For this system, one dynamic glass transition process originates



from the fluctuations of the interfacial molecules, second from the PLA matrix (polar polymer, C=O in the main chain) and the third from segments confined between the intercalated LDH sheets. Additional thermal investigations were carried out for PP/LDH and PLA/LDH samples. The increase in the rigid amorphous fraction (RAF) was observed in both the cases. This is attributed to the polymer molecules which are in close proximity to LDH sheets, as they hinder their mobility. This is analyzed in detail and related to the BDS results. PLA based MWCNT nanocomposites were investigated by BDS as initial result. The findings showed that between 0.5 and 1 wt% of CNT, a percolating network of the nanotubes is formed which leads to DC conductivity. This is due to the high aspect ratio of the CNTs and also the van der Waals interaction between the nanotubes which forms a network leading to conductivity.

## Zusammenfassung

---

Polymer-Nanokomposite hergestellt durch Schmelzmischen von synthetisierten ZnAl-Layered Double Hydroxide (ZnAl-LDH) und Polyolefine (Polypropylen und Polyethylen) sowie auch Polylactid mit MgAl-LDH und multi-walled Carbon Nanotubes (MWCNT) wurden untersucht. Das LDH wurde organisch unter Verwendung des Tensids Natriumdodecylbenzolsulfonat (SDBS) modifiziert, um den Abstand zwischen den Schichten der LDH zu erhöhen, so dass sich die Polymerketten zwischen den Schichten einfügen können. In die PP und PE basieren Nanokomposite wurde eine gewisse Menge an Maleinsäureanhydrid aufgepfropft auf PP bzw. PE eingearbeitet, um die Wechselwirkung der nicht polaren Polymeren (PP und PE) mit dem LDH zu ermöglichen. Die resultierende Morphologie wurde durch eine Kombination von Dynamischer Differenzkalorimetrie (DSC), Klein- und Weitwinkelröntgenstreuung (SAXS und WAXS) und dielektrischer Relaxationsspektroskopie (BDS) untersucht.

Im Falle der LDH Nanokomposite (PP, PE und PLA) wurde die Homogenität der Nanokomposite und die durchschnittliche Anzahl der „Stapelgröße“ (4 - 7 Schichten) mittels scanning micro Focus SAXS (BESSY II) untersucht. DSC Untersuchungen auf PP und PE basierenden LDH Nanokompositen zeigten eine lineare Abnahme des Kristallinitätsgrades als Funktion der Füllstoffkonzentration. Die Extrapolation dieser Abhängigkeit auf null ergibt eine grenz Konzentration von 40 Gew.% bzw. 45 Gew.%. Für hohe Konzentration an LDH ist die Kristallinität der Polymere vollständig unterdrückt. Dieses Ergebnis ist in Übereinstimmung mit den WAXS-Untersuchungen, wobei die Fläche unterhalb der kristallinen Reflexe und dem amorphen „Halo“ berechnet wurde, um den Grad der Kristallinität zu berechnen.

Die PLA / LDH Nanokomposite zeigten ein etwas anderes Verhalten. Die Kristallinität des Polymers wächst zunächst mit steigendem LDH Konzentration an und nimmt dann als Funktion der LDH Konzentration ab. Bei diesen System wird die Kristallinität bei etwa 15 Gew.% unterdrückt. Die dielektrischen Spektren der Nanokomposite auf PP / LDH und PE / LDH Basis weisen mehrere Relaxationsprozesse auf, die im Detail diskutiert werden. Die Intensität der dynamischen Glas temperatur ( $\beta$ -Relaxation) steigt mit der Konzentration von LDH an. Dies ist auf die Erhöhung der Konzentration des ausgetauschten Anions Dodecylbenzolsulfonat (SDBS) zurückzuführen, welches an den LDH Schichten adsorbiert wird. Daher bietet eine detaillierte Analyse der  $\beta$ -Relaxation Informationen über die Struktur

und die molekulare Dynamik in der Grenzregion zwischen den LDH Schichten und der Polymer-Matrix, welche sonst dielektrisch unsichtbar ist (niedriges Dipolmoment).

Im Falle von PLA / LDH konnten zwei Relaxationsprozesse zurückzuführen auf den dynamischen Glasübergang und lokalisierte Fluktuationen identifiziert werden. Diese wurden im Detail analysiert, um die Morphologie zu verstehen. Zusätzliche thermische Untersuchungen wurden für PP / LDH und PLA / LDH Proben durchgeführt. Der Anstieg in der starren amorphen Fraktion (RAF) wurde in beiden Fällen beobachtet. Dies ist auf die Polymermoleküle, die in unmittelbarer Nähe der LDH-Platten sind zurückzuführen, da diese sie in ihrer Mobilität behindern. Eine detaillierte Analyse und eine Korrelation mit den BDS Ergebnissen werden durchgeführt.

Die PLA basierten MWCNT Nanokomposite wurden zunächst mit BDS untersucht. Die Ergebnisse zeigten, dass zwischen 0,5 und 1 Gew.% CNT ein perkoliertes Netzwerk von Nanoröhren gebildet wird, welches zur Gleichstrom-Leitfähigkeit des Systems führt. Dies kann durch das hohe Aspektverhältnis (Länge zu Durchmesser) der CNTs sowie durch die van-der-Waals-Wechselwirkung zwischen den Nanoröhren erklärt werden, welche ein Netzwerk ausbilden und so zu Leitfähigkeit führen.

# Table of Contents

---

**Acknowledgements**

**Abstract**

**Zusammenfassung**

<b>1. Introduction</b>	1
1.1 Polymer Composites	1
1.2 Polymer Nanocomposites	1
1.3 Structure of the Thesis	5
<b>2. Theoretical Background</b>	7
2.1 Nanofillers	7
2.1.1 Layered Double Hydroxide	7
2.1.2 Carbon Nanotubes	9
2.2 Polymer based LDH and CNT Nanocomposites	10
2.3 Relaxation phenomena in polymers	11
2.3.1 Glass Transition	11
2.3.2 Molecular dynamics in polymers	14
2.4 Broadband Dielectric Relaxation Spectroscopy	17
2.4.1 Static Polarization	18
2.4.2 Dielectric Relaxation	21
2.4.3 Analyzing dielectric spectra	24
2.5 Small- and Wide- angle X-ray Scattering	29
2.5.1 Spatial correlation function	30
2.5.2 Amorphous halo subtraction in WAXS	31
2.5.3 BESSY	32
2.6 Differential Scanning Calorimetry	33
<b>3. Experimental Techniques</b>	35
3.1 Dielectric relaxation spectroscopy	35
3.1.1 Dielectric measurement techniques	35
3.1.2 Fitting Haviriliak-Negami function	36
3.2 Small-and Wide-angle X-ray Scattering	37
3.3 Differential Scanning Calorimetry	37
3.4 Transmission Electron Microscopy	38

<b>4. Materials</b>	39
4.1 Nanofillers	39
4.1.1 Layered Double Hydroxide	39
4.1.2 Carbon Nanotubes	43
4.2 Matrix Polymers	43
4.2.1 Polyethylene (PE)	43
4.2.2 Polypropylene (PP)	46
4.2.3 Polylactide (PLA)	44
4.3 Sample Preparation	51
4.3.1 Nanocomposites based on LDH	51
4.3.2 Nanocomposites based on carbon nanotubes	53
4.4 Sample Information	53
<b>5. Nanocomposites based on PP/ZnAl-LDH</b>	54
5.1 Homogeneity and SAXS analysis	54
5.2 Investigations using DSC and WAXS	58
5.3 Investigations using BDS	62
5.4 Extended thermal investigations using TMDSC	77
<b>6. Nanocomposites based on PE/ZnAl-LDH</b>	83
6.1 Homogeneity and SAXS analysis of the nanocomposites	83
6.2 DSC and WAXS Investigations	85
6.3 BDS results and analysis	89
<b>7. Polylactide based Nanocomposites</b>	98
7.1 MgAl-LDH based Nanocomposites	98
7.1.1 Homogeneity and SAXS Investigations	98
7.1.2 Thermal Investigations	99
7.1.3 Investigations employing BDS	105
7.2 Carbon Nanotubes based Nanocomposites	111
7.2.1 Preliminary BDS Investigations	112
<b>8. Summary and Outlook</b>	116
<b>References</b>	120
<b>Appendix</b>	127
List of Symbols, Constants and Abbreviations	127

This thesis is concerned with the structure-property relationships of Polymer Based Nanocomposites using Layered Double Hydroxides (LDH) and Carbon Nanotubes (CNT). This chapter highlights what are polymer based nanocomposites, motivation of the work and structure of the thesis.

Materials with specially designed properties for different applications are becoming more and more important. Various attempts have been made to develop organic-inorganic hybrid polymer materials for a wide range of applications. In order to accomplish various requirements, a tailor-made material design is necessary, with control over bulk and surface characteristics.

## 1.1 Polymer Composites

Conventional composites are prepared by mixing of polymer with different type of reinforcing fibres (e.g., glass, aramid, carbon etc.) or particulate solids (e.g., talc, calcium carbonate, mica, carbon black etc.). This is done by different ways such as reacting the polymer and the filler (chemical mixing), physical mixing, with an aid of a compatibilizer etc. Such materials exhibit improved mechanical properties, higher heat deflection temperatures while maintaining their ease of process ability.<sup>1</sup> Fibre based composites were first developed in 1940's mainly for military applications. From then they have been widely used to replace metals in various applications such as construction, automobile, consumer products etc.

However, improvement of properties requires addition of high amounts of the reinforcing material ( $\geq 10$ -wt%). Moreover, after a certain concentration of the filler, the properties such as mechanical either reach a plateau or even decrease. This is also associated with loss of optical clarity, reduction in surface gloss etc. So to replace conventional macro-composites, materials with addition of nano-sized fillers are a field of academic and industrial research.

## 1.2 Polymer Nanocomposites

In past few years the advancement in synthesis and characterization of materials on atomic scale has increased interest in nano sized materials. The combination of composites and nano sized materials form the so called *Polymer Nanocomposites*.

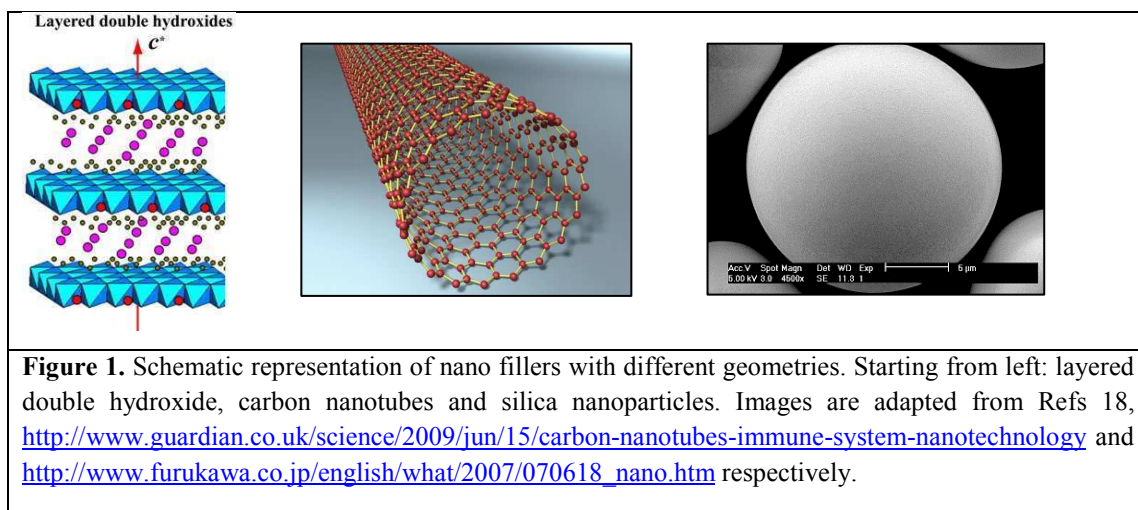
Polymer based nanocomposites are gaining an increasing interest because of the substantial improvements in material properties such as gas and solvent barrier, toughness, mechanical

strength, flame retardancy etc. as compared to micro or macro scaled composites.<sup>2-8</sup> The reasons behind these property improvements are the small size of the filler particles, their homogenous dispersion on the nanoscale in the polymeric matrix and thus the length scale of interaction with the polymer segments. Also due to the small size of the particles they have a high surface to volume ratio which results in a high volume fraction of an interface area between the polymer matrix and the nanoparticle.<sup>9</sup> So, even a small amount of the nanofiller (2 wt%) can improve the properties of the polymer by several orders of magnitude. The structure, like the packing density and/or the molecular mobility of the segments in that interface can be quite different from those in the matrix polymer.<sup>10-13</sup> Therefore, the interfacial area between the polymer and the nano-filler is crucial for the properties of the whole composite. The challenge is to characterize this interface and deduce the resulting morphology and the properties of the nanocomposites. This can be investigated by BDS which is used extensively for the work mentioned in this thesis.

The understanding of the basic physical origin of these tremendous property changes remains in its infancy. This is partly due to the complexity of polymer nanocomposites, which require re-considering the meaning of some basic polymer physics terms and principles, and partly by the lack of experimental data. In addition to detailed knowledge of molecular structure of the polymer matrix, the theory also requires a sufficient description of particle dispersion, self-assembly phenomena, particle-chain interactions and nanocomposite preparation processes.<sup>14</sup> An increasing number of review articles are published on structure-property relationships of polymer nanocomposites. (For instance see the references 14-16). The properties, nanostructure etc. not only depends on the chemical nature of the components but also on the synergy of the system.<sup>17</sup>

Depending upon the geometry of the nano fillers, they can be classified into three categories:

- 1) One-dimensional (1D), e.g., carbon nanotubes.
- 2) Two-dimensional (2D), e.g., silicate clays, layered double hydroxide.
- 3) Three-dimensional (3D), e.g., silica, metal nanoparticles.

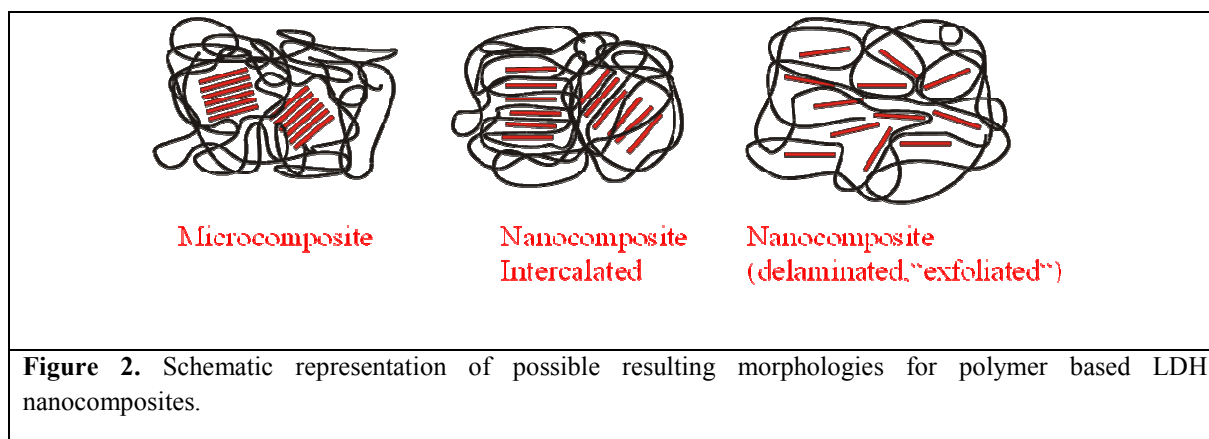


In this thesis, the results discussed are extensively of nanocomposites based on a relatively new class of inorganic material layered double hydroxide (LDH). However, some preliminary results of carbon nanotubes (MWCNT) based nanocomposites are also presented. LDH's are mixed metal hydroxides of di- and trivalent metal ions crystallized in the form similar to mineral brucite or magnesium hydroxide (MH) with the incorporation of interlayer anionic species. The specialty of LDHs as nanofiller is their thermal decomposition behavior, which makes them potential flame retardants for polymers. The LDH materials can be interesting to industry as they combine the features of conventional metal hydroxide-type fillers, like magnesium hydroxide (MH), with the layered silicate type of nanofillers, like montmorillonite. The major area of interest in this regard is the role of LDH materials as potential non-halogenated, non-toxic flame retardant for polymer matrices. The state of the dispersion of nanofillers in the polymeric matrix often has a large impact on the properties of polymeric materials. Unfortunately, it often has proved difficult to form uniform and stable dispersions of nanofillers in polymer matrices resulting in large variations in properties for systems of the same composition prepared using different techniques.

Polymer nanocomposites are formed by either polymerizing a monomer in the presence of the filler (in-situ polymerization) or by allowing the polymer to diffuse in between the LDH from a solution or a melt (solution or melt intercalation). Often shear is used to disperse the LDH into the polymer matrix. Nanocomposites in which the LDH layers are completely delaminated and are dispersed in the polymer matrix are said to be exfoliated nanocomposites. Intercalated nanocomposites are those in which the polymer chains reside



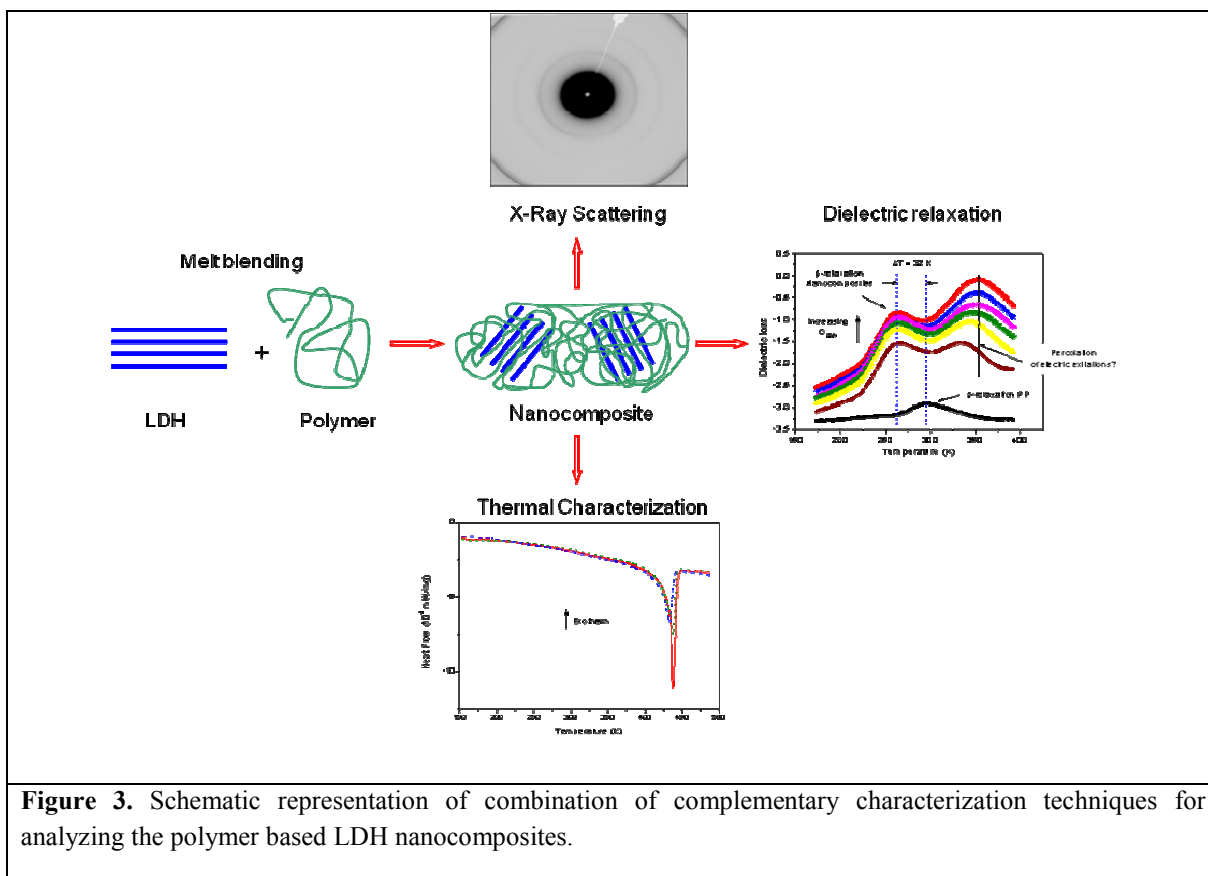
in between the LDH galleries, while preserving the layered structure. And systems with completely phase separated morphology are termed as Microcomposite.



Exfoliated nanocomposites show enhancements in properties and are typically obtained by smart in-situ polymerization techniques. However, melt intercalation is a preferred route as it utilizes existing compounding equipment such as twin-screw extruders to prepare nanocomposites.

The resulting structure and properties for a given polymer can vary depending upon the geometry of the nanofillers. It also depends upon a number of other parameters such as type of interaction between the polymer and the nanofiller, processing conditions, method of analysis or characterization etc. So, it is necessary to establish the structure-property relationships of polymer based nanocomposites for an in-depth understanding. A combination of various characterization techniques to study the molecular structure of macromolecular systems has attracted lots of attention recently.<sup>19</sup>

In this contribution, nanocomposites based on polypropylene, polyethylene and polylactide with LDH are investigated by a combination of differential scanning calorimetry (DSC), small- and wide- angle X-ray scattering (SAXS & WAXS) and broadband dielectric spectroscopy (BDS) for the first time. The approach of combining the different characterization techniques involving a variety of different probes will provide different windows to characterize the structure property relationship of this particular system. But this unique combination will be in turn helpful to establish standard models for structure property relationships of polymer based nanocomposites in general. Figure 3 shows the schematic representation of various characterization techniques employed for analyzing the nanocomposites.



### 1.3 Structure of the Thesis

This thesis is divided into various chapters to put forth the understanding of polymer based LDH nanocomposites from different aspects. As mentioned above, the different characterization techniques would focus on different characteristics of the system studied.

Scanning microfocus SAXS (BESSY II of the Helmholtz Centre Berlin for Materials and Energy) investigations determine the structure of the particles (intercalated, exfoliated, stack size etc.). DSC is employed for the thermal characterization of the nanocomposites, to determine the melting temperature and the crystallization & melting enthalpies. Dielectric spectroscopy (BDS) is employed to study the molecular dynamics of the polymers, for instance. The molecular motions in polymers which are dependent on the morphology occur on different time scales due to the complex structure of the polymer. BDS can be used to investigate these motions on a broad time and temperature range making it a probe for studying the structure of the polymer systems.

Chapter 2 gives the theoretical background and fundamental understanding of the the nanofiller – layered double hydroxide, the molecular dynamics (glass transition phenomena) and the characterization techniques.

Chapter 3 discusses in detail the experimental methods, and Chapter 4 deals with the materials used (different types of LDH and matrix polymers) and the basic findings related to it.

Chapter 5 and 6 report the experimental findings of Polypropylene (PP) based ZnAl-LDH nanocomposites and Polyethylene (PE) based ZnAl-LDH nanocomposites respectively.

Chapter 7 focuses on the results obtained for Polylactide (PLA) based MgAl-LDH nanocomposites and discusses some initial analysis of PLA based carbon nanotubes (MWCNT) nanocomposites. Also, a brief comparison of nanofiller geometry dependence on the properties of PLA is presented.

Chapter 8 gives a full length summary of the structure-property relationships of the various nanocomposites studied.

This chapter deals with the fundamental understanding of layered double hydroxide (LDH) and its advantages along with carbon nanotubes. Moreover, a brief description about the polymer based LDH and carbon nanotubes nanocomposites is given by highlighting some important literature and work done in the past. Theoretical background of glass transition, broadband dielectric spectroscopy and X-ray scattering is also described briefly.

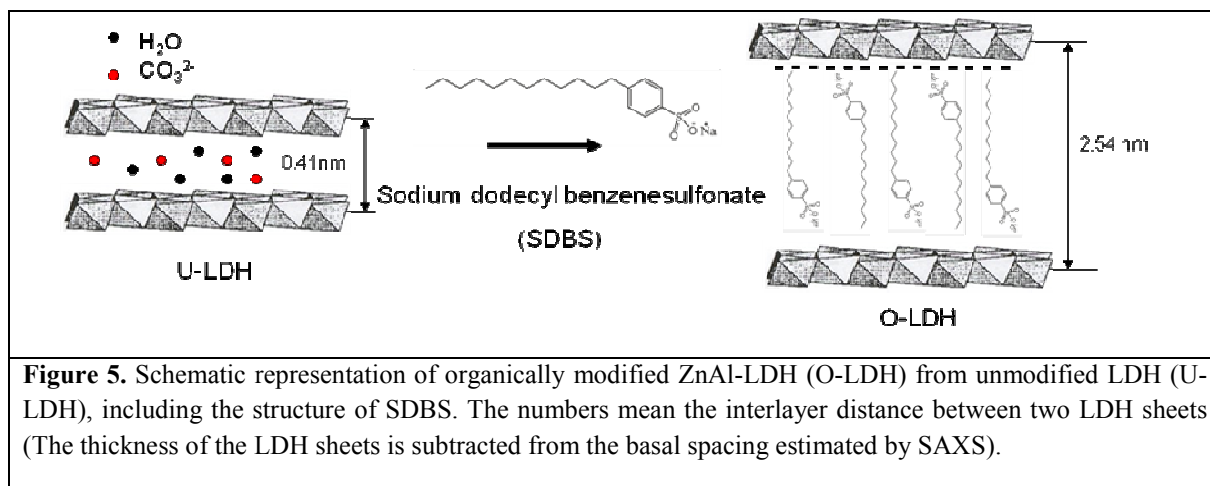
## **2.1 Nanofillers**

### **2.1.1 Layered Double Hydroxide<sup>20</sup>**

Layered double hydroxides are anionic clays whose structure is based on brucite-like layers ( $\text{Mg}(\text{OH})_2$ ).<sup>20</sup> In the latter case each magnesium cation is octahedrally surrounded by hydroxyl groups. An isomorphous substitution of  $\text{Mg}^{2+}$  by a trivalent cation or by a combination of other divalent or trivalent cations occurs in the LDHs. Therefore the layers become charged and anions between the layers are required to balance the charge. LDH can be represented by the general formula  $[\text{M}^{\text{II}}_{1-x} \text{M}^{\text{III}}_x (\text{OH})_2]^{x+} \cdot [(\text{A}^{n-})_{x/n} \cdot m\text{H}_2\text{O}]^{x-}$  where  $\text{M}^{\text{II}}$  and  $\text{M}^{\text{III}}$  are the divalent and trivalent metal cations respectively, and A is the interlayer anion. Examples of divalent ions are  $\text{Mg}^{2+}$ ,  $\text{Ni}^{2+}$  and  $\text{Zn}^{2+}$  and for the trivalent ions are commonly used  $\text{Al}^{3+}$ ,  $\text{Cr}^{3+}$ ,  $\text{Fe}^{3+}$  and  $\text{Co}^{3+}$ . For the present case the LDH material is fully synthetic where the metal cations are  $\text{Zn}^{2+}$  and  $\text{Al}^{3+}$ .

The structure of LDHs can best be explained by drawing analogy with the structural features of the metal hydroxide layers in mineral brucite or simply the MH crystal. A schematic representation comparing the brucite and the LDH structure is shown in Figure 4.





Xu et al. explained how the SDBS increase the interlayer distance by means of a structure where the alkyl tails of the SDBS face in an antiparallel way to each other (see Figure 5).<sup>21</sup> The intercalation of polymer chains establishes three different types of interactions: polymer – surfactant, surfactant – LDH surface and polymer – LDH surface. The stabilization of the structure relies on the interlayer structure as it was already discussed and the interaction of the polymer and the surface. To increase this interaction compatibilizers are added, e.g. in polyolefins is generally used a polymer grafted with maleic anhydride (MA).<sup>22</sup> MA ensures the occurrences of hydrophilic interactions between the surface and the polymer.

### 2.1.2 Carbon Nanotubes

A Carbon Nanotube is a tube-shaped material, made of carbon, having a diameter measuring on the nanometer scale. The graphite layer appears somewhat like a rolled-up chicken wire with a continuous unbroken hexagonal mesh and carbon molecules at the apexes of the hexagons.<sup>23</sup> Carbon Nanotubes have many structures, differing in length, thickness, and in the type of helicity and number of layers. Although they are formed from essentially the same graphite sheet, their electrical characteristics differ depending on these variations, acting either as metals or as semiconductors. As a group, Carbon Nanotubes typically have diameters ranging from <1 nm up to 50 nm.<sup>24</sup> Their lengths are typically several microns, but recent advancements have made the nanotubes much longer, in centimeters.

They are classified depending on their structure as:

- 1) Single-walled nanotubes (SWNT)
- 2) Double-walled nanotubes (DWNT)
- 3) Mutli-walled nanotubes (MWNT)

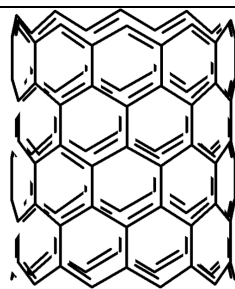


**Figure 6.** Schematic view of a multi-walled carbon nanotube.

Carbon nanotubes are nanofillers with a very high potential in different industrial applications, e.g. for static dissipative or conductive parts in automotive or electronic industries. For the effective use of carbon nanotubes (CNTs) an excellent distribution and dispersion is an essential precondition. The properties of CNT like nanotube type (single-, double-, multiwalled), length, diameter, bulk density, and waviness are dependent on the CNT synthesis conditions, e.g. catalyst, temperature of synthesis, and the method used.<sup>25</sup> The purity and functional groups on the surface of the CNTs as well as mainly their entanglements and strength of agglomerates influence the dispersability of CNTs in different media. In addition, due to strong van der Waals forces CNTs tend to agglomerate. Ultrasonication of CNT dispersions is a common tool used to break up CNT agglomerates in solution based processing techniques. In case of melt compounding, the shear forces experienced during processing helps the dispersion of the nanotubes in the polymer matrix. This is achieved by suitable processing parameters such as temperature, screw speed, time of residence and concentration of the CNTs.

## 2.2 Polymer based LDH and CNT Nanocomposites

In chapter 1, the concept of polymer based nanocomposites is discussed. Other than LDH and CNT, various types of fillers are employed for the successful preparation of polymer-based nanocomposites. Amongst the well-known nanofillers are layered silicates,<sup>2,6,26-28</sup> metal nanoparticles,<sup>29</sup> carbon nanotubes<sup>30-32</sup> and polyhedral oligomeric silsesquioxanes (POSS®)<sup>33-37</sup>.

In order to establish the structure-property relationships, various characterization techniques such as X-ray scattering,<sup>38</sup> dielectric spectroscopy,<sup>13,22,39-44</sup> rheology,<sup>45</sup> microscopy, Fourier transform infrared spectroscopy<sup>46</sup> differential scanning calorimetry<sup>47</sup> etc. have been employed. Dielectric spectroscopy is gaining importance to study the nanocomposites.

Besides the review articles mentioned<sup>14-16</sup>, there are a number of research articles available in the literature reporting the properties of polymer based nanocomposites with LDH as nanofiller. For instance, Kotal et al. studied the thermal properties of polyurethane nanocomposites based on LDH as nanofiller.<sup>48</sup> Costa et al. synthesized and characterized polyethylene based MgAl-LDH nanocomposites using various characterization techniques.<sup>49</sup> Lee et al. investigated the thermal, rheological and mechanical properties of layered double hydroxide/poly(ethylene terephthalate) nanocomposites.<sup>50</sup>

Similarly, in case of nanocomposites based on CNT, from 1994, when Ajayan et al. first incorporate CNT in an epoxy matrix,<sup>51</sup> till now, CNT have been used as fillers in all the available polymer matrices, aiming mainly to improve their mechanical and electrical properties, as well as their thermal stability.<sup>52,53,149</sup>

For the preparation of polymer based LDH and CNT nanocomposites, most of the time melt blending technique is employed as it is of industry interest. The description about the preparation method and its parameters for the nanocomposites employed for this thesis is given in detail in chapter 3. As discussed earlier, LDH have proved to improve flame retardancy of the polymer, CNTs have helped improve the thermal and electrical properties in general.

## **2.3 Relaxation phenomena in Polymers**

### **2.3.1 Glass transition**

Glass transition temperature is regarded as one of the most important parameter in the property of glassy materials and therefore soft matter physics. It is considered to be an important property in case of polymer-based materials, as it relates to the morphology and segmental mobility of the polymer matrix.



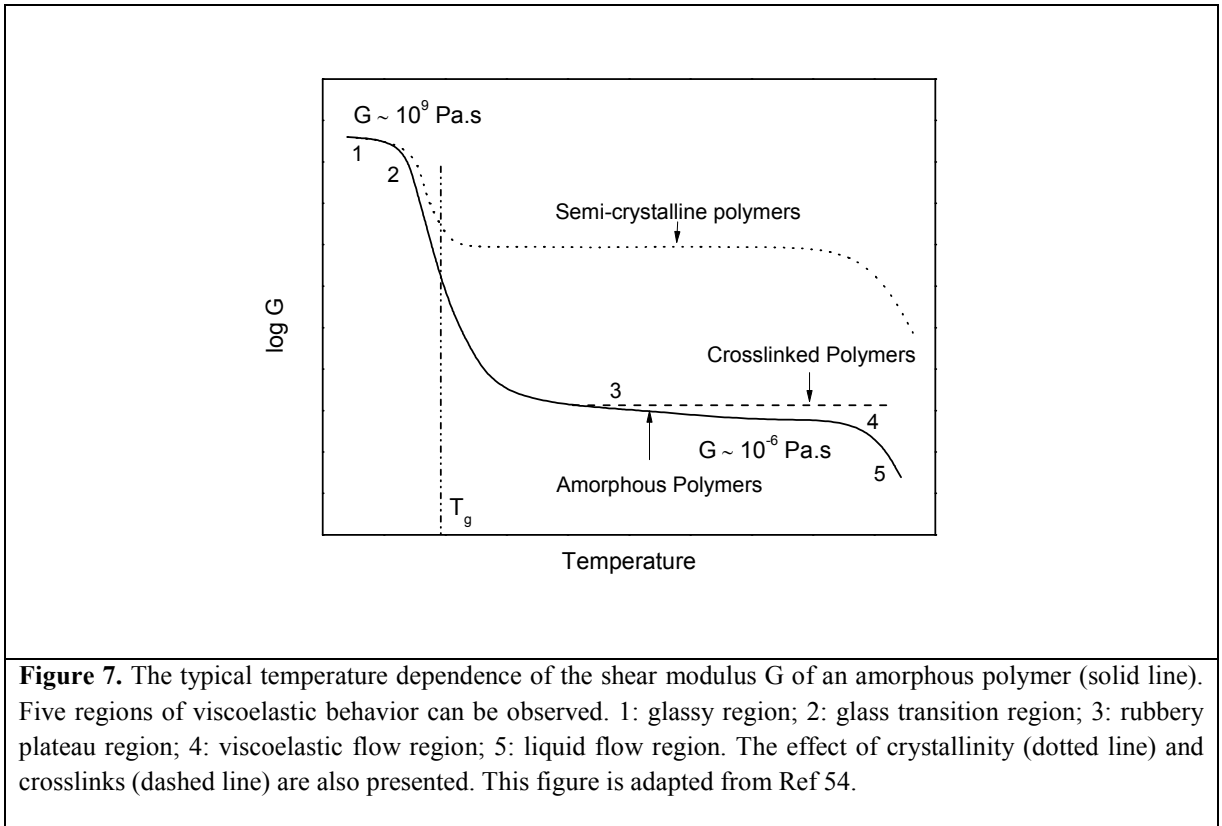
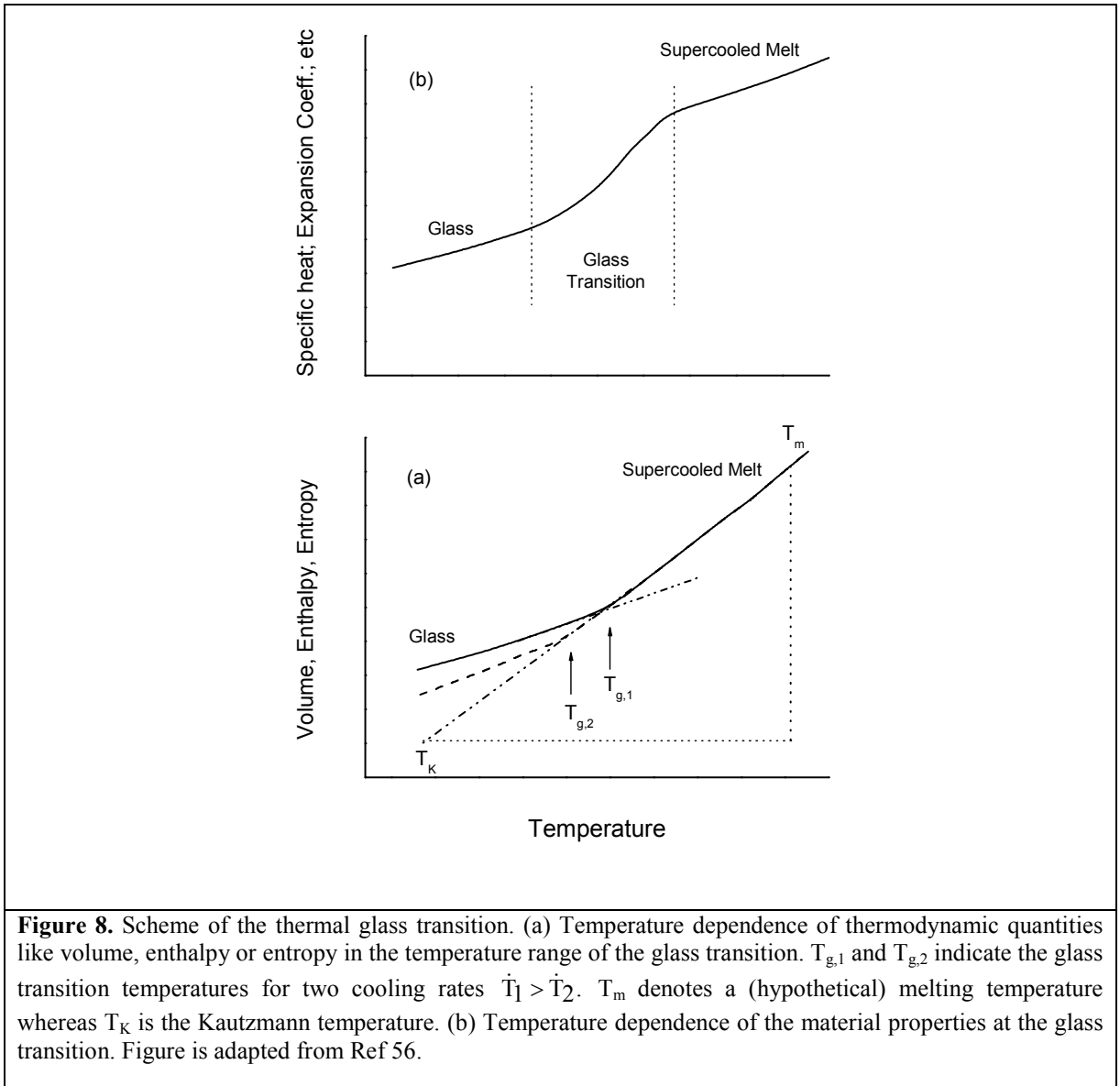


**Figure 7.** The typical temperature dependence of the shear modulus  $G$  of an amorphous polymer (solid line). Five regions of viscoelastic behavior can be observed. 1: glassy region; 2: glass transition region; 3: rubbery plateau region; 4: viscoelastic flow region; 5: liquid flow region. The effect of crystallinity (dotted line) and crosslinks (dashed line) are also presented. This figure is adapted from Ref 54.

When an amorphous polymer is heated from its glassy state, it is observed that the shear modulus decreases by a factor of  $10^3$  within a small temperature range of 20-30 K (Figure 7). From this step-like change a (dynamic) glass transition temperature  $T_g$  can be estimated which corresponds for low measuring frequencies to the value which can be measured by calorimeter. In practice the material becomes more soft and flexible. This phenomenon is called the ‘glass transition’.<sup>54</sup> It is observed in all of glassy materials, including amorphous and semi-crystalline polymers. The glass transition is characterized by the glass transition temperature ( $T_g$ ). One widely used method is Differential Scanning Calorimetry (DSC) and its characteristic frequency is ca.  $10^{-2} \text{ Hz}$ <sup>55</sup> depending on the cooling or heating rate.



If a glass-forming material cools down with a constant rate, a typical behaviour is observed for the temperature dependence of characteristic thermodynamic quantities like volume  $V$ , enthalpy  $H$  etc. (see Figure 8). If temperature is decreased and crystallization can be avoided around the glass transition temperature  $T_g$ , well defined changes in the slopes of the temperature dependence of the volume or enthalpy take place. In parallel, step-like changes in the materials properties like the specific heat  $C_p = (\partial H / \partial T)_p$  or the thermal expansion coefficient  $\alpha = (1/V)(\partial V / \partial T)_p$  are observed (see Figure 8). Above  $T_g$ , the state of the polymer is called “supercooled” whereas below  $T_g$  the supercooled polymeric melt becomes a glass (glassy state). If one extrapolates the temperature dependence of the entropy linearly below  $T_g$ , at a certain temperature  $T_K$ , the entropy of the “extrapolated” supercooled melt

will become lower than that of the corresponding (hypothetic) crystal (see Figure 8). This is known as Kauzmann paradox.<sup>57</sup> To resolve the Kauzmann paradox, a phase transition of second order is suggested to appear at  $T_2$  with  $T_2 \approx T_K$  which cannot be observed experimentally due to the glass transition. For polymers, Gibbs and DiMarzio developed a lattice model which can be analytically solved and predicts a phase transition at  $T_2$ .<sup>58-62</sup>

One has to note that  $T_g$  is a dynamic property and so its value changes as a function of frequency and time scale of measurement. The glass transition temperature can be determined by other methods such as Dynamical-Mechanical Analysis (DMA),<sup>63</sup> light<sup>64</sup> and neutron scattering,<sup>65</sup> Nuclear Magnetic Resonance (NMR)<sup>66</sup> and Broadband Dielectric Relaxation Spectroscopy (BDS).<sup>67</sup>

### 2.3.2 Molecular Dynamics of Polymers

Assuming that the potential barrier of the molecular fluctuation is temperature independent, the simplest case of molecular fluctuation is described by jumps of segments in a double minimum potential model. The frequency-dependent fluctuation in a polymer material is determined by the dynamic equilibrium of two neighboring sub-states and is described by the Arrhenius function (Eq. 1).

The molecular mobility within a polymer is due to localized and segmental fluctuations as well as collective motions of the whole polymer chain. Most amorphous polymers show a slow  $\beta$  relaxation process (Figure 9) which is observed as a peak in the dielectric loss. This corresponds to rotation of side groups or other intramolecular fluctuations in the polymer and is observed at higher frequencies (or lower temperatures). It can be identified as broad and symmetric peaks for instance in dielectric loss spectra. The temperature dependence of its relaxation rate  $f_p$  is linear on a log scale and described by the Arrhenius function.

$f_p(T) = f_\infty \exp\left(\frac{-E_A}{RT}\right)$	<b>(1)</b>
--	------------

In Eq. 1,  $R$  is the ideal gas constant (8.314 J/K.mol) and  $E_A$  is the activation energy of the  $\beta$  relaxation.  $f_\infty$  is the pre-exponential factor.

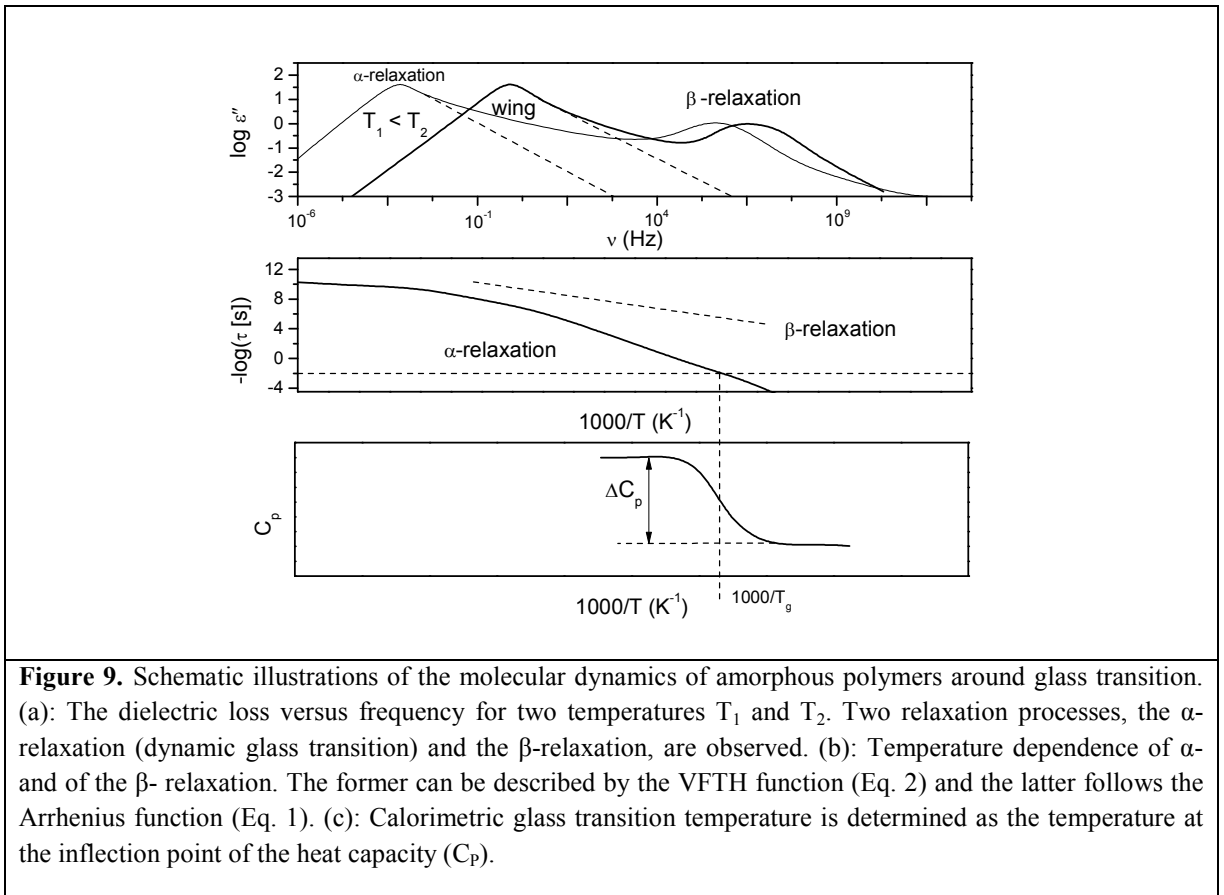
From Figure 9, the dynamic glass transition ( $\alpha$  relaxation) which is related to the glass transition is observed at lower frequencies and shifts to higher frequencies with increasing temperature. This process is assigned to cooperative segmental motion. The temperature dependence of their mean relaxation rates is curved and well described by the VFTH

equation (Eq. 2). Extrapolating this dependence to lower frequency gives the  $T_g$  from calorimetric measurement (Figure 9).

The prominent feature of the glass transition process is the rapid increase of the characteristic relaxation time  $\tau$  of the relaxation function. In general, the characteristic time or mean relaxation rate  $f_p$  of the relaxation increases as the temperature decreases. This effect is described by the Vogel-Fulcher-Tammann-Hesse function,<sup>68-70</sup>

$\frac{1}{\tau(T)} = f_p(T) = f_\infty \exp\left(\frac{-A_0}{T - T_0}\right)$	(2)
---	-----

In Eq. 2,  $A_0$  is a constant,  $f_\infty$  is a pre-exponential factor and  $T_0$  is the ideal glass transition temperature, and empirically its value is about 30-70 K lower than  $T_g$  measured by calorimetric or viscometric techniques. The VFTH equation describes the experimental phenomenon that increasing/decreasing the characteristic frequency or time of measurement shifts the glass transition process to higher/lower temperatures.



The present nomenclature of  $\alpha$ - and  $\beta$ -relaxation is used for amorphous polymers, however for semi-crystalline polymers a different convention is employed in the literature and is described in Chapters 5 and 6.

Glassy materials are classified in fragile or strong depending how much the dependence of the relaxation rate versus the temperature deviates from the Arrhenius-type behavior.<sup>71,72</sup> Materials are called "fragile" if their  $f_p(T)$  dependence deviates strongly from an Arrhenius-type behaviour and "strong" if  $f_p(T)$  is close to the latter. From Eq. 2, a parameter  $D$  called fragility strength can be defined as,

$D = \frac{A_0}{T_0}$	<b>(3)</b>
-----------------------	------------

Different theories and models have been developed to describe the glass transition based on thermodynamic and kinetic considerations. The two most common models are the Free Volume and The Cooperative Approach.<sup>73</sup> The concept of Free Volume Model was initially developed to describe the molecular motions of polymers based on the presence of vacancies. These vacancies are named as 'Free Volume'.<sup>74</sup> Doolittle and Cohen<sup>75,76</sup> attributed the free volume as the result of inefficient packing of disordered polymer chains. For a polymeric segment to move from its present position to an adjacent site, a critical free volume must first exist.<sup>54</sup>

#### ***Cooperative approach***

Adam and Gibbs explained the temperature dependence of the relaxation of glass-forming polymers by the "temperature-dependent cooperatively rearrange region (CRR)".<sup>90</sup> According to the model, the CRR is a subsystem of the polymer matrix, which can be rearranged into another configuration independent from its environment. Assuming  $z^*(T)$  is the number of segments in the CRR, the following relationship for the characteristic relaxation time  $\tau$  is obtained:

$\frac{1}{\tau(T)} \sim \exp\left(-\frac{z^*(T)\Delta E}{k_B T}\right)$	<b>(4)</b>
---	------------

$\Delta E$  is a free energy barrier for a conformational change of a segment.  $z^*(T)$  can be expressed by the total configurational entropy  $S_c(T)/(Nk_B \ln 2)$ , where  $N$  is the total number of particles and  $k_B \ln 2$  the minimum entropy of a CRR assuming a two-state model. Eq. 4 cannot

determine the co-operative length and so in this fluctuation approach; Donth developed a formula to determine the size of a CRR ( $\xi$ ).

$\xi^3 = \frac{k_B T_g^2 \Delta(1/C_p)}{\rho(\delta T)^2}$	<b>(5)</b>
--	------------

$k_B$  is the Boltzmann constant =  $1.38 \times 10^{-23} \text{ m}^2 \text{ kg/ s}^2 \text{ K}$ ,  $\rho$  is the density and  $\delta T$  is the temperature fluctuation of a CRR at  $T_g$  which can be taken from DSC experiments. Donth estimated that to have a signature of a glass transition, the spatial extent of these regions should be in the order of 1 to 3 nm.<sup>77-81</sup>

The subsequent works by Donth<sup>77</sup> showed that the cooperative length  $\xi$  of the CRR varies with the temperature as

$\xi \approx \frac{1}{(T - T_0)^{2/3}}$	<b>(6)</b>
---	------------

## 2.4 Broadband Dielectric Relaxation Spectroscopy (BDS)<sup>67</sup>

Dielectric spectroscopy measures the dielectric permittivity as a function of frequency and temperature. The frequency at which the measurement can be done ranges from  $\mu\text{Hz}$  to  $\text{THz}$ . It is used to study the molecular dynamics of the polymers, for instance. The molecular motions in polymers which are dependent on the morphology occur on different time scales due to the complex structure of the polymer. Dielectric spectroscopy can be used to investigate these motions on a broad time and temperature range making it a probe for studying the structure of the polymer systems. Some fundamentals related to this technique are discussed here.

### 2.4.1 General considerations

For small electric field strengths  $E$ , the dependence of the dielectric displacement  $D$  on  $E$  is given by,

$$\mathbf{D} = \epsilon^* \epsilon_0 \mathbf{E} \quad (7)$$

$\epsilon^*$  is the complex dielectric function and  $\epsilon_0$  is the permittivity in vacuum which is  $8.854 \times 10^{-12} \text{ As/Vm}$ .

$$\epsilon^* = \epsilon' - i\epsilon'' \quad (8)$$

$\epsilon'$  = Real part and  $\epsilon''$  = Imaginary part of the complex dielectric function. The response of materials to an electric field depends on the frequency and is retarded if time dependent processes are taking place in the sample. This means that there is in general a time shift between the outer electric field and dielectric displacement and for this reason permittivity is treated as complex dielectric function.

Dielectric spectroscopy is sensitive to dipoles and when an electric field is applied, these dipoles get oriented. The polarization  $\mathbf{P}$  due to this is given by,

$$\mathbf{P} = \mathbf{D} - \epsilon_0 \mathbf{E} = (\epsilon^* - 1) \epsilon_0 \mathbf{E} \quad (9)$$

Here,  $(\epsilon^* - 1) = \chi$  is called the dielectric susceptibility of the material.

In an ideal dielectric, there exist only bound charges (electrons, ions) which can be displaced from their equilibrium positions until the electric field force and the oppositely acting elastic force are equal. This phenomenon is called displacement polarization or induced polarization ( $\mathbf{P}_\infty$ , Eq. 10) (electronic or ionic polarization). Electronic polarization is one such example for induced polarization where the negative electron cloud of an atom (molecule) is shifted to the positive nucleus. It occurs on a time scale of  $10^{-12}$  s. Atomic polarization occurs at longer time scale and it is observed when an agglomeration of positive and negative ions is deformed under the force of applied electric field. Electronic and atomic polarizations are resonant processes.

Many molecules have a permanent dipole moment  $\mu$  which can be oriented by an electrical field. So the macroscopic polarization  $\mathbf{P}$  can be related to the dipole moment as:

$\mathbf{P} = \frac{1}{V} \sum \mu_i + \mathbf{P}_\infty = \frac{N}{V} \langle \mu \rangle + \mathbf{P}_\infty$	<b>(10)</b>
---	-------------

Where,  $N/V$  denotes the number density of dipoles in the system and  $\langle \mu \rangle$  the mean dipole moment. If the system contains different kinds of dipoles one has to sum up over all kinds.

In the case, if time dependent processes are taking place then,  $\epsilon^*$  is time or frequency dependent. When an electric field is applied, a part of the permanent dipoles get oriented in the direction of the field; this is termed as orientation polarization. In the following section, the static case ( $t \rightarrow \infty$ ,  $\omega \rightarrow 0$ ) is discussed first and then the dielectric relaxation will be introduced.

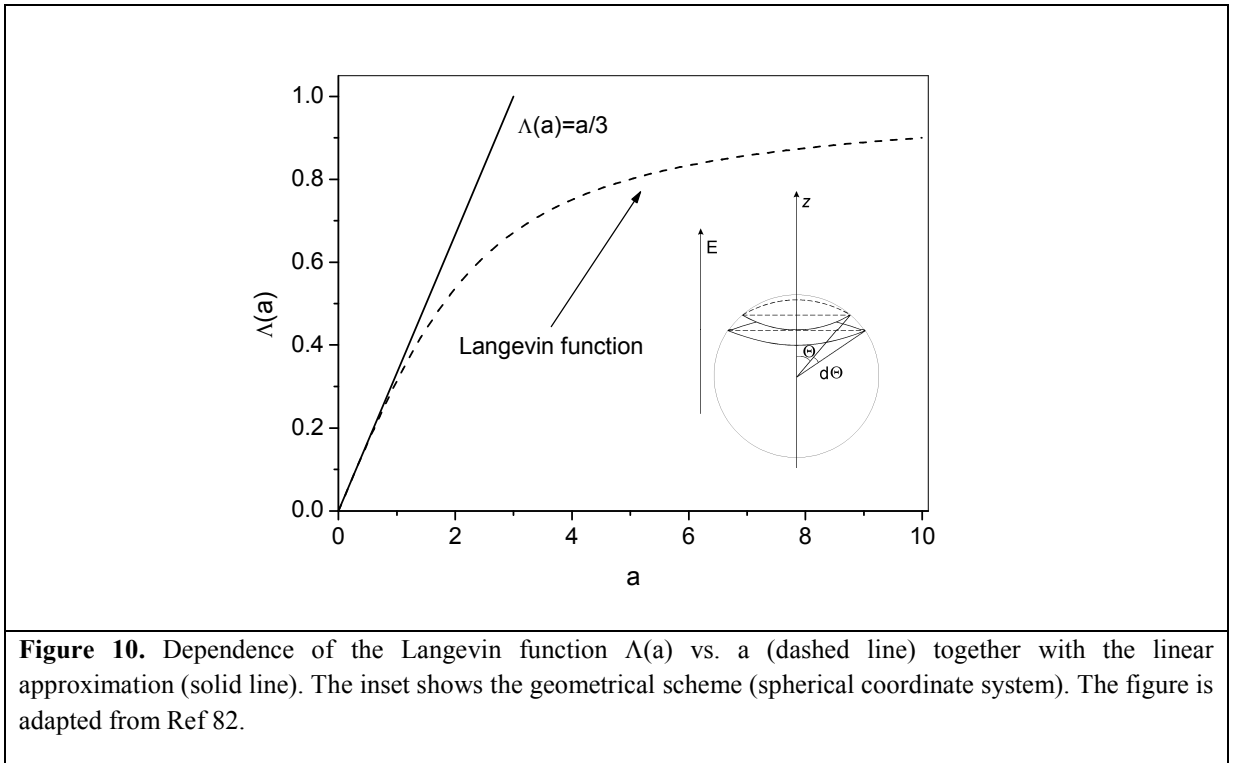
#### 2.4.1.1 Static Polarization

Assuming that the dipoles in a material do not interact with each other and the local electrical field  $E_{loc}$  at the location of the dipole is equal to the outer electrical field the mean

value of the dipole moment is given only by the counterbalance of the thermal energy and the interaction energy  $W$  of a dipole with the electric field given by  $W = -\boldsymbol{\mu} \cdot \mathbf{E}$ . According to Boltzmann statistics one gets,

$\langle \boldsymbol{\mu} \rangle = \frac{\int \boldsymbol{\mu} \exp\left(\frac{\boldsymbol{\mu} \cdot \mathbf{E}}{k_B T}\right) d\Omega}{\int \exp\left(\frac{\boldsymbol{\mu} \cdot \mathbf{E}}{k_B T}\right) d\Omega}$	<b>(11)</b>
---	-------------

where  $T$  is temperature,  $k_B$  Boltzmann constant and  $d\Omega$  the differential space angle. The factor  $\exp\left(\frac{\boldsymbol{\mu} \cdot \mathbf{E}}{k_B T}\right) d\Omega$  gives the probability that the dipole moment vector has an orientation between  $\Omega$  and  $\Omega + d\Omega$ . Only the dipole moment component which is parallel to the direction of the outer electric field contributes to the polarization.



Therefore, the interaction energy is given by  $W = -\mu E \cos\theta$  where  $\theta$  is the angle between the orientation of the dipole moment and the electrical field (see inset Figure 10). So Eq. 11 simplifies to,



$\langle \mu \rangle = \frac{\int_0^\pi \mu \cos \theta \exp\left(\frac{\mu E \cos \theta}{kT}\right) \frac{1}{2} \sin \theta d\theta}{\int_0^\pi \exp\left(\frac{\mu E \cos \theta}{kT}\right) \frac{1}{2} \sin \theta d\theta}$	(12)
---	------

The term  $\frac{1}{2} \sin \theta$  corresponds to components of the space angle in  $\theta$  direction. With  $x = (\mu E \cos \theta) / (kT)$  and  $a = (\mu E) / (k_B T)$  Eq. 12 can be rewritten as:

$\langle \cos \theta \rangle = \frac{\frac{1}{a} \frac{\int_{-a}^a x \exp(x) dx}{\int_{-a}^a \exp(x) dx}}{\frac{\exp(a) + \exp(-a)}{\exp(a) - \exp(-a)} - \frac{1}{a}} = \Lambda(a)$	(13)
--	------

where  $\Lambda(a)$  is the Langevin function. The dependence of  $\Lambda$  on  $a$  is given in Figure 10. For small values of interaction energy of a dipole with the electric field (field strengths  $|E| \leq 10^6$  V/m) compared to the thermal energy  $\Lambda(a) \approx a/3$  holds. Therefore Eq. 13 reduces to,

$\langle \mu \rangle = \frac{\mu^2}{3k_B T} E$	(14)
--	------

Inserting Eq. 14 into Eq. 10 yields,

$\mathbf{P} = \frac{\mu^2}{3k_B T} \frac{N}{V} \mathbf{E}$	(15)
--	------

and with the aid of Eq. 9, the contribution of the orientation polarization to the dielectric function can be calculated as,

$\varepsilon_s - \varepsilon_\infty = \frac{1}{3\varepsilon_0} \frac{\mu^2}{k_B T} \frac{N}{V}$	(16)
---	------

where,  $\varepsilon_s = \lim_{\omega \rightarrow 0} \varepsilon'(\omega)$ .  $\varepsilon_\infty = \lim_{\omega \rightarrow \infty} \varepsilon'(\omega)$  covers all the contributions to the dielectric function which are due to electronic and atomic polarization  $\mathbf{P}_\infty$  in the optical frequency range. Eq. 16 considers the two assumptions 1) the dipoles do not interact with each other and 2) the local field effects (shielding effect) i. e. the polarization of the neighboring molecules

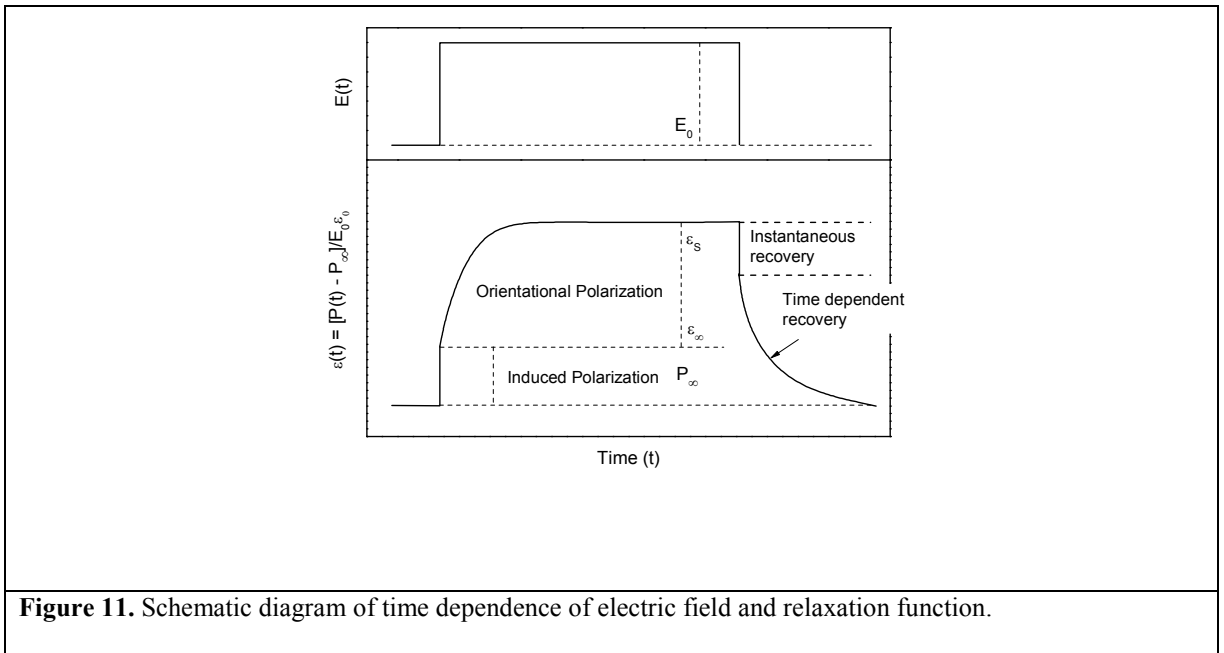
does not affect the electric field of the dipole under consideration. To counter these two effects, Onsager and Kirkwood/Fröhlich modified the Eq. 16,<sup>82</sup>

$\epsilon_s - \epsilon_\infty = \frac{1}{3\epsilon_0} Fg \frac{\mu^2}{k_B T} \frac{N}{V}$	<b>(17)</b>
---	-------------

here, F is the Onsager factor to account for the shielding effect whereas, g is the Kirkwood/Fröhlich correlation factor for interacting dipoles. The g-factor can be smaller or greater than 1, depending on the molecules having tendency to orient anti-parallel or parallel.

### 2.4.2 Dielectric Relaxation

The response of orientation polarization is retarded; this is due to the fact that molecular dipoles are attached to other molecules. When an alternating electric field is applied, at lower frequencies the molecular dipoles fluctuate with same frequencies as of applied field. At higher frequencies the dipoles cannot follow the applied frequencies of the field. Between these two phenomenons, the relaxation process occurs. The onset of such a phenomenon is termed as dielectric relaxation and the characteristic time of such a relaxation process is called the relaxation time  $\tau$ .



The dielectric relaxation can be described by the linear response theory, linking an external perturbation and the response of the system. In general as a simple case, the time dependent electric field  $E(t)$  is the perturbation which is considered as a step change and the time

dependent polarization  $P(t)$  is the response. When the electric field is shut down, there occurs an instantaneous recovery after which the process is time dependent (see Figure 11).

The time dependent dielectric function,  $\varepsilon(t)$  can be measured by the time dependent response followed of an instantaneous electric field change,

$$dE(t)/dt = E_0 \delta(t) \quad (18)$$

$\delta(t)$  is the Dirac function and the corresponding dielectric function is  $\varepsilon(t) = [P(t) - P_\infty]/E_0 \varepsilon_0$  see Figure 11. For a more complicated case then a step like change,  $P(t)$  is given by,

$$P(t) = P_\infty + \varepsilon_0 \int_{-\infty}^t \varepsilon(t-t') \frac{dE(t')}{dt'} dt' \quad (19)$$

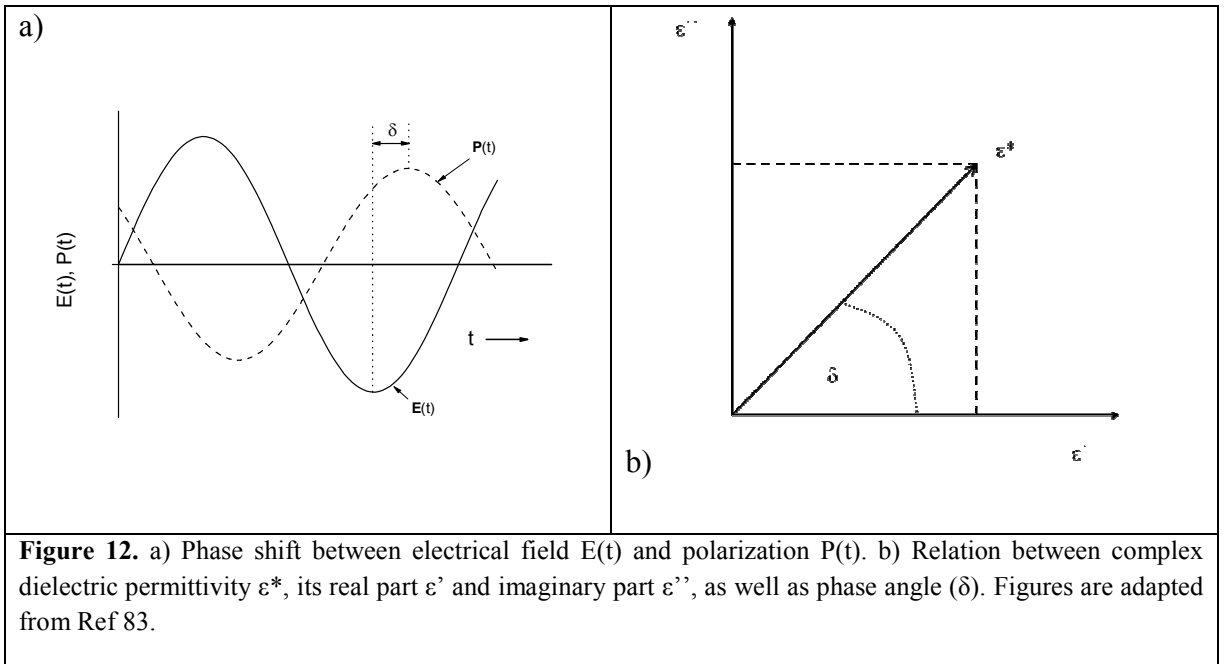
If a stationary periodic disturbance  $E(t) = E_0 \exp(-i\omega t)$  is applied to the system there occurs a phase shift between the electric field and the polarization given by  $\delta$ .  $\omega$  is the angular frequency ( $\omega = 2\pi f$ ), Eq. 19 is transformed to

$P(\omega) = \varepsilon_0 [(\varepsilon^*(\omega) - 1) E(\omega)]$ with $\varepsilon^*(\omega) = \varepsilon'(\omega) - i\varepsilon''(\omega)$	<b>(20)</b>
--	-------------

The relationship of  $\varepsilon^*(\omega)$  to the time dependent dielectric function  $\varepsilon(t)$  is given by,

$\varepsilon^* = \varepsilon_\infty - \int_0^\infty \frac{d\varepsilon(t)}{dt} \exp(-i\omega t) dt$	<b>(21)</b>
---	-------------

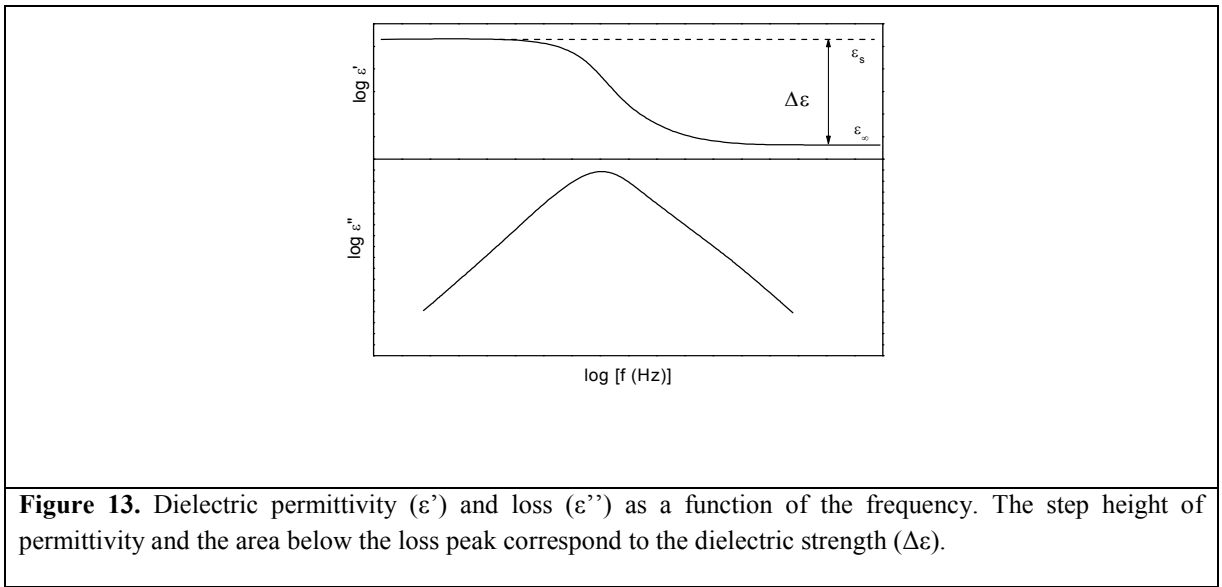
Eq. 21 is a one sided Fourier transformation.



The tangent of the phase angle  $\delta$ , also termed as dissipation factor can be given by,

$\tan \delta = \frac{\varepsilon''}{\varepsilon'}$	<b>(22)</b>
--	-------------

For scientific investigations, however, dielectric properties should be characterized by  $\varepsilon'$  and  $\varepsilon''$ , since they have defined physical significance.  $\varepsilon'(\omega)$  has a step like decrease with increasing frequency corresponding to energy stored reversibly, and  $\varepsilon''(\omega)$  shows a peak corresponding to energy dissipated during one cycle. So, the terms are called dielectric storage and dielectric loss, respectively.



Here,  $\varepsilon_s$  and  $\varepsilon_\infty$  correspond to static and infinite permittivity, respectively. The difference between the two is called the Dielectric Strength ( $\Delta\varepsilon$ ),

$$\Delta\varepsilon = \varepsilon_s - \varepsilon_\infty \quad (23)$$

The Kramer Kronig relation indicates that both the real and imaginary part of the complex dielectric functions contains equivalent information on the relaxation process.<sup>82</sup> The dielectric strength  $\Delta\varepsilon$  is estimated as:

$\Delta\varepsilon = \frac{2}{\pi} \int_0^\infty \varepsilon''(\omega) d(\ln \omega)$	<b>(24)</b>
---	-------------

There also exist free charge carriers in the material along with the dipoles. Under the influence of electric field, these charge carriers can move through the sample and cause conductivity in the material. In addition, due to phase separation creating phase boundaries the moving charge carriers can be blocked at the internal phase boundaries which get polarized and are termed as Maxwell Wagner Sillars (MWS) Polarization.

The relaxation processes are frequency and temperature dependent and occur on a broad time scale. For the analysis of these relaxation peaks a few generalized models were developed. These models are fitted to the data obtained by dielectric measurements.

### 2.4.3 Analyzing Dielectric Spectra

#### 2.4.3.1 Debye Relaxation

The simplest ansatz to calculate the time dependence of dielectric behavior was given by Debye.<sup>84</sup> The theory is based on the assumption that change of polarization is proportional to its actual value.

$$\frac{d\mathbf{P}(t)}{dt} = -\frac{1}{\tau_D} \mathbf{P}(t) \quad (25)$$

$\tau_D$  is the characteristic relaxation time. Solving Eq. 25 gives,

$\mathbf{P}(t) = \mathbf{P}(0) \exp\left(-\frac{t}{\tau_D}\right)$	<b>(26)</b>
--	-------------

Hence, the time dependent function  $\varepsilon(t)$  is proportional to an exponential decay given by,

$\varepsilon(t) \propto \exp\left[-\frac{t}{\tau_D}\right]$	<b>(27)</b>
---	-------------

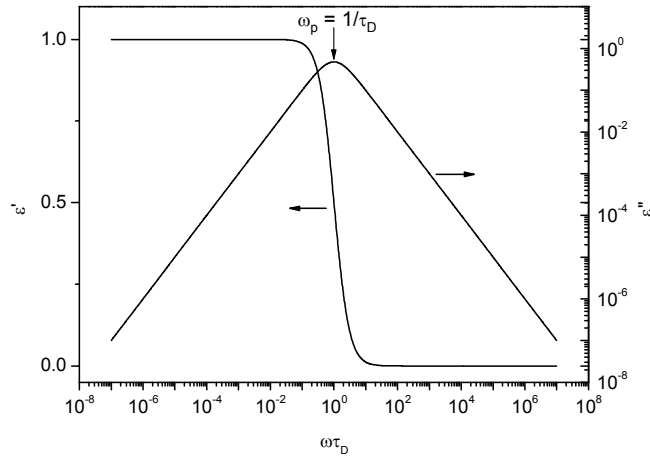


**Figure 14.** Schematic relaxation process observed by permittivity ( $\epsilon'$ ) and dielectric loss ( $\epsilon''$ ), logarithmic scale) according to the Debye model, for  $\tau_D = 1$ s and  $\Delta\epsilon = 1$ .

For complex dielectric function  $\epsilon^*(\omega)$ ,

$$\epsilon^*(\omega) = \epsilon'(\omega) - i\epsilon''(\omega) = \epsilon_\infty + \frac{\Delta\epsilon}{1 + i\omega\tau_D} \quad (28)$$

From the maximum position of the dielectric loss, the mean relaxation rate  $f_p$  related to the mean relaxation time of the dipoles can be determined.

#### 2.4.3.2 Non-Debye Relaxation (Evaluation in frequency domain)

Eq. 25 gives the expression of a Debye relaxation process, which is valid for the orientation of a small rigid dilute dipole system and cannot be applied to polymeric systems. This is due to the fact that polymer materials are quite complex systems. For an isolated polymer molecule, a large number of atoms are covalently bonded together. Therefore, the dynamic relaxation of the polymer occurs on a broad time and temperature scales. Experimentally, the dielectric spectra of polymer materials are always asymmetric and broader than the prediction given by Eq. 25.

The Cole-Cole function<sup>85</sup> describes a symmetric broadening of the time distribution over which the relaxation occurs, where  $\beta$  ( $0 < \beta \leq 1$ ) value characterizes the symmetric broadening of relaxation peaks (dielectric loss) and  $\tau_{CC}$  is the characteristic relaxation time.

$$\varepsilon_{CC}^*(\omega) = \varepsilon_{\infty} + \frac{\Delta\varepsilon}{1 + (i\omega\tau_{CC})^{\beta}} \quad (29)$$

The Cole-Davidson function<sup>86</sup> describes the asymmetry of the relaxation (dielectric loss), where  $\tau_{CD}$  is the characteristic relaxation time. The parameter  $\gamma$  ( $0 < \gamma \leq 1$ ) is introduced to describe the asymmetric broadening of a relaxation peak.

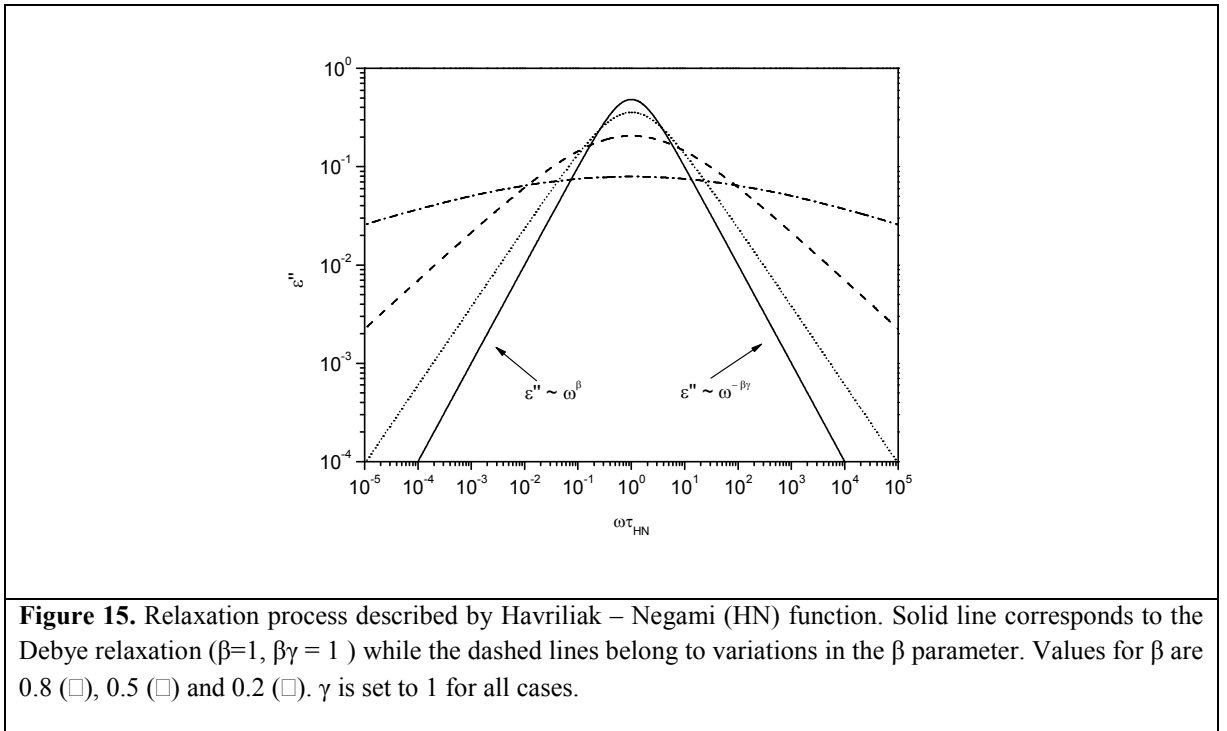
$$\varepsilon_{CD}^*(\omega) = \varepsilon_{\infty} + \frac{\Delta\varepsilon}{[1 + (i\omega\tau_{CD})^{\gamma}]^{\beta}} \quad (30)$$

By combining these two functions, a more general function was introduced by Havriliak and Negami called the Havriliak-Negami (HN)<sup>87-89</sup> function, where  $\tau_{HN}$  is the characteristic relaxation time.

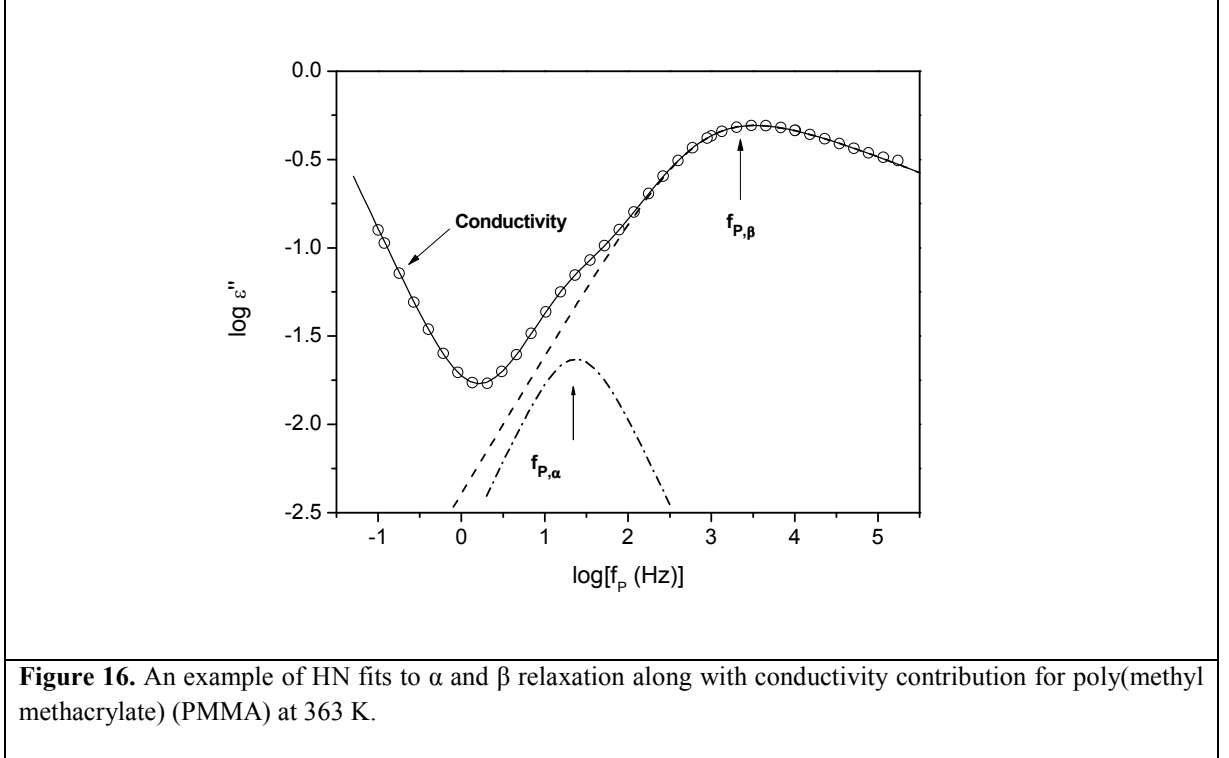
$$\varepsilon_{HN}^*(\omega) = \varepsilon_{\infty} + \frac{\Delta\varepsilon}{[1 + (i\omega\tau_{HN})^{\beta}]^{\gamma}} \quad (31)$$

The HN function has four parameters.  $\Delta\varepsilon$  and  $\tau_{HN}$  are the dielectric strength and characteristic relaxation time respectively.  $\beta$  and  $\gamma$  ( $0 < \beta, \beta\gamma \leq 1$ ) are parameters determining the shape of the relaxation spectra. The impacts of changing  $\beta$  on the shape  $\varepsilon''$  is shown in Figure 15.

Figure 16 gives an example of HN fits to the dielectric spectrum in the frequency domain.



Conduction effects are treated in the usual way by adding a contribution  $\frac{\sigma_0}{\varepsilon_0 (2\pi f)^s}$  to the dielectric loss, where  $\sigma_0$  is related to the dc conductivity of the sample and  $\varepsilon_0$  is the dielectric permittivity of vacuum. The parameter  $s$  ( $0 < s \leq 1$ ) describes for  $s < 1$  non-Ohmic effects in the conductivity. For details see Ref 90.



#### 2.4.3.3 Evaluation in temperature domain

In some cases the evaluation cannot be applied in the frequency domain of the dielectric spectra due to constraints resulting from the conductivity in the samples or crystallization which narrows the range where the Havriliak – Negami analysis can be performed. This limits the analysis of the obtained spectra and it is required to change the representation of the spectra. For any measured frequency, the dielectric loss is plotted against the temperature.<sup>91</sup>

Dielectric loss is described as a superposition of Gaussian functions with a conductivity contribution. It is assumed that the conductivity follows the VFTH equation, and the exponent  $s$  that describes the behavior of the conductivity depends linearly on the temperature. The dielectric loss in this case can be represented as:



$$\varepsilon'' = \sum_{i=1}^n a_i \exp\left(\frac{-(T - T_i^{\max})^2}{w_i}\right) + \left(\frac{\sigma_{\infty}}{\varepsilon_0 \omega^{(mT+n)}} \exp\left(\frac{-A}{T - T_0}\right)\right) + \lambda \quad (32)$$

where  $a_i$  and  $T_i^{\max}$  are the amplitude and maximum position of the Gaussian functions;  $w_i$  corresponds to the width of the peak when it has decreased to  $1/e$  of the maximum;  $\sigma_{\infty}$ ,  $A$  and  $T_0$  are the parameters that describe the conductivity dependence of the VFTH equation;  $m$  and  $n$  are used to describe the linear dependence of the conductivity exponent on the temperature;  $\omega$  is the angular frequency of the electric field and  $\lambda$  is an offset.

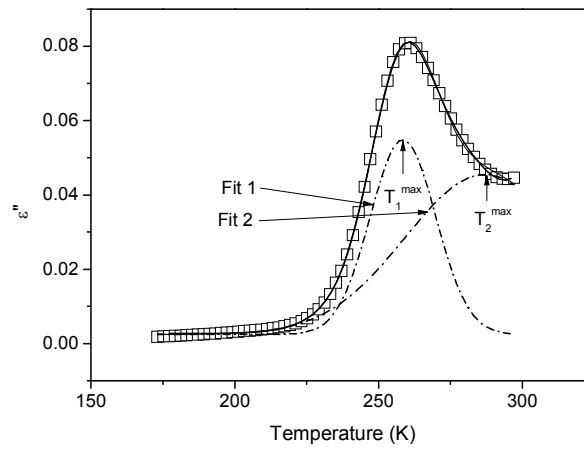
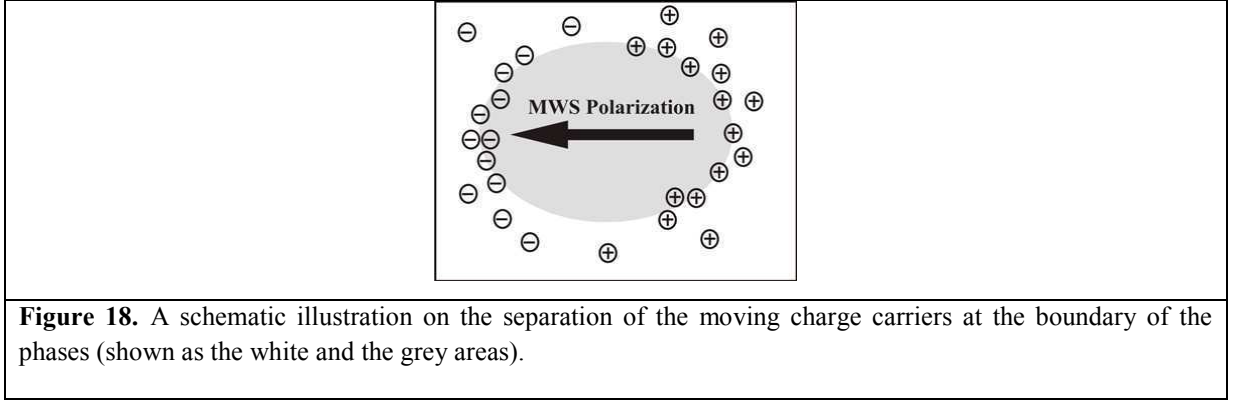


**Figure 17.** An example of evaluation in the temperature domain of dielectric data for polypropylene nanocomposite at  $2.9 \cdot 10^5$  Hz. The solid line is a combined fit of two functions (Eq. 32) and dashed-dotted lines show individual contribution of two processes.  $T_1^{\max}$  and  $T_2^{\max}$  are the maximum position of the Gaussian functions for the individual processes.

Figure 17 shows an example of evaluation of the dielectric spectrum in the temperature domain for polypropylene nanocomposite using Eq. 32. From the fit of the peaks, the  $T^{\max}$  positions are determined. The corresponding measured dielectric frequency is then plotted against inverse of the  $T^{\max}$  values to get the relaxation map.

#### 2.4.3.4 Maxwell Wagner Sillars (MWS) Polarization

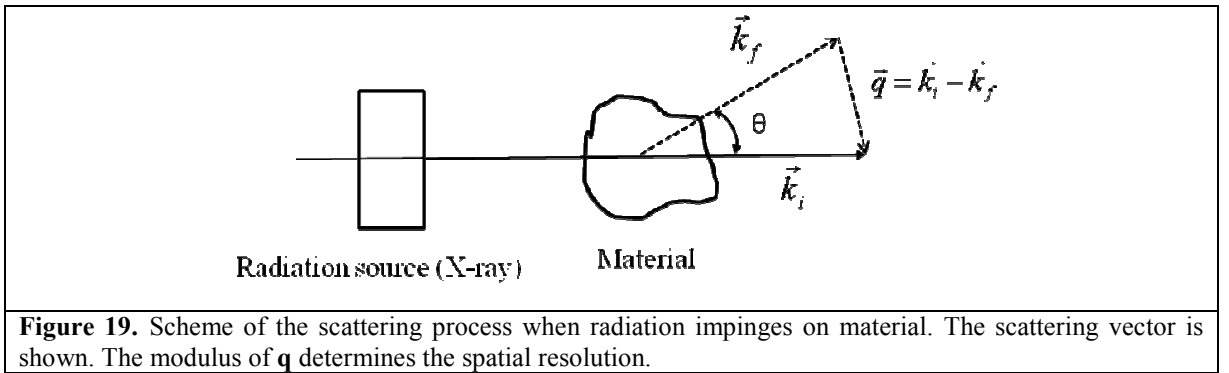
At the interface of two materials, charge carriers can be blocked and give rise to MWS polarization. Such an effect leads to separation of charges and results in an additional contribution to polarization.



The Maxwell-Wagner-Sillars polarization is widely observed in heterogeneous systems such as colloids, phase separated, biological and liquid crystalline materials. The contribution to dielectric storage is several magnitudes larger than orientation polarization due to charge separation over a distance. This effect is generally accepted besides others as a characteristic signature of MWS polarization.<sup>92-94</sup>

## 2.5 X-ray Scattering (Small- and Wide- angle)

Scattering methods are important tools in polymer, colloid and interface science. When radiation interacts with a sample, scattering or diffraction occurs due to spatial and temporal correlations in the sample.<sup>95</sup>



The geometry of a typical scattering experiment is given in Figure 19, where,  $\mathbf{k}_f$  is the scattered and  $\mathbf{k}_i$  is the incident vector, and  $\theta$  is the angle between the two vectors known as scattering angle. The difference between the two vectors is termed as scattering vector  $\mathbf{q}$  and is a reciprocal of the spatial correlation length. The most important quantity is the norm of the so-called scattering vector given by:

$q = \frac{4\pi n}{\lambda} \sin \frac{\theta}{2}$	<b>(33)</b>
--	-------------

$\lambda$  is the wavelength of the radiation used,  $n$  is the refractive index in the scattering medium and  $\theta$  is the scattering angle. The choice of the appropriate scattering method depends on the relationship length-scale to  $q$ -range, since  $q$  determines the spatial resolution of a scattering experiment ( $d = 2\pi/q$ ). The wavelength  $\lambda$  thus determines the spatial resolution of the equipment which is inversely proportional to the scattering vector  $q$ . At low  $q$  values the overall size and shape of the scattering objects is seen, for example the nanofiller geometry, size and dispersion, while at high  $q$  the internal structure of the particles can be resolved and also the crystal structure of the polymer.

Scattering experiments are carried out in different angular regions. The sub-areas are identified by the typical distance  $R$  between the sample and the detector. The wavelength selected for the example is close to the wavelength of an X-ray tube equipped with a copper anode (CuK $\alpha$  radiation with  $\lambda = 0.154$  nm). Classical X-ray diffraction and scattering is carried out in the sub-area of wide-angle X-ray scattering (WAXS). The corresponding scattering patterns yield information on the arrangement of polymer-chain segments (e.g. orientation of the amorphous phase, crystalline structure, size of crystals, crystal distortions, WAXS crystallinity). The sub-area of middle-angle X-ray scattering (MAXS) covers the characteristic scattering of liquid-crystalline structure and rigid-rod polymers.

In the small-angle X-ray scattering (SAXS) regime the typical nanostructures, for e.g. in case of polymer nanocomposites, the size, shape and dispersion of the nanofillers are observed.

### 2.5.1 Spatial correlation function

Elastic and inelastic scattering techniques are based on the measurement of the spatial and temporal correlations in the scattering medium.

The scattering function (also called static structure factor) establishes the relationship between a sample and its scattering behavior. The derivation of the static correlation function can be based on the so-called pair correlation function. This function describes the interaction between particles and takes the form:

$K(\mathbf{r}_{12}) = \frac{H(\mathbf{r}_1/\mathbf{r}_2)}{H(\mathbf{r}_1)H(\mathbf{r}_2)}$	<b>(34)</b>
--	-------------

$H(\mathbf{r})$  is the probability to find a particle at a certain position  $\mathbf{r}$ , and  $H(\mathbf{r}_1/\mathbf{r}_2)$  is the probability of finding a particle 1 at position  $\mathbf{r}_1$  and particle 2 at position  $\mathbf{r}_2$ .<sup>96</sup> From the Fourier transform of the pair correlation function, the scattering function  $S(q)$  can be found. The easiest

example is to consider the case of a monoatomic liquid, in which case the scattering function takes the form:

$S(q) = 1 + \rho_d \int_0^{\infty} dr \left[ 4\pi^2 K(r) \frac{\sin qr}{qr} \right]$	<b>(35)</b>
--	-------------

$\rho_d$  is the density number of atoms.<sup>97</sup>

The major difference between a monoatomic liquid and e.g. a polymer chain in the melt or in solution is that the total structure factor consists of two parts. The first is the inter-particle structure factor, and the second the intraparticle structure factor. In the literature they are usually called structure factor  $S(q)$  and particle form factor  $P(q)$ , respectively.

A first, straightforward analysis, which already reveals some information on the shape of the investigated particles, is the calculation of the scattering exponent in the low  $q$ -regions of the experimental data ( $q^a \leq 1$ ) by fit to expressions of the type:

$I(q) = \frac{1}{q^a}$	<b>(36)</b>
------------------------	-------------

$a = 0$  for spherical aggregates and  $a = 1$  for cylindrical aggregates. In case of SAXS of polymer based nanocomposites, the particle size and shape can be determined. In case of lamellar structure, Gaussian functions are fitted to the low  $q$ -value peaks, and the peak position ( $q_{\text{peak}}$ ) and peak widths ( $w$ ) are estimated. By using Braggs law, then the distance between the two layers ( $d$ ) and the stack size ( $l_c$ ) are calculated by

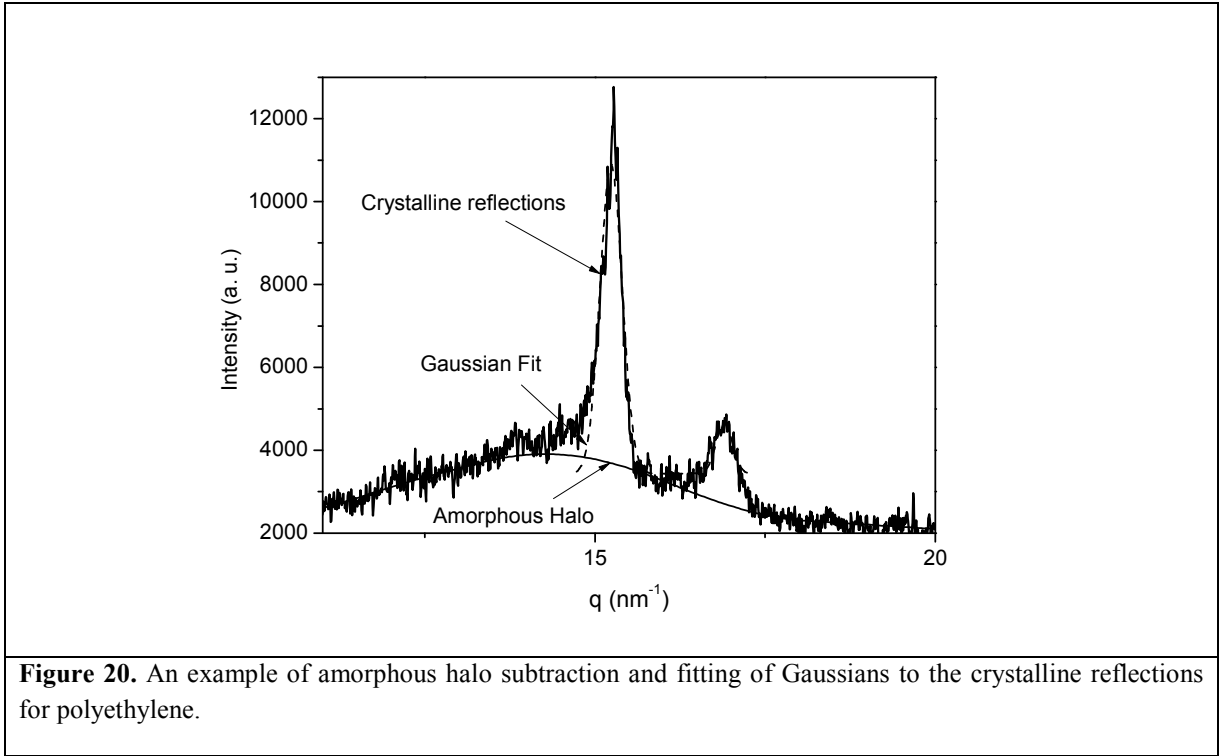
$d = 2\pi/q_{\text{peak}}$  and  $l = 2\pi/w$ . The slope at very low  $q$ -values is then fitted using power law dependence given in Eq. 36.

In case of LDH based nanocomposites, a rough estimate about the morphology (intercalated or exfoliated) can be determined by plotting  $q^2 I(q)$  vs.  $q$ . This is called Kratky plot and is used to determine qualitatively the conformations of the polymer chain or molecular shape.<sup>95</sup>

### 2.5.2 Amorphous halo subtraction in WAXS

The use of WAXS for crystallinity estimation involves analysis of crystalline reflections superposed on a broad amorphous halo. The peaks for crystallinity are then obtained by subtracting this amorphous halo from the diffractogram. In general, there are two methods to do this:

- 1) If completely non-crystalline material is available, then a diffractogram pattern is obtained in the same angular range. This halo is then properly scaled and subtracted from the crystalline diffractogram.
- 2) In case a non-crystalline or completely amorphous material is not available, then the subtraction is achieved either by peak fitting or by estimating the shape from the corresponding molten material.



By fitting Gaussians to both determined amorphous halo and subtracted crystalline patterns, the areas below the peaks are calculated (Figure 20),

$\chi = \frac{I_{\text{crystalline}}}{I_{\text{crystalline}} + I_{\text{amorphous}}} \times 100\%$	<b>(37)</b>
--	-------------

By using Eq. 37, the degree of crystallinity (mass %) can be determined, where,  $I_{\text{crystallinity}}$  is the area below crystalline reflections and  $I_{\text{amorphous}}$  area below the halo.

### 2.5.3 Berlin Electron Storage Ring Society for Synchrotron Radiation (BESSY)

When electromagnetic radiation is emitted by radially accelerating charged particles, it is termed as ‘Synchrotron radiation’. It is produced in synchrotrons using bending magnets, undulators and/or wigglers. Synchrotron radiation is generated by the acceleration of charged

particles through magnetic fields. The radiation produced in this way has a characteristic polarization, and the frequencies generated can range over the entire electromagnetic spectrum.

The BESSY II synchrotron source (Figure 21) located in Adlershof, Berlin, has a circumference of 240 m, providing 46 beam lines, and offers a multi-faceted mixture of experimental opportunities (undulator, wiggler and dipole sources) with excellent energy resolution. The combination of brightness and time resolution enables both femtosecond time and picometer spatial resolutions.

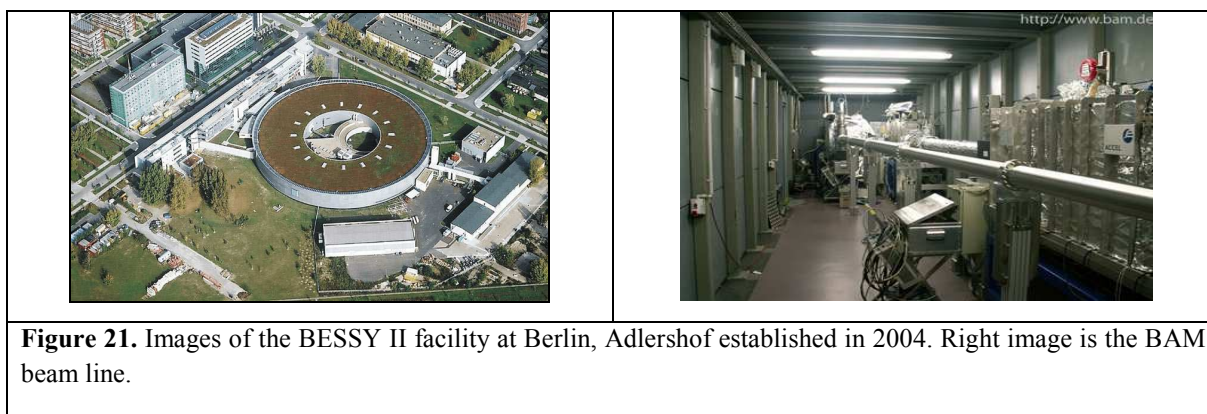


**Figure 21.** Images of the BESSY II facility at Berlin, Adlershof established in 2004. Right image is the BAM beam line.

## 2.6 Differential Scanning Calorimetry (DSC)

The possible glass and phase transitions in polymers can be observed experimentally by measuring the thermodynamic properties as a function of temperature. DSC yields quantitative information relating to the enthalpic changes in the polymer which is subjected to a temperature program. The DSC instrument consists of two pans of same material; one is called reference and the other sample pan. The reference pan is kept empty and sample pan contains the material. However, in some cases the reference pan contains a standard material such as constantan (Cu-Ni alloy). Both the pans are heated at a constant rate in the temperature range of interest. Due to the difference in the heat capacity of both the pans, there exists a temperature difference. Heat energy is supplied in order to keep both the pans at equal temperature. This difference in energy is observed either as a kink or peak corresponding to glass or phase transition respectively.

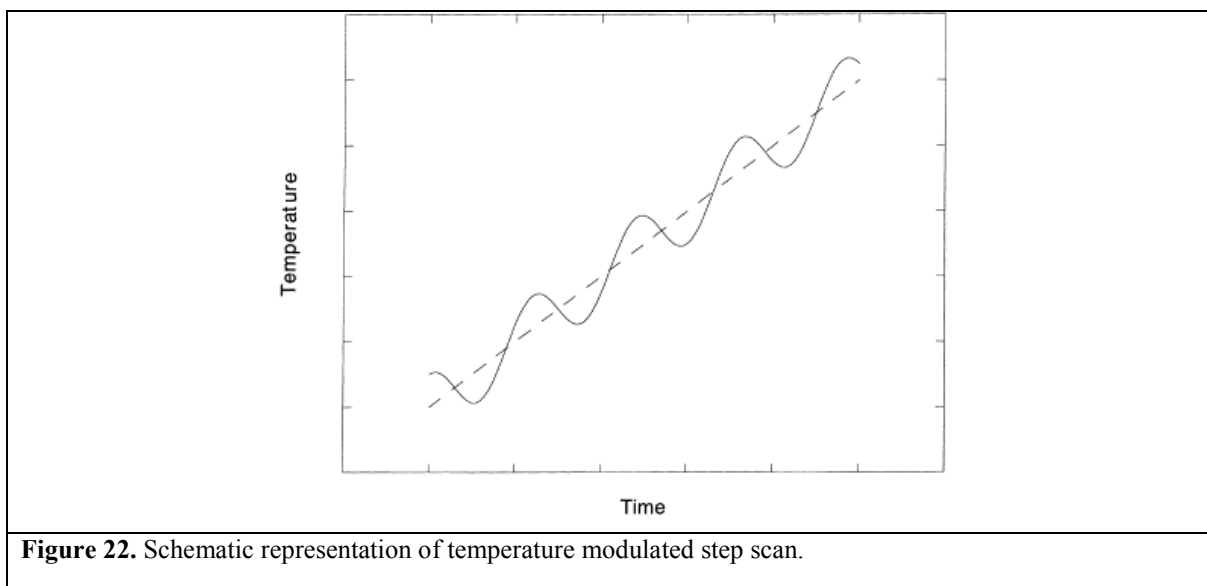
**Temperature Modulated DSC (TMDSC):** TMDSC is an extension of the conventional DSC technique introduced by Reading et al. in 1995.<sup>98</sup> As the name indicates, a periodic temperature modulation is superimposed on the linear heating or cooling rate of a conventional DSC measurement. It allows modulation with either simple waveforms such as steps or saw teeth, or with sinusoidal waveforms characterized by temperature amplitude  $A_T$

and an angular frequency  $\omega$ , defined as  $2\pi/h$ , where  $h$  denotes the period of the sine wave. In this latter case, the general temperature program,  $T(t)$ , is given by,

$$T(t) = T_a + \beta_0 t + A_T \sin(\omega t) \quad (38)$$

where,  $T_a$  denotes the initial temperature,  $t$  the time and  $\beta_0$  the underlying (average) heating rate.

The measured heat flow in response to the temperature program is also periodic. Certain effects such as changes in the specific heat capacity due to a glass transition can follow the applied heating rate (“reversing” phenomena), whereas other effects such as crystallization cannot (“nonreversing” phenomena). The periodic heat flow signal is therefore the superposition of an in-phase heat flow component and a component that is out of phase with the heating rate.



The usually linear temperature program is modulated by a small perturbation, in this case a sine wave, and a mathematical treatment is applied to the resultant data to deconvolute the sample response to the perturbation from its response to the underlying heating program. In this way the reversible (within the time scale of the perturbation) and irreversible nature of a thermal event can be probed. The advantages include disentangling overlapping phenomena. Improving resolution and enhancing sensitivity. A further benefit is that meta-stable melting can be detected in cases where it is not normally observed.

This chapter deals with a brief introduction of the equipments and instruments used for characterization and analysis of the polymer based nanocomposites.

### 3.1 Broadband Dielectric Relaxation Spectroscopy (BDS)

#### 3.1.1 Dielectric measurement techniques<sup>140</sup>

The complex dielectric function  $\varepsilon^*(\omega)$  can be determined using dielectric spectroscopy within a range from  $\mu\text{Hz}$  to  $\text{THz}$ . For a capacitor  $C^*$  filled with a material under study, the complex dielectric function is given by:

$$\varepsilon^*(\omega) = \frac{C^*(\omega)}{C_0} \quad (39)$$

Here,  $C_0$  is the vacuum capacitance of the capacitor. Applying a sinusoidal electric field  $\mathbf{E}^* = \mathbf{E}_0 \exp(i\omega t)$ , the complex dielectric function can be deduced by measuring the complex dielectric impedance  $Z^*(\omega)$ .

$$\varepsilon^*(\omega) = \frac{1}{i\omega Z^*(\omega)C_0} \quad (40)$$

In order to determine the complex impedance of the sample, several methods such as Fourier correlation analysis ( $10^{-6} - 10^7 \text{ Hz}$ ),<sup>99</sup> impedance analysis ( $10^1 - 10^7 \text{ Hz}$ ),<sup>100</sup> coaxial line reflectrometry ( $10^6 - 10^9 \text{ Hz}$ )<sup>66</sup> and network analysis ( $10^7 - 10^{11} \text{ Hz}$ )<sup>101</sup> have been utilized.

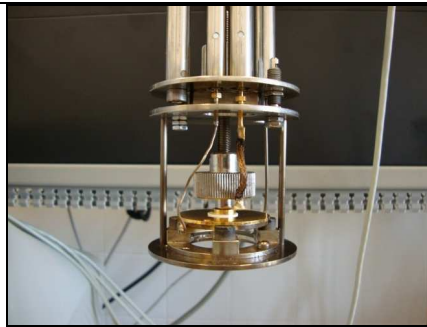


**Figure 23.** Measurement cell for BDS, frequency range from  $10^{-1}$  to  $10^6 \text{ Hz}$ .



Dielectric relaxation spectroscopy (BDS) was used to investigate the molecular mobility in the nanocomposites. A high-resolution ALPHA analyzer (Novocontrol, Hundsagen, Germany) is used, to measure the complex dielectric function  $\varepsilon^*(f) = \varepsilon'(f) - i\varepsilon''(f)$  ( $\varepsilon'$ -real part,  $\varepsilon''$ -loss part and  $i = \sqrt{-1}$ ) as a function of frequency  $f$  ( $10^{-1}$  Hz to  $10^6$  Hz). The samples were mounted between two gold-plated electrodes (20 mm) of the sample holder. All the measurements were done isothermally where the temperature is controlled by a Quatro Novocontrol cryo-system with a temperature stability of 0.1 K. This procedure leads to an effective heating rate of 0.13 K/min. For more details see Ref 140. The experimental data were collected and monitored online by the program WINDETA<sup>®</sup>.

### 3.1.2 Fitting HN Function to Experimental Results

The analysis of dielectric function is accomplished by fitting model functions to the experimental data in the isothermal scale. Despite the conductive contribution, the HN function describes the dielectric data in the best way in the frequency domain.

Each parameter of the HN function can be determined by:

$\sum_i w_i [\varepsilon_i^* - \varepsilon_{HN}^*(\omega_i)]^2 \rightarrow \min$	<b>(41)</b>
--	-------------

where,  $i$  counts the number of experimental points.  $w_i$  is the weighing factor and it characterizes the accuracy of data measured by different equipments. In principle, the dielectric loss or the permittivity can be used for analysis. Both quantities provide the same information about the relaxation process. In our discussion we have used the dielectric loss peak for analysis.

The dielectric spectrum consists of superposition of several relaxation processes, due to fluctuation of dipolar groups or polarization of moving charge carriers. Assuming the actual relaxation spectrum is a combination of  $k$  different processes and the whole spectrum consists of  $i$  different measurement points, the complex dielectric function can be separated by the HN function:

$\sum_i w_i [\varepsilon_i^* - \sum_k \varepsilon_{HN,k}^*(\omega_i)]^2 \rightarrow \min$	<b>(42)</b>
---	-------------

### 3.2 X-ray Scattering (SAXS and WAXS)

The synchrotron micro focus beamline  $\mu$ Spot (BESSY II of the Helmholtz Centre Berlin for Materials and Energy) was employed for the SAXS experiments of the nanocomposites. Providing a divergence of less than 1 mrad (horizontally and vertically), the focusing scheme of the beamline is designed to provide a beam diameter of 100  $\mu$ m at a photon flux of  $1 \times 10^9 \text{ s}^{-1}$  at a ring current of 100 mA. The experiments were carried out employing a wavelength of 1.03358 Å using a double crystal monochromator (Si 111). Scattered intensities were collected 820 mm behind the sample position with a two-dimensional X-ray detector (MarMosaic, CCD  $3072 \times 3072$  pixel with a point spread function width of about 100  $\mu$ m). A more detailed description of the beamline can be found in reference.<sup>102</sup>

The obtained scattering images were processed and converted into diagrams of scattered intensities versus scattering vector  $q$  ( $q$  is defined in terms of the scattering angle  $\theta$  and the wavelength  $\lambda$  of the radiation, thus  $q = 4\pi/\lambda \sin\theta$ ) employing an algorithm of the computer program FIT2D.<sup>103</sup>

SAXS data were also collected in house on a SAXSess (Anton Paar) instrument using  $\text{CuK}\alpha$  radiation ( $\lambda = 1.54 \text{ Å}$ ) and an image plate detector. Two dimensional data collected from the image plate were integrated to one dimension and reduced to  $I(q)$  versus  $q$  using the SAXSquant software package provided by the vendor.

WAXS were carried out using  $\text{Cu-K}\alpha$  radiation with a curved position sensitive detector (INEL CPS120).

For the characterization of unmodified LDH, X-ray scattering was performed using a 2-circle diffractometer XRD 3003  $\theta/\theta$  (GE Inspection Technologies/Seifert-FPM, Freiberg) with a  $\text{Cu-K}\alpha$  radiation ( $\lambda = 1.54 \text{ Å}$ ) generated at 30 mA and 40 kV.

### 3.3 Differential Scanning Calorimetry (DSC)

A Seiko instruments Differential scanning calorimeter (DSC 220C) was employed for the thermal analysis of the nanocomposites. The samples (10 mg) were measured with a heating and cooling rate of 10 K/min. Nitrogen was used as protection gas. The thermograms are taken from the second run. The enthalpy changes related to melting and crystallization were calculated.

Also, the thermograms generated were used to determine the  $T_g$  of the sample which is taken at the inflection point of temperature due to  $C_p$  changes. Temperature-modulated DSC

(TMDSC) measurements were also carried out using a PerkinElmer PYRIS Diamond DSC at the Physics Department of University of Rostock. Initially samples were cooled to 223 K. Precise heat capacity at  $T_g$  was determined from the following StepScan differential scanning calorimetry (SSDSC) run, a special variant of temperature modulated DSC. Measurements were performed using samples of about 20 mg, 2 K steps at heating rate 6 K/min and isotherms of about 1.5 min.<sup>104,105</sup> The instrument was calibrated as recommended by GEFTA<sup>106</sup> by indium and zinc at zero heating rates for temperature and by sapphire for heat capacity.

### **3.4 Transmission Electron Microscope (TEM)**

Some morphological analysis was carried out at IPF Dresden by Dr. D. Y. Wang using transmission electron microscopy (TEM) with microscope LEO 912. The conditions used during analysis were room temperature, 120 kV acceleration voltage and bright field illumination. The ultra-thin sections of the samples were prepared by ultramicrotomy at -120°C with a thickness of 80 nm.

The different nanocomposites were prepared by melt blending. This chapter provides information about the matrix polymers and the nanofillers in terms of their characteristics determined by BDS & DSC and SAXS respectively. Moreover, the synthesis of LDH, preparation of the nanocomposites and the sample information is also given in this section. It should be noted that the synthesis of LDH and the preparation of the nanocomposites was exclusively done by Dr. De-Yi Wang at Leibniz Institute for Polymers Research (IPF), Dresden, Germany.

## 4.1 Nanofillers

### 4.1.1 Layered Double Hydroxide (LDH)

The introduction and concept of LDH was described earlier in Chapter 2. For the present case the LDH material is fully synthetic where the metal cations are  $\text{Zn}^{2+}$  and  $\text{Al}^{3+}$ . The employed inter gallery anion of LDH is sodium dodecylbenzene sulfonate (SDBS) which was incorporated into the layered structure directly during the synthesis.<sup>20</sup> SDBS increases the spacing between the LDH sheets, which makes it possible for the polymer chains to intercalate. This is called as organic modification of LDH indicated as O-LDH hereafter.

#### 4.1.1.1 Zinc-Aluminium LDH (ZnAl-LDH)

In general, LDHs are commercially available, but in present case the LDH were completely lab synthesized in a one-step process.<sup>107</sup>

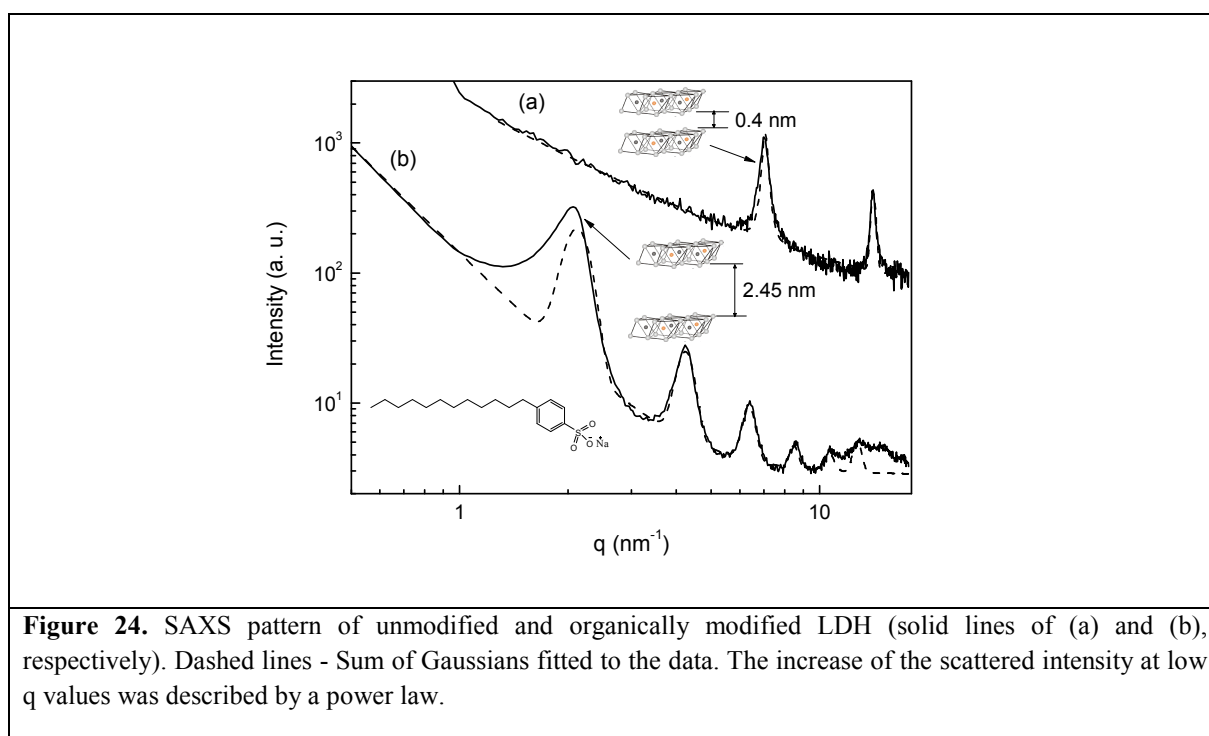
##### *Synthesis of ZnAl-LDH*

The metal nitrate salts ( $\text{Zn}(\text{NO}_3)_2 \cdot 6\text{H}_2\text{O}$  and  $\text{Al}(\text{NO}_3)_3 \cdot 9\text{H}_2\text{O}$ ), sodium dodecylbenzene sulfonate (SDBS) for the synthesis of organic ZnAl-LDH were obtained from Aldrich and used without further purification. Deionized water was required to dilute the solutions and wash the filtered precipitates. The synthesis of organo-modified ZnAl-LDH was carried out via a one step method.<sup>107</sup> The typical procedure is the slow addition of a mixed metal (divalent  $\text{Zn}^{2+}$  and trivalent  $\text{Al}^{3+}$ ) salt solution (with  $\text{Zn}^{2+}:\text{Al}^{3+}$  equal to 2:1) (with  $\text{MZn}^{2+} = 0.025$  mol,  $\text{MAl}^{3+} = 0.0125$  mol in 200 ml solution) to a SDBS solution (0.015 mol SDBS in 100 ml solution) under continuous stirring and maintaining the reaction temperature at 323 K. During the synthesis, the pH value was maintained at  $9 \pm 0.1$  by adding suitable amount of 1 M NaOH solution. The resulting slurry was continuously stirred at the same temperature

for 30 minutes and was allowed to age in a heater at 333 K for 18 h. The final products were filtered and washed several times with distilled water to remove non-reacted surfactant molecules until the pH of the supernatant solution was about 7. The material was then dried in an oven at 343 K until a constant weight was achieved. The product is called organo-modified ZnAl-LDH (O-LDH) where for comparison, the unmodified ZnAl-LDH (U-LDH) was also synthesized. The empirical formulae both of U-LDH and the O-LDH have been investigated by ICP and elemental analysis. For U-LDH it is  $\text{Zn}_{0.67} \text{Al}_{0.33} (\text{OH})_2 (\text{NO}_3)_{0.33} 0.4\text{H}_2\text{O}$  where as for O-LDH  $\text{Zn}_{0.67} \text{Al}_{0.33} (\text{OH})_2 (\text{SDBS})_{0.28} (\text{NO}_3)_{0.05} 0.4\text{H}_2\text{O}$  is found. This means SDBS is the only balancing anion. The water content was additionally calculated from TGA measurements to be around 4 wt-% which matches well with the empirical formula.

### **Characterization of ZnAl-LDH by SAXS**

The organic modification of U-LDH to O-LDH was characterized employing WAXS at IPF Dresden.



The SAXS diagram for unmodified LDH shows two equidistant reflections at  $7.05 \text{ nm}^{-1}$  and  $14.10 \text{ nm}^{-1}$  which is characteristic for a layered compound corresponding to a lamellar repeat distance of  $d = 0.89 \text{ nm}$  (Figure 24). Here, the thickness of the hydrotalcite brucite-like LDH sheet is  $0.49 \text{ nm}$ .<sup>108</sup> Subtracting this value gives the effective interlayer distance to be  $0.40$

nm. Traditionally, indexing LDH powder patterns is based on the hexagonal unit cells although the structures described are mostly rhombohedra, i.e. the peaks were accordingly assigned to the first (003) and second basal reflection (006). We determined peak widths of  $w = 0.31 \text{ nm}^{-1}$  from fitting Gaussian profiles to the measured data (Figure 24). The correlation lengths in direction perpendicular to the lamella normal is therefore  $l_c = 2\pi/w = 20.3 \text{ nm}$ . Assuming that lattice distortions could be neglected to a first approximation, this value represents the crystallite thickness in the normal direction of the (00l) plane. Then the average number of layers in a stack in the unmodified LDH is 23.

The modification of the LDH with SDBS to the O-LDH results in a shift of the lamellar reflections towards lower  $q$ -values, as expected. Six equidistant reflections are visible with the (003) reflection located at  $2.14 \text{ nm}^{-1}$  corresponding to  $d = 2.94 \text{ nm}$  (Figure 24). This value is in agreement with the value reported recently by Wang et. al. (2.98 nm).<sup>107</sup>

Subtraction of the thickness of the brucite-like LDH sheet results in an effective interlayer distance of 2.45 nm for O-LDH. This proves that SDBS is intercalated in the interlayer gallery thus modifying the LDH. A more detailed discussion of similar systems can be found elsewhere.<sup>107</sup> A peak width of  $0.40 \text{ nm}^{-1}$  to  $0.50 \text{ nm}^{-1}$  is determined from fitting six equidistant Gaussians to the experimental curve. Therefore  $l_c$  is in the range of 12.6 nm to 15.7 nm, which is equivalent to 4.3 to 5.3 layers. The number of layers is drastically reduced in O-LDH as compared to U-LDH. This reduction in the number of layers in case of O-LDH can be argued as follows: The SDBS molecules used for the modification increases the  $d$ -spacing between the layers, which in turn sterically hinders large size stack formation. Moreover, the lack of reflections at  $7.05 \text{ nm}^{-1}$  and  $14.10 \text{ nm}^{-1}$  in the diagram of O-LDH proves the absence of significant amounts of U-LDH. One has to conclude here that already small stacks of O-LDH with only few layers are used to prepare nanocomposites.

#### **4.1.1.2 Magnesium-Aluminium LDH (MgAl-LDH)**

##### ***Synthesis of MgAl-LDH***

In case of MgAl-LDH, a two step process was employed for synthesizing, in which first the LDH was synthesized and then it was treated with anionic surfactant SDBS. The procedure of synthesis was as follows:

Mg–Al LDH was synthesized by urea hydrolysis method described by Costantino et al.<sup>109</sup> An aqueous solution containing  $\text{Al}^{+3}$  and  $\text{Mg}^{+2}$  with the molar fraction  $\text{Al}^{+3}/(\text{Al}^{+3} + \text{Mg}^{+2})$  equal to 0.33 was prepared by dissolving  $\text{AlCl}_3$  and  $\text{MgCl}_2$  in distilled water. To this solution

solid urea was added until the molar fraction  $\text{urea}/(\text{Mg}^{+2} + \text{Al}^{+3})$  reached 3.3. The clear solution was refluxed for 36 h. The white precipitate was then filtered, washed until chloride free and dried in vacuum at 333 K till constant weight.

LDH was then calcined in a muffle furnace at 723 K for about 3 h to convert it into metal oxide (CLDH). The calcined product was dispersed in 0.1 M aqueous solution of SDBS with solid/solution ratio 1 g/50 cm<sup>3</sup> and the dispersion was stirred by magnetic stirrer for 24 h at room temperature. The regenerated SDBS intercalated LDH (SDBS-LDH) was then filtered out followed by drying in vacuum at 333 K.

### ***Characterization of MgAl-LDH by SAXS***

Similar to ZnAl-LDH, MgAl-LDH was also characterized by SAXS to determine the successful organic modification.

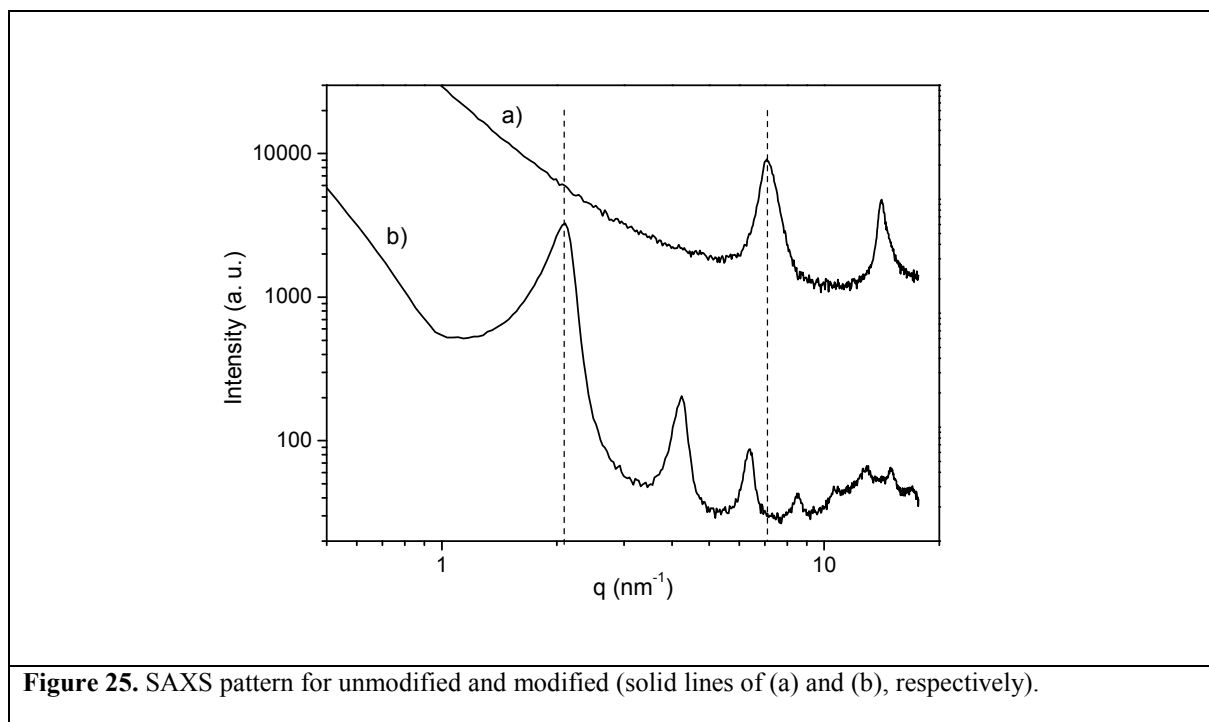


**Figure 25.** SAXS pattern for unmodified and modified (solid lines of (a) and (b), respectively).

Similar analysis was performed as for MgAl-LDH and the following calculations were done. For unmodified LDH (U-MgAl-LDH),  $d = 0.39 \text{ nm}$  ( $q_{\text{peak}} = 7.13 \text{ nm}^{-1}$ , after brucite sheet thickness subtraction) and stack size,  $l_c = 9.23 \text{ nm}$  ( $w = 0.69 \text{ nm}^{-1}$ ). As it can be seen, that the (003) reflection for U-LDH is quite broad as compared to U-ZnAl-LDH, in other words, the stack size is smaller ( $l_c = 2\pi/w$ ). So, the no. of layers present in U-LDH is around 10. This is smaller than the no. of layers present in unmodified ZnAl-LDH. Similarly, for O-MgAl-LDH,  $d = 2.54 \text{ nm}$  ( $q_{\text{peak}} = 2.07 \text{ nm}^{-1}$ , after brucite sheet thickness subtraction); this proves the modification of the U-MgAl-LDH, and stack size,  $l_c = 17.44 \text{ nm}$  ( $w = 0.36 \text{ nm}^{-1}$ ). This

results in around 6 layers on an average per stack. Even in this case, SDBS sterically hinders the large stack formation and reduces the no. of layers in O-MgAl-LDH. Table 1 gives an outline about the stack size, d-spacing (after brucite thickness subtraction) and no. of layers for the nanofillers.

**Table 1.** Compilation of information about d-spacing, stack size and no. of layers for ZnAl-LDH and MgAl-LDH.

Filler	Unmodified			Organically Modified		
	$d$ (nm)	Stack size ( $l_c$ ) (nm)	No.of layers	$d$ (nm)	Stack size ( $l_c$ ) (nm)	No.of layers
<b>ZnAl-LDH</b>	0.4	20.3	23	2.45	13.5	5
<b>MgAl-LDH</b>	0.39	9.2	10	2.54	17.4	6

#### 4.1.2 Carbon Nanotubes (CNT)

The CNT used for this present work is NANOCYL<sup>TM</sup> NC7000 series (commercially available), thin multi-wall carbon nanotubes, produced via the catalytic carbon vapor deposition (CCVD) process.

A primary interest is in applications requiring low electrical percolation threshold such as high performance electrostatic dissipative plastics or coatings. The average diameter is around 9.5 nm and average length 1.5 microns as determined by the TEM. The purity of carbon is around 90% and surface area determined by BET is 250 – 300 m<sup>2</sup>/g.

## 4.2 Matrix Polymers

Basically, nanocomposites based on LDH and CNT were investigated for three different polymers, Polyethylene (PE), Polypropylene (PP), and Polylactide (PLA). A brief introduction by highlighting the DSC and BDS results for each polymer will be described.

#### 4.2.1 Polyethylene (PE)

The repeating unit of polyethylene (PE) is shown in Figure 26. Depending on the density of the polymer, it is classified as high or low density polyethylene. In this work, low density polyethylene (LDPE; density 0.925 g/cm<sup>3</sup>; melt flow index MFI 3.52 g/10 min) produced by Exxon Mobil was characterized. Maleic anhydride grafted polyethylene (MAH-g-PE) (density 0.926 g/cm<sup>3</sup>, MFI 32.0 g/10 min, maleic anhydride concentration 1.0 wt %) was used as a compatibilizer. It was obtained from Crompton, USA.



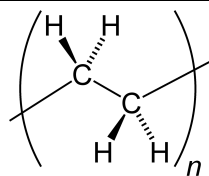


**Figure 26.** The repeat unit of Polyethylene (PE).

#### 4.2.1.1 DSC Measurement

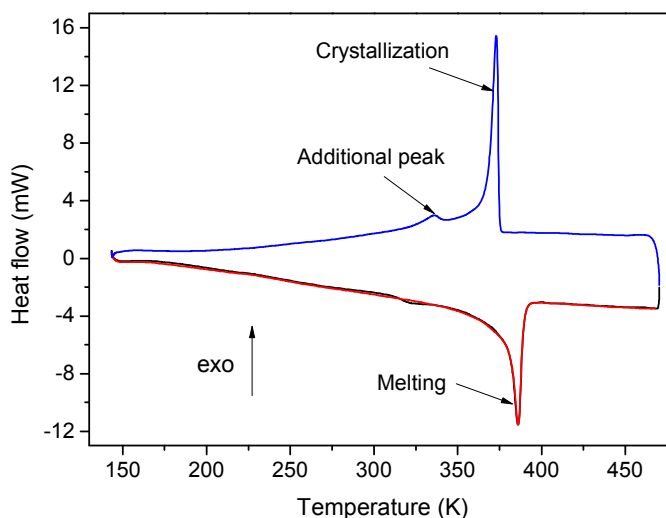


**Figure 27.** DSC thermogram for pure PE, the melting (red, 2<sup>nd</sup> heating scan, heating and cooling rate of 10 K/min) and crystallization (blue, cooling scan) peaks are presented too.

DSC measurements show a peak due to the melting process at 386 K, and another one for the crystallization at 373.1 K during cooling. Another peak around 335 K is observed in the cooling curve of the PE. Its origin might be related to rearrangements of the forming crystals. In the second heating this peak disappears (see Figure 27). The melting enthalpy  $\Delta H_{\text{melt}}$  is calculated to be 213 J/g.K and the crystallization enthalpy  $\Delta H_{\text{Crys}} = 190$  J/g.K. Various glass transition temperature values are reported in the literature which is mainly because of the characterization method used to determine it. However, a value of 148 K is reported by Ref 110.

#### 4.2.1.2 BDS Measurements

Polymers with a high degree of crystallinity like polypropylene, polyethylene in general follows a different nomenclature of relaxation processes as compared to amorphous

polymers.<sup>66</sup> For amorphous polymers with a low degree of crystallization glassy dynamics related to segmental mobility is referred to as  $\alpha$ -relaxation. For polymers with a high degree of crystallinity, glassy dynamics in the most of the publications, is called  $\beta$ -relaxation.<sup>22,128,133</sup> Sometimes this causes confusion but because of the fact that this nomenclature is well established, here dynamic glass transition will be termed as ' $\beta$ -relaxation'.

The polyethylene chains possess a very weak dipole moment; it is rather difficult to find a response of the dielectric function versus the temperature and frequency. This is because the dipole moments of the carbon – hydrogen bonds cancel each other along the chain. Nevertheless, besides other approaches the dielectric probe technique was used to study the molecular dynamics of polyethylene in detail<sup>121</sup> which is presented below.

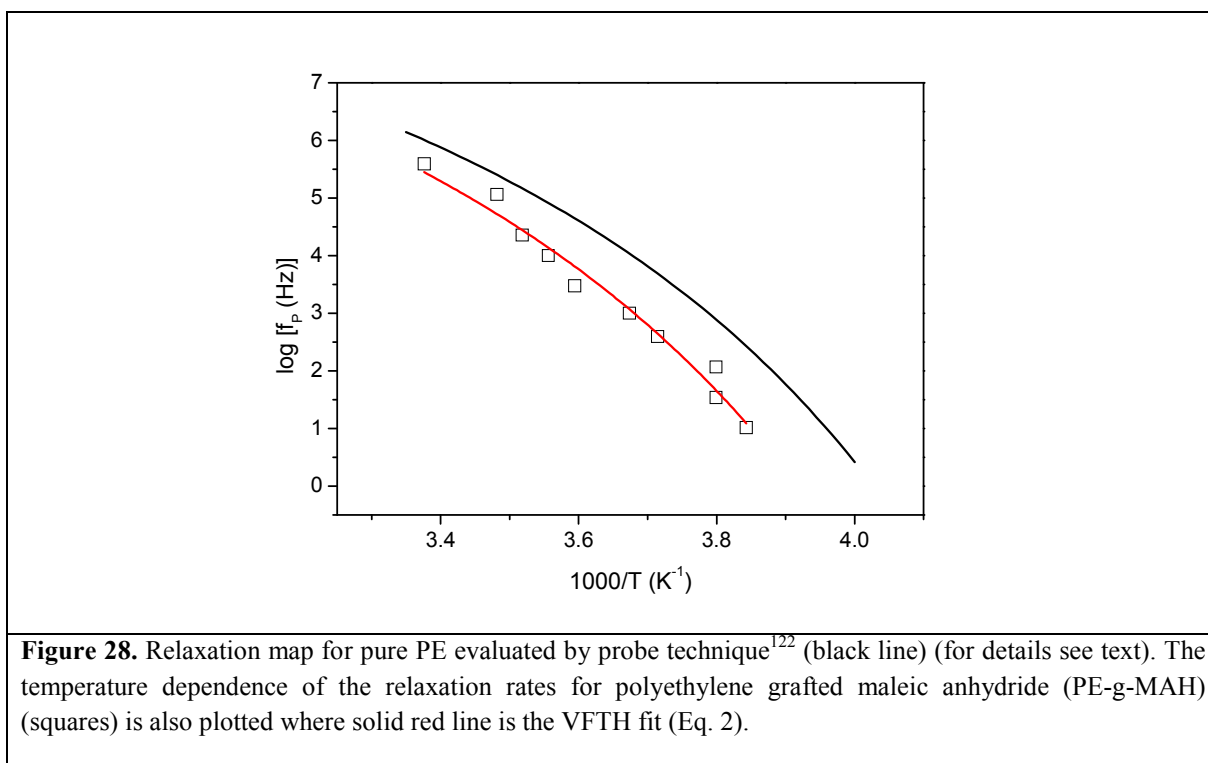
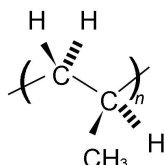


Figure 28 shows the relaxation map of pure PE and PE-g-MAH. The temperature dependence of the mean relaxation rates is curved and well described by VFTH function (Eq. 2). This indicates a glassy dynamics behavior of the only process observed originating from segmental fluctuations. The VFT fit parameters are given in Table 2.

#### 4.2.2 Polypropylene (PP)

Polypropylene (PP, homopolymer, HD 120 MO, density: 0.908 g/cm<sup>3</sup> and melt flow index of 8 g/10 min) was purchased from Borealis, Porvoo, Finland. Maleic anhydride grafted polypropylene (MAH-g-PP, Exxelor PO1020) as compatibilizer (density: 0.9 g/cm<sup>3</sup> and melt flow index of 125 g/10 min) was supplied by Exxon Mobil Chemical. The MAH graft level is in the range of 0.5 to 1.0 wt%.



**Figure 29.** The repeat unit of Polypropylene (PP)

##### 4.2.2.1 DSC Measurement

The DSC thermogram is plotted below showing the crystallization and melting transitions whereas the inset shows the glass transition.

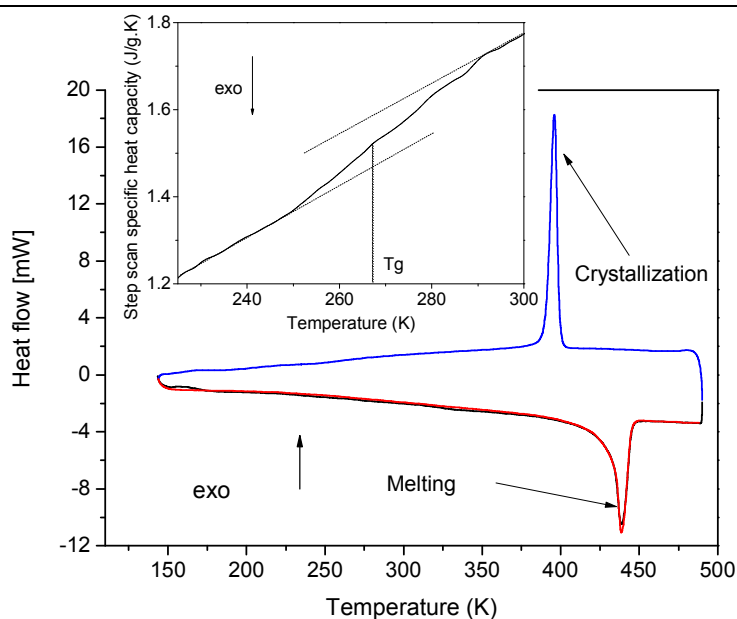


**Figure 30.** DSC thermogram for pure PP, the melting (red, 2<sup>nd</sup> heating scan, heating and cooling rate of 10 K/min) and crystallization (blue, cooling scan) peaks are presented too. Inset shows the thermogram measured by Stepscan TMDSC, glass transition temperature ( $T_g$ ) is determined from it.

The samples (10 mg) were measured from 173 K to 473 K with a heating and cooling rate of 10 K/min using nitrogen as protection gas. The enthalpy changes related to melting and crystallization were calculated from 343 K to 453 K and 363 K to 408 K respectively by estimating the areas below the corresponding peaks. The melting temperature ( $T_m$ ) was found to be 438.6 K and a melting enthalpy of  $\Delta H_{\text{melt}} = 117 \text{ J/g.K}$  whereas, the crystallization temperature ( $T_c$ ) is 395.9 K and the crystallization enthalpy of  $\Delta H_{\text{Crys}} = 111 \text{ J/g.K}$ . Standard methods for glass transition evaluation use tangents at the heat capacity curve above and below the glass transition region. The glass transition temperature  $T_g$  can be defined as the temperature at which the measured heat capacity curve equals the half distance between the tangents. Then, the thermal relaxation strength ( $\Delta C_p$ ) is defined as the difference between the tangents at  $T_g$ . (The term “thermal relaxation strength” is used for describing the height of the heat capacity step at glass transition).

The glass transition was found to be 264 K and  $\Delta C_p$  of 0.084 J/g.K as determined by Stepscan DSC performed at the Physics Department of University of Rostock.

#### 4.2.2.2 BDS Measurement

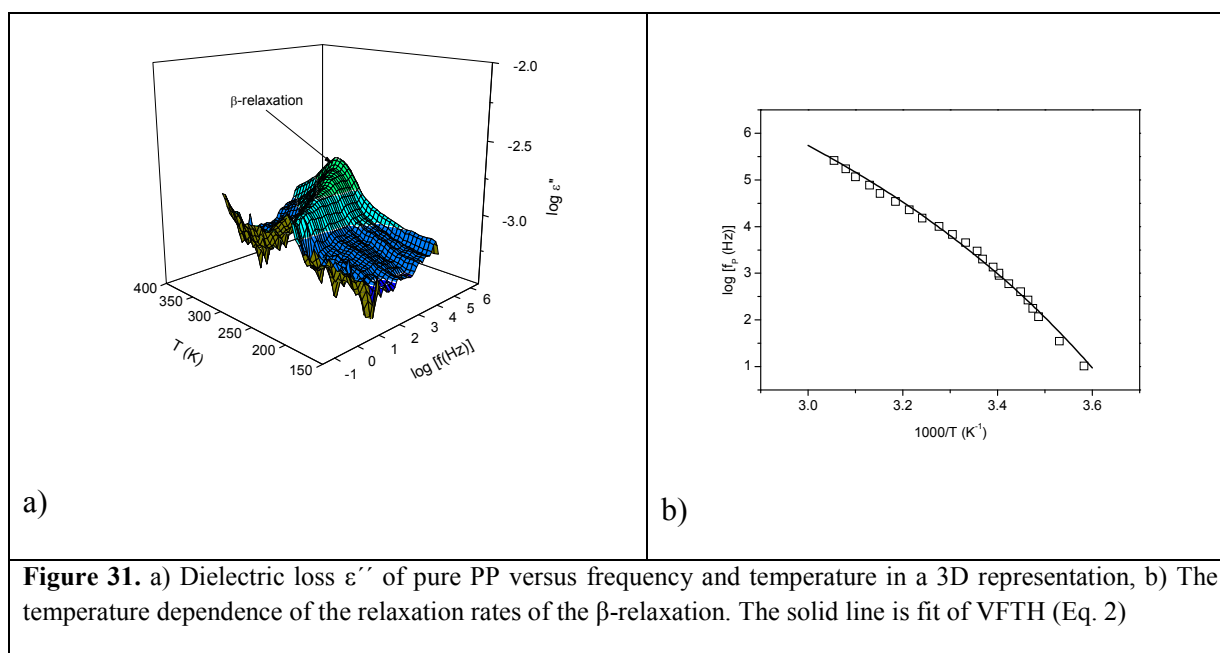


Figure 31 displays the dielectric behavior of pure polypropylene versus frequency and temperature in a 3D representation. The dielectric response of pure PP is weak, because the asymmetry in the repeating unit of polypropylene leads only to a low dipole moment. Moreover, by oxidation processes a small number of polar carbonyl groups can be formed. The dielectric spectra of pure polypropylene show one main relaxation process indicated by

a peak in the dielectric loss. With increasing temperature its shifts to higher frequencies as expected. This process is called  $\beta$ -relaxation and corresponds to the dynamic glass transition related to segmental fluctuations. The temperature dependence of the relaxation rate of the  $\beta$ -relaxation is plotted in Figure 31b. The VFT parameters are given in Table 2. At lower temperatures (higher frequencies) than the  $\beta$ -relaxation, a  $\gamma$ -relaxation is observed which corresponds to localized fluctuations as discussed in more detail later.

**Table 2.** VFT parameters for pure PE, PE-g-MAH, and PP.

Sample name	$\beta$ -relaxation (dynamic glass transition)		
	$\log [f_{\infty} \text{ (kHz)}]$	$A_0 \text{ (K)}$	$T_0 \text{ (K)}$
Pure PE	12	803	205
PE-g-MAH	12	590	206
Pure PP	12	914	182

### 4.2.3 Polylactide (PLA)

Poly(lactic acid) or Polylactide (PLA) is one of the most promising candidates in environmental friendly polymers because it is biodegradable and can be produced from renewable resources (sugar beets, corn starch, etc.). Further, PLA is promising in replacing some petrochemical polymers due to its excellent mechanical properties, high degree of transparency, and the ease of fabrication.

For the present research Biomer<sup>®</sup> L9000 was purchased from Biomer, Krailling, Germany.

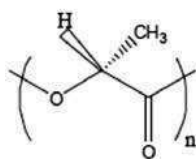


**Figure 32.** The repeat unit of Polylactide (PLA).

#### 4.2.3.1 DSC Measurement

In case of PLA, a glass transition, melting and crystallization phenomenon were observed in the DSC thermogram (see Figure 33). The DSC was measured from 248 K to 523 K at 10 K/min using nitrogen gas. The crystallization and melting temperatures are 403 K and 440

K, whereas the corresponding enthalpies are 6 J/g.K and 8 J/g.K respectively. A glass transition temperature of 333 K and  $\Delta C_p$  of 0.51 J/g.K was also calculated from the thermogram.

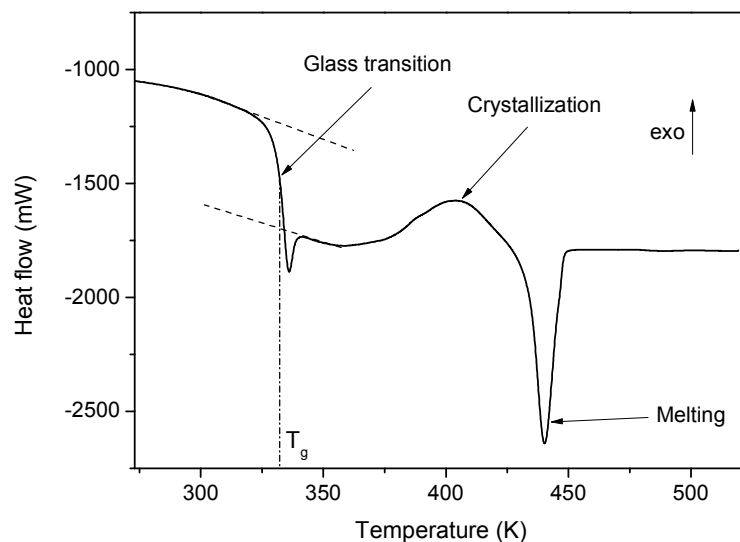


**Figure 33.** DSC thermogram for pure PLA showing glass transition, crystallization and melting, 2<sup>nd</sup> heating scan with a heating rate of 10 K/min.

#### 4.2.3.2 BDS Measurement

In case of PLA, the convention of amorphous polymers is followed, so  $\alpha$ -relaxation will be used for dynamic glass transition, whereas for localized fluctuations  $\beta$ -relaxation will be termed.

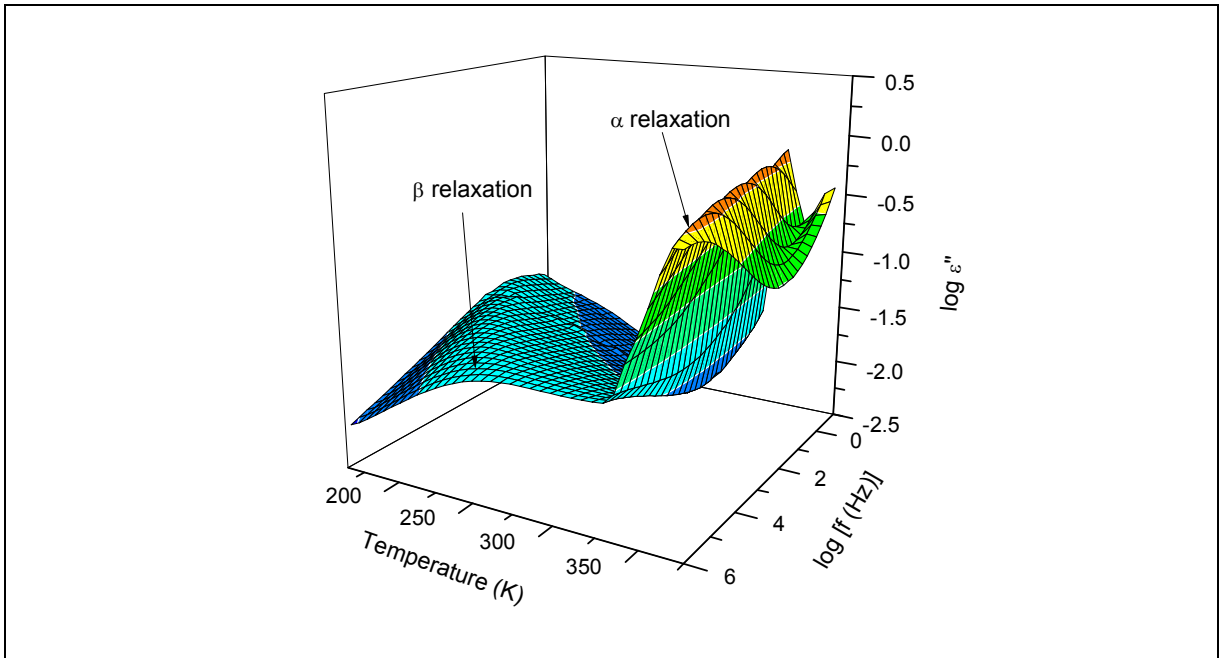
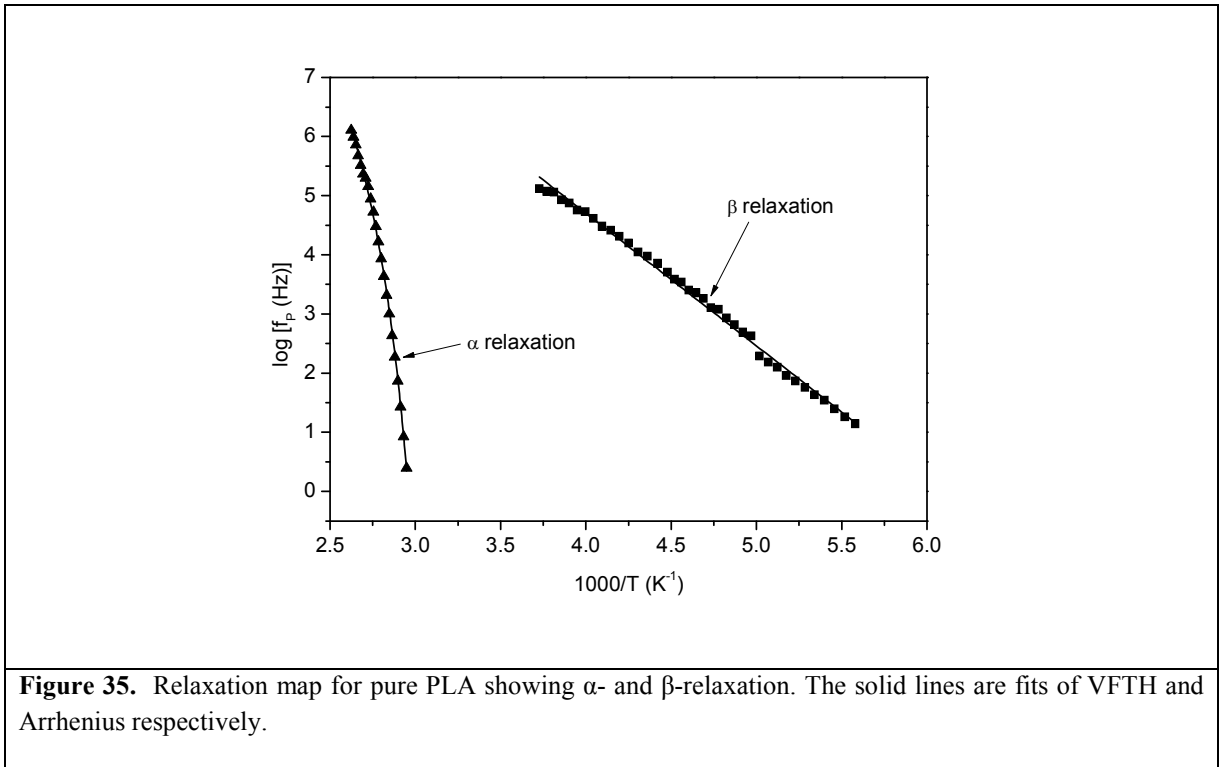


**Figure 34.** Dielectric loss vs. temperature and frequency for pure PLA in a 3D representation.

The dielectric spectra of pure polylactide show two main relaxation processes indicated by a peak in the dielectric loss (see Figure 34).<sup>111,112</sup> With increasing temperatures both the processes shift to higher frequencies as expected. The process observed at lower temperatures (higher frequencies) is called  $\beta$ -relaxation and corresponds to the localized fluctuations. As discussed before in Chapter 2, BDS is sensitive to dipoles, in this case the  $\beta$ -relaxation corresponds to fluctuations of the C=O bond. At higher temperatures (lower frequencies) than the  $\beta$ -relaxation,  $\alpha$ -relaxation is observed related to the dynamic glass transition corresponding to segmental fluctuations as discussed in more detail.

The HN function (section 2.4.3.2) is fitted to the different relaxation processes in the frequency domain. The mean relaxation rate as a function of inverse temperature is then plotted in Figure 35.



As described in Chapter 2, section 2.3.2, the dynamic glass transition ( $\alpha$ -relaxation) is well described by the VFTH function (Eq. 2) and the  $\beta$ -relaxation by Arrhenius (Eq. 1). The corresponding fit parameters are given in Table 3.

**Table 3.** VFT and Arrhenius parameters for pure PLA.

Sample name	$\alpha$ -relaxation			$\beta$ -relaxation	
	$\log [f_{\infty} \text{ (kHz)}]$	$A_0 \text{ (K)}$	$T_0 \text{ (K)}$	$\log [f_{\infty} \text{ (kHz)}]$	$E_A \text{ (kJ/mol)}$
Pure PLA	11.2	387.9	303.1	13.6	42.8

### 4.3 Sample Preparation

For the preparation of all the nanocomposites, melt blending technique was employed. The samples were provided by Dr. D. Y. Wang at Leibnitz Institute for Polymer Research, Dresden, Germany.

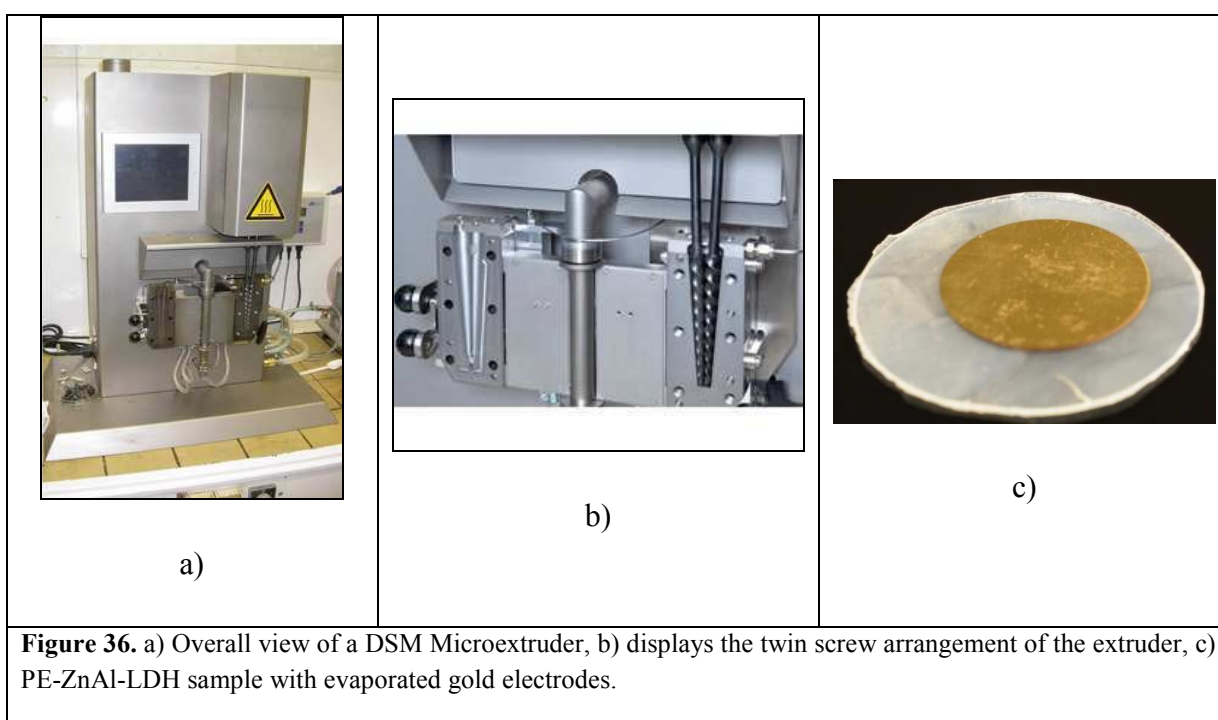
#### 4.3.1 LDH based Nanocomposites

The nanocomposites based on LDH were prepared by melt mixing. Before compounding, all the materials (polymers, LDH) were dried under vacuum at 323 K for 24 h. Two different approaches were used for the preparation of the nanocomposites viz. a two-step and one step approach. In case of two-step approach, nanocomposites based on PP and PE were prepared.



In the first step, the O-LDH was melt-compounded with maleic anhydride grafted polypropylene/polyethylene (MAH-g-PP)/(MAH-g-PE) in a weight ratio of 1:1 (based on the approximate metal hydroxide content of O-LDH) to prepare a masterbatch. In the second step, this masterbatch was added in different amounts to the PP/PE through melt compounding. Both steps were carried out in a co-rotating twin-screw microextruder (15-mL microcompounder, DSM Xplore, Geleen, The Netherlands). The conditions used for melt-compounding steps were 463 K with 200 rpm screw speed for 10 min. The concentrations of O-LDH in the nanocomposites were determined based on an approximate metal hydroxide content of the filler. The O-LDH prepared in the present study contains 50% of its weight as metal hydroxide. In case of PLA, a one step approach was employed as no MAH-grafted PLA was used. PLA contains a polar group in the main chain which can interact with the LDH for intercalation. So, MgAl-LDH was mixed in different concentrations with pure PLA to obtain various nanocomposites.

After melt compounding, the strands obtained were pressed into sheets using Vogt LaboPress 200T at 500 K, 10 bar, for 1 min (preheating of the material at 500 K for about 1 min). Following the above procedure, circular ( $D \sim 30$  mm) specimens of  $t \sim 0.5$  mm thickness were formed. Gold electrodes with a diameter of 20 mm were evaporated on both sides of the samples for BDS measurements, in order to have a good contact of the sample with the electrode plates. For the other characterization methods, the samples were used as it is. The various compositions prepared are given in section 4.4.



### 4.3.2 Nanocomposites based on PLA and CNT

The nanocomposites based on CNT were also prepared by melt blending. Prior to mixing the polymer was dried at around 323 K for 24 h and the MWCNT at 393 K for 2 h. The melt mixing was carried out at 473 K for 10 mins with a screw speed of 100 rpm. Similarly, the extruded strands were pressed into circular sheets of around 30 mm diameter and 0.5 mm thickness.

## 4.4 Sample Information

In terms of the physical properties, all the nanocomposites became more brittle with increasing concentration of the nanofillers (LDH and CNT). Considering the optical properties, the nanocomposites based on LDH and all the three polymers viz. PP, PE and PLA are ranging from translucent to opaque, whereas the CNT based PLA are completely black as expected. The following table gives the information about the different concentrations of the nano-fillers in the nanocomposites and their code names which will be used hereafter in the next chapters.

**Table 4.** Various compositions of the nanocomposites along with sample codes.

<b>Polypropylene + ZnAl-LDH</b>		<b>Polyethylene + ZnAl-LDH</b>		<b>Poly lactide + MgAl-LDH</b>		<b>Poly lactide + MWCNT</b>	
<b>Sample code</b>	<b>Amount of LDH (wt%)</b>	<b>Sample code</b>	<b>Amount of LDH (wt%)</b>	<b>Sample code</b>	<b>Amount of LDH (wt%)</b>	<b>Sample code</b>	<b>Amount of CNT (wt%)</b>
PP	0	PE	0	PLA	0	PLAC	0
PP2	2.43	PE2	2.43	PLA1	1	PLAC0.1	0.1
PP4	4.72	PE4	4.72	PLA3	3	PLAC0.5	0.5
PP6	6.89	PE6	6.89	PLA6	6	PLAC1	1
PP8	8.95	PE8	8.95	PLA9	9	PLAC2	2
PP12	12.75	PE12	12.75	PLA12	12	PLAC4	4
PP16	16.20	PE16	16.20	---	---	PLAC8	8

As discussed in Chapter 2, LDHs are good flame retardant materials. In application they are incorporated in the polymers to improve the thermal stability and also to make them flame retardant. Polypropylene is a commercial polymer which finds applications in day to day use such as automotive, household etc. Improving its flame retardancy by preparing nanocomposites based on LDH is obviously a motivation from a commercial point of view. However, it is not the flame retardant properties which will be discussed here, it can be found elsewhere,<sup>113</sup> but establishing the structure-properties relationships would definitely support scientifically the motivation mentioned above.

The synthesis of ZnAl-LDH and the preparation of the nanocomposites is given in Chapter 4. However, here the structure-property relationship of nanocomposites based on polypropylene and LDH is investigated by a combination of DSC, SAXS, WAXS and BDS for the first time. The first thing that needs to be investigated in case of multicomponent systems like polymer nanocomposites is the homogeneity of the dispersed nanofiller.

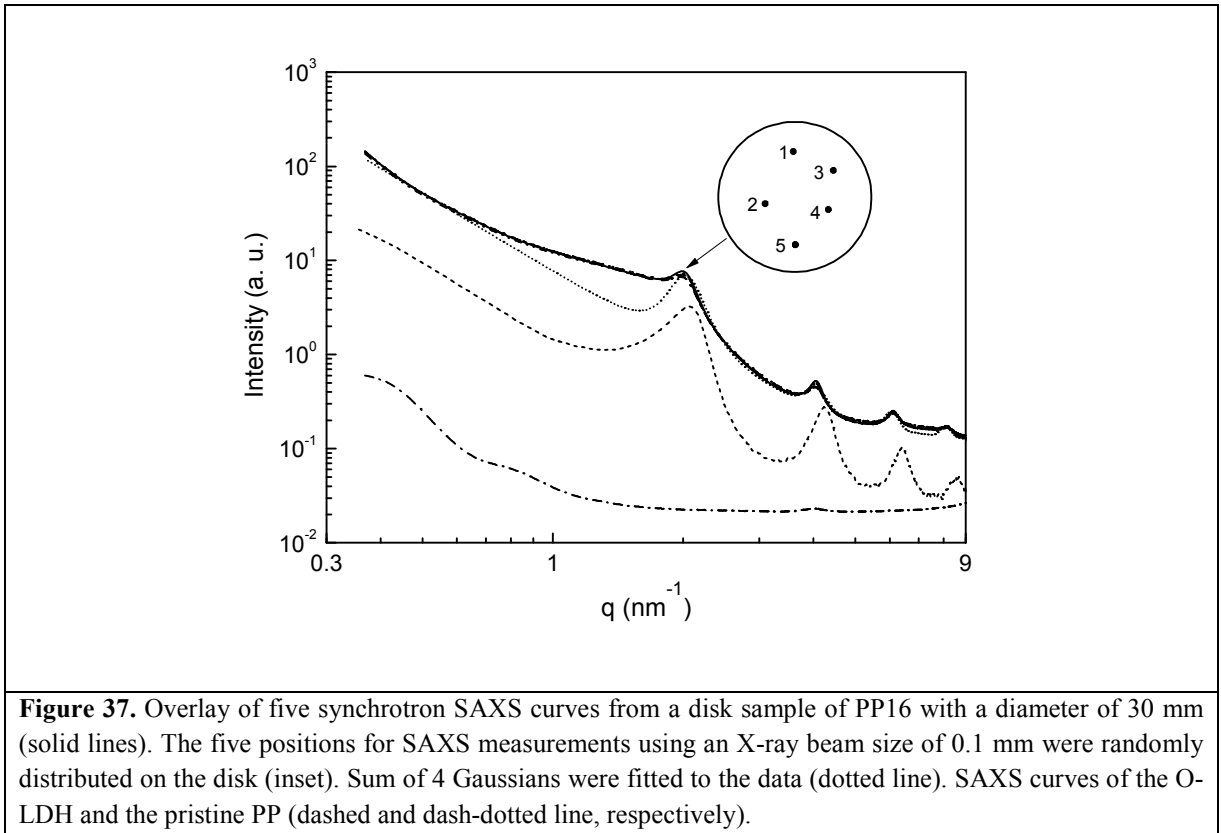
### **5.1 Homogeneity and SAXS analysis of the nanocomposites**

The homogenous distribution of the nanoparticles inside the polymer matrix across the whole macroscopic sample area is essential for the structure property relationships of nanocomposites. To investigate this for the prepared nanocomposites SAXS, measurements were performed with a microfocus using synchrotron radiation at the  $\mu$ SpotBeamline of BESSY.<sup>102</sup> The samples having a diameter of more than 30 mm were measured at five different positions with a spot diameter of 0.1 mm of the X-ray beam.

All the individual SAXS pattern collapse into one chart as shown exemplarily for PP16 in Figure 37 (solid curves, positions of measurements at the sample are shown in the inset). The finding of nearly collapsing scattering pattern is a strong indication for a homogeneous dispersion of O-LDH in the polymer matrix at a length scale of several cm.

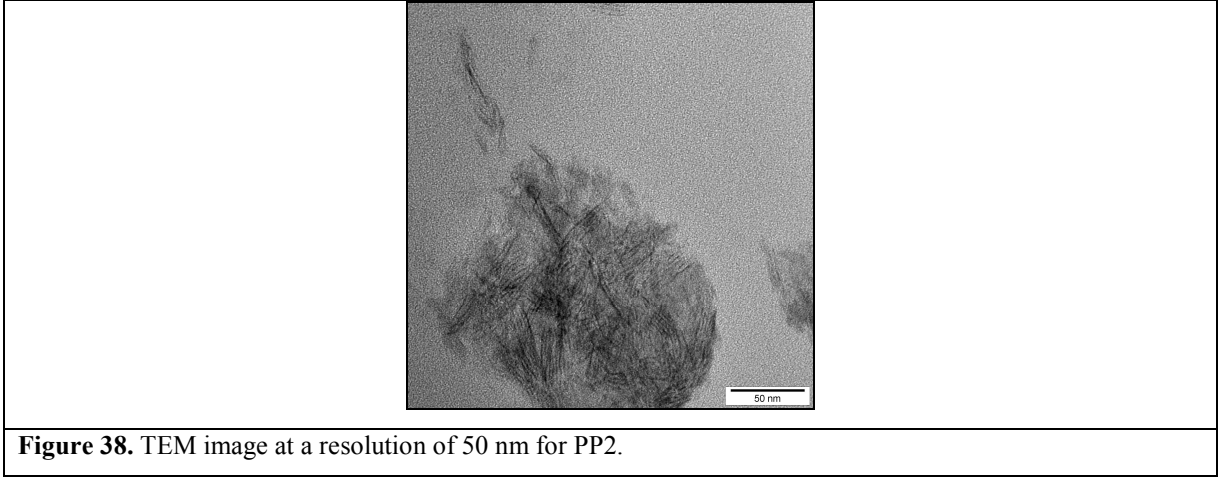
An analysis of the data using four equidistant Gaussians with the first maximum at  $2.02 \text{ nm}^{-1}$  was found to be appropriate (Figure 37, dashed curve). This position corresponds to a lamellar repeat unit of 3.11 nm and hints to a slight expansion of 0.17 nm in comparison to the O-LDH (2.94 nm). A similar expansion of the layer spacing from 2.95 nm to 3.27 nm has been reported earlier by Costa et. al.<sup>20</sup> They interpreted the expansion by partial intercalation

of polymer chain segments into the interlayer region of LDH as induced by strong shearing during melting in the extruder.

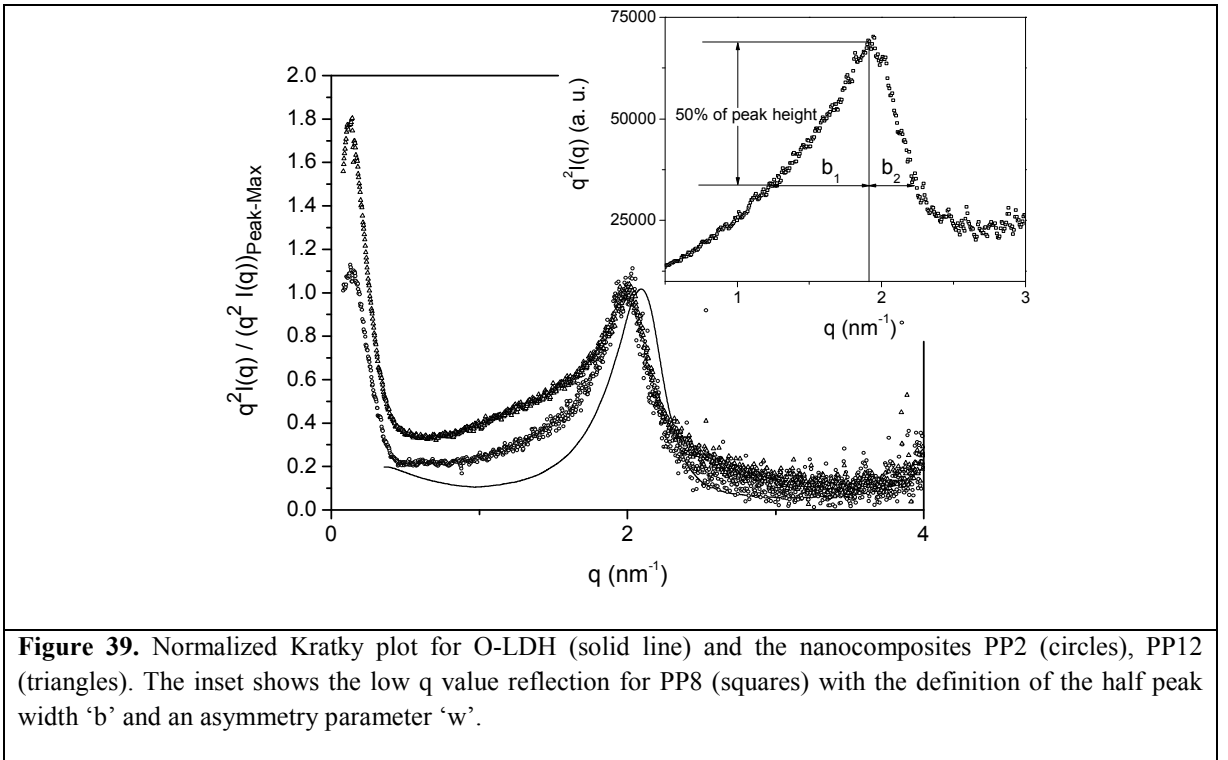


Peak widths of  $0.38 \text{ nm}^{-1}$  to  $0.50 \text{ nm}^{-1}$  are determined from fitting four equidistant Gaussians to the experimental curve. Therefore  $l_c$  is in the range of 12.6 nm to 16.5 nm, which is equivalent to 4.05 to 5.3 layers. This can be also concluded from the TEM image in Figure 38. Stacks of LDH (4 to 5 layers) are arranged in different orientations in the polymer matrix. For sake of comparison, the scattering of O-LDH and neat PP are displayed in Figure 37. It can be seen that the scattering intensity of PP can be considered as negligible for approximation in the region of the appearance of the reflections. The scattering pattern of the samples PP2 to PP12 is similar to PP16 with the same layer spacing and correlation lengths (not shown). Differences are found in the increase of the scattering intensity in the low  $q$ -range, whereas the scattering increases with increasing content of O-LDH. A simple explanation for this finding is that attractive interactions between neighboring nanoparticles become successively visible at higher LDH content.

It is concluded that the lamellar spacing of the O-LDH increases slightly after incorporation in the PP matrix while the height of the lamellar stack is constant.



In addition to the analysis presented in Figure 37, the peak in Figure 39 is background (pure PP) subtracted and plotted after applying the Lorentz correction [ $I(q) \rightarrow q^2 I(q)$ ] versus  $q$  (Kratky plot). The different data sets are normalized to the maximum peak position for comparison. A closer inspection of the scattering pattern in Figure 39 shows that for the nanocomposites the peak is quite asymmetric.



Therefore, to discuss these features in dependence on the concentration of the LDH, the half width ( $b$ ) and an asymmetry parameter ( $w$ ) are defined by using the following equation (see inset of Figure 39).

$$b = b_1 + b_2, w = \frac{b_1 - b_2}{b} \quad (43)$$

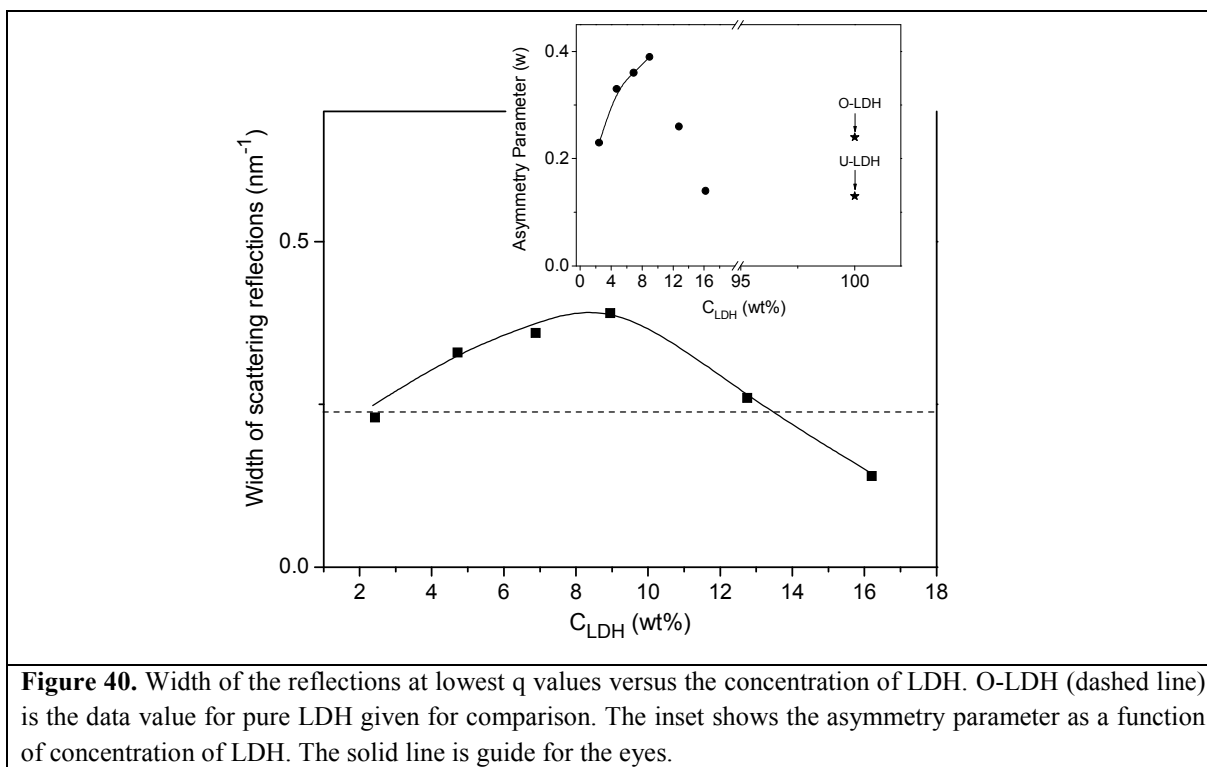
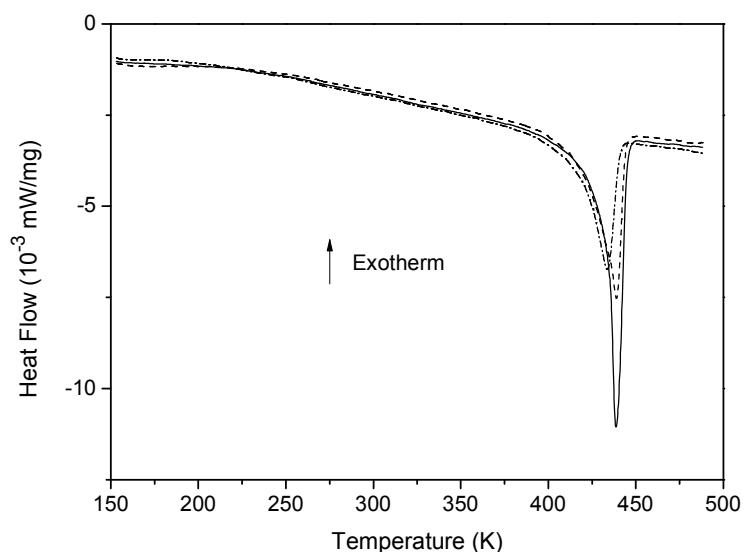


Figure 40 shows the change in the width of the low  $q$  scattering peaks. As it is observed from Figure 39, the peak widths increase asymmetrically. It is worth to note that only a symmetrical broadening of the diffraction peaks can be attributed to a reduction of the stack size. Therefore, the asymmetry of the Bragg peaks must be assigned to another molecular origin. The detailed analysis of the asymmetry parameter gives a result displayed in the inset of Figure 39. As result from the SAXS analysis, it was concluded that around 4 – 5 layers of LDH per stack are present in the nanocomposite. So, the asymmetry can arise from the arrangement of these stacks in different orientations in the polymer matrix. This can be also observed in the TEM image for low loading of LDH. This line of argumentation seems to be important for low concentration of stacks. For higher concentrations these different orientation are averaged out and the peaks for the samples PP12 and PP16 become more symmetric.

## 5.2 Crystallinity Investigation of the nanocomposites using Differential Scanning Calorimetry (DSC) and Wide angle X-ray Scattering (WAXS)



**Figure 41.** DSC curves for PP and corresponding nanocomposites (second heating run): solid line - PP; dashed line - PP8; dashed-dotted line - PP16. Inset gives the dependence of  $T_{\text{melt}}$  on the concentration of LDH. The solid line is guide for the eyes.

Thermal analysis was carried out by differential scanning calorimeter (DSC, Seiko instruments, DSC 220C). The samples (10 mg) were measured from 173 K to 473 K with a heating and cooling rate of 10 K/min using nitrogen as protection gas. The enthalpy changes related to melting and crystallization were calculated from 343 K to 453 K and 363 K to 408 K respectively. The following table displays the melting and crystallization temperature along with their enthalpies.

Figure 41 compares the DSC curves for the second heating run for PP, PP8 and PP16. At higher temperatures, a broad melting transition with a peak at  $T_{\text{melt}} \sim 438$  K takes place. In the inset of Figure 42 melting ( $\Delta H_{\text{melt}}$ ) and crystallization ( $\Delta H_{\text{crys}}$ ) enthalpies are plotted versus the concentration of LDH. (For sake of comparison the absolute values of  $\Delta H_{\text{melt}}$  and  $\Delta H_{\text{crys}}$  are plotted in the inset.)

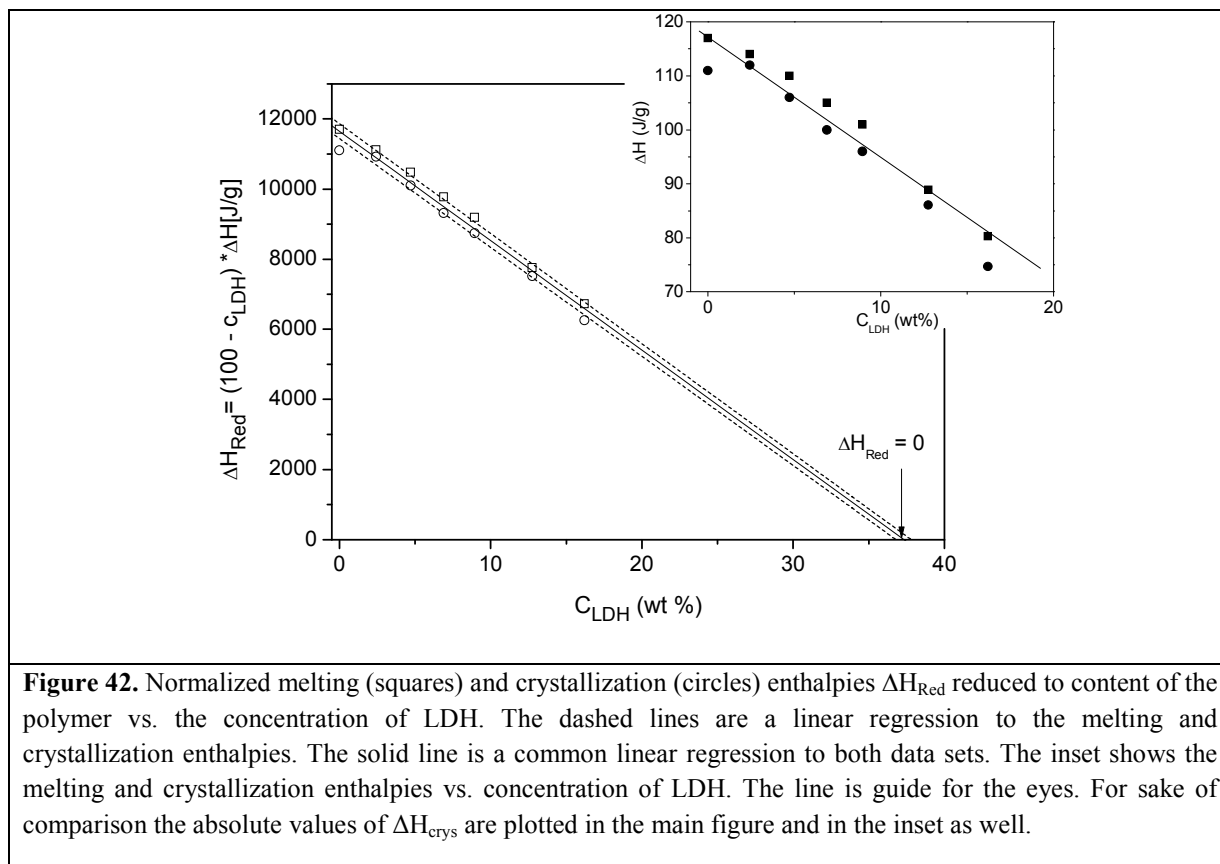
**Table 5.** Thermal data of the investigated nanocomposite samples. (here first and second melting is from DSC measurement)

Sample Information		1. Melting (1. heating)		Crystallization (cooling)		2. Melting (2. heating)	
Sample Code	Amount of LDH (wt%)	T <sub>m</sub> (K)	$\Delta H_{\text{melt}}$ (J/g)	T <sub>c</sub> (K)	$\Delta H_{\text{crys}}$ (J/g)	T <sub>m</sub> (K)	$\Delta H_{\text{melt}}$ (J/g)
PP	0	438.7	124	395.9	-111	438.6	117
PP2	2.43	441.5	141	400.1	-112	440.7	114
PP4	4.72	440.2	124	397.9	-106	440.5	110
PP6	6.89	439.8	130	396.9	-100	439.4	105
PP8	8.95	439.3	131	396.0	-96	438.8	101
PP12	12.75	441.4	108	394.5	-86.1	434.9	88.9
PP16	16.20	434.1	97.6	392.6	-74.7	433.7	80.3

As expected both quantities decrease with increasing concentration of LDH because the amount of polymer decreases with increasing content of LDH. Therefore, the enthalpy values have to be normalized to the content of the polymer. Also this normalized enthalpy values  $\Delta H_{\text{Red}}$  decreases linearly with increasing concentration of LDH where a similar dependence is obtained for melting and crystallization. Taking the enthalpy values as a measure for the degree of crystallization this indicates that the degree of crystallization decreases with increasing content of LDH. The extrapolation of normalized enthalpy to zero value results in a critical concentration of LDH of ca. 40 wt%. For concentrations above this value, the crystallization of PP will be completely suppressed. The nanoparticles can hinder the crystallization of PP segments. The same was observed for nanocomposites based on polyethylene containing MgAl-LDH<sup>22</sup> and nanocomposites made from polyamide and silica.<sup>47</sup> A similar analysis is reported by Lonjon et al. where they studied the decrease in crystallinity of poly(vinylidene difluoride-trifluoroethylene) as a function of gold nanowires content.<sup>114</sup> The limiting value of 40 wt% LDH for crystallization cannot be proved experimentally as it is difficult to prepare nanocomposite sample with such a high concentration of nanofiller.



It should be noted that for other systems, an increase of crystallization rate and also more perfect crystals were observed for low concentration of nanofiller because the nanoparticles can act as additional nucleation sites.<sup>115,116</sup> So the observed behavior might depend on the type of system studied.



In addition to DSC, WAXS is employed to estimate the degree of crystallinity for the nanocomposites directly. The observed dependence on the concentration of LDH estimated by WAXS can be compared with the data obtained from the DSC experiments. The measured WAXS pattern is due to both contributions of the amorphous and crystalline polypropylene. Therefore, the values for the degree of crystallinity  $\chi$  were determined through peaks of crystalline and amorphous fractions deconvolution process using the software OriginPro, release 8.5, and its *Peak Fitting* tool. Peaks deconvolution was performed using Gaussian functions to obtain the areas due to the crystalline and amorphous fractions ( $I_{\text{crystalline}}$  and  $I_{\text{amorphous}}$ , respectively).

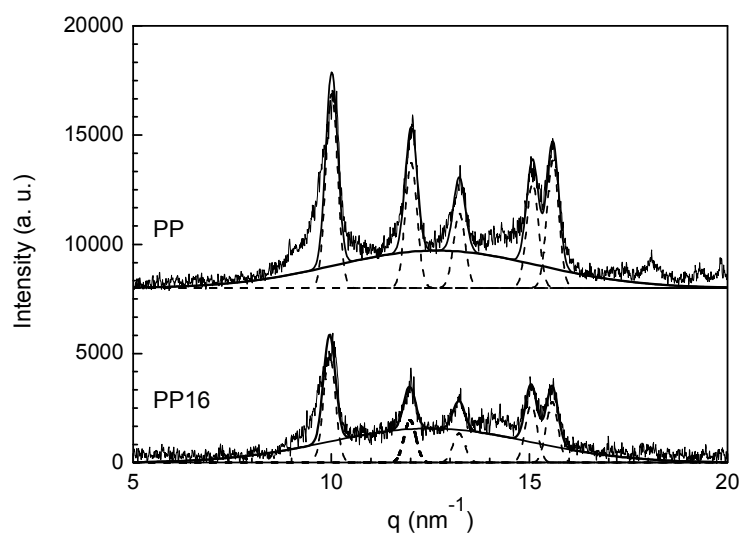


**Figure 43.** WAXS pattern for the sample PP and PP16 (solid lines in upper and lower curve, respectively). The amorphous contributions are indicated (solid lines) and the crystalline contributions (dashed lines). The degree of crystallinity is 49% (PP) and 31% PP16. For details see the text.

The  $\chi$ -values were determined with these areas by using the relation between the total area of the crystalline peaks and the total area of the diffractogram given in Eq. 37.

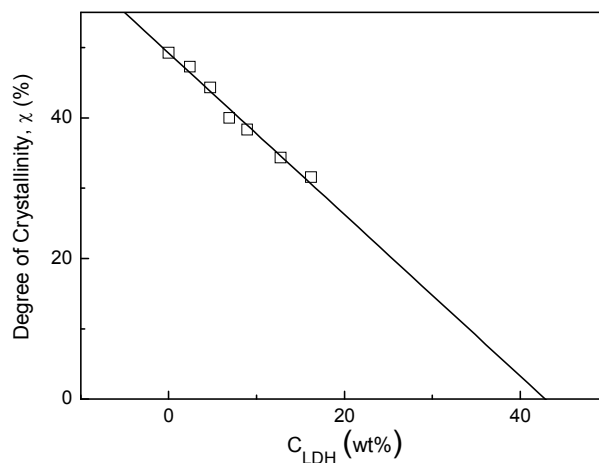


**Figure 44.** Degree of crystallinity  $\chi$  vs. the concentration of LDH. The solid line is a linear regression to the data.

Figure 44 shows that  $\chi$  decrease with increasing concentration of LDH. The result is in agreement with the DSC results. The extrapolation of the  $\chi$  to zero gives a concentration of

ca. 42wt % of LDH where there are no crystallites present in the polymer. This limiting value estimated from WAXS measurements is approximately equal to the value obtained by DSC (40wt %). This can be considered as a strong conclusion, due to the fact that both the techniques DSC and WAXS measure slightly different aspects of the same material's phenomenon. In case of DSC, the crystallinity is determined by relating it to the measured enthalpy changes of the system whereas, for WAXS direct information of the molecular structure is obtained by X-ray diffraction. Even for WAXS absolute values can depend on the employed method of analysis.

### **5.3 Dielectric Relaxation Spectroscopy (BDS)**

As mentioned in Chapter 4, section 4.2.1.1, the dielectric behavior of polymers with a high degree of crystallinity like polypropylene in general follows a different nomenclature of relaxation processes as compared to amorphous polymers. The detailed analysis employing BDS is discussed hereafter.

BDS was measured as a function of frequency  $f$  ( $10^{-1}$  Hz to  $10^6$  Hz) and temperature  $T$  (173 K to 393 K). The dielectric response of pure PP is weak, because the asymmetry in the repeating unit of polypropylene leads only to a low dipole moment. The dielectric spectra of pure polypropylene show one main relaxation process indicated by a peak in the dielectric loss. With increasing temperature its shifts to higher frequencies as expected. This process is called  $\beta$ -relaxation and corresponds to the dynamic glass transition related to segmental fluctuations. At lower temperatures (higher frequencies) than the  $\beta$ -relaxation a  $\gamma$ -relaxation is observed which corresponds to localized fluctuations as discussed in more detail later in this chapter.

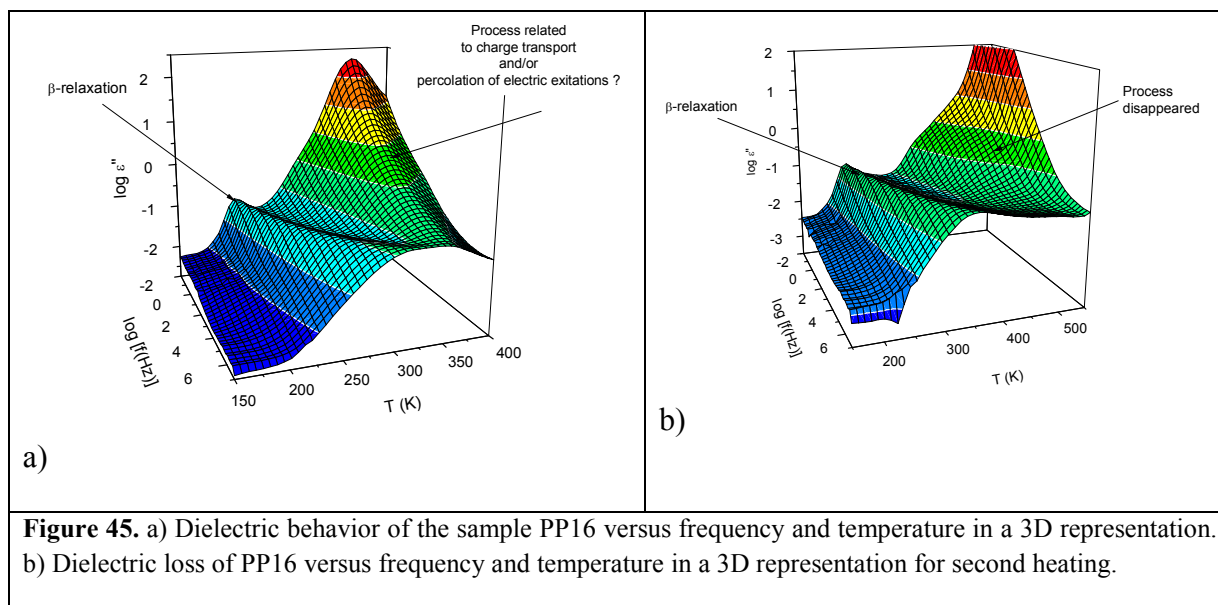
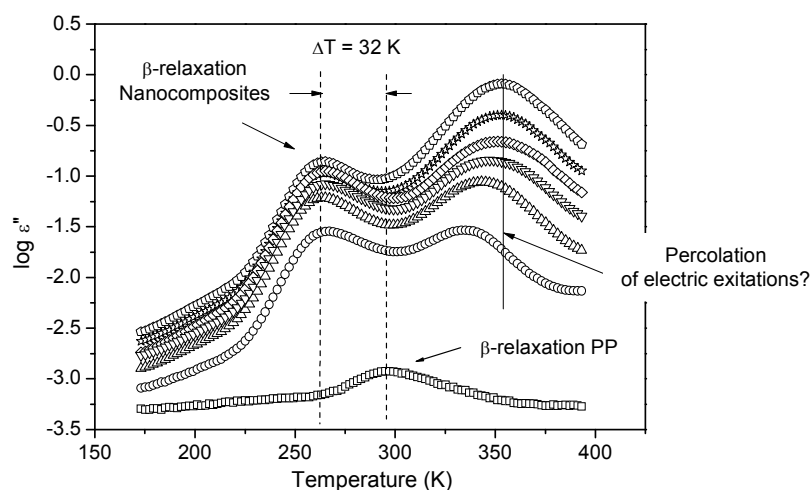


Figure 45a shows the dielectric spectra for the nanocomposite PP16 also in a 3D representation. At lower temperature/higher frequency the  $\beta$ -relaxation is observed like for pure PP. Its intensity is strongly increased compared to that of pure PP. This will be discussed in detail later. At higher temperatures a further dielectrically active process is observed. This process has some specific peculiarities (see Figure 45). Firstly, its dielectric strength decreases strongly with increasing frequency. Secondly, the position of the maximum of dielectric loss is independent of temperature. These characteristics indicate that this mode is not a relaxation process related to the molecular mobility of molecular dipoles etc. It was discussed by Pissis et al. that such specific features of a dielectric process are due to percolation.<sup>117</sup> In a series of papers Feldman et al. applied dielectric spectroscopy to study the percolation of electric excitations through porous silica glasses with a random structure of interconnected pores.<sup>118-120</sup> From the analysis of the dielectric spectra quantitative information was deduced about the fractal nature of the pores and the porosity. In the case of the system considered here exfoliated and/or small stacks of LDH layers are present which have a huge amount of interfacial area and porosity. Therefore, these concepts of the percolation of electric excitation might also apply. Moreover, this peak disappears after heating up the sample (see Figure 45b). Therefore, it might be also due to the preparation of the nanocomposites. However, a weak peak which is frequency dependent can be recognized, which might be assigned to MWS polarization.



**Figure 46.** Dielectric loss  $\epsilon''$  versus temperature  $T$  at a frequency of 1 kHz for PP (squares) and different nanocomposites: PP2 (circles), PP4 (triangles), PP6 (inverted triangles), PP8 (rhombus), PP12 (stars) and PP16 (pentagons).

Figure 46 shows the dielectric behavior of nanocomposites in the temperature domain at a fixed frequency of 1 kHz in dependence on the concentration of LDH. A strong increase in the intensity of the  $\beta$ -relaxation with increasing concentration of LDH is observed as compared to pure PP. The increase in the measured dielectric loss with the concentration of LDH is due to an increase in the concentration of polar molecules. In the current case it is the bulky anionic surfactant (SDBS) which is the only polar component which increases with increasing concentration of LDH.<sup>20</sup> In the presence of a weakly polar molecule (grafted polypropylene) the polar head group of the SDBS ionically interacts with the surface of the LDH layer while the alkyl tail is desorbed from the layers and forms a common phase with the polypropylene segments. The polar surfactant molecules are fluctuating together with the weakly polar polypropylenes segments and monitor the molecular mobility of the latter ones. Therefore, an increasing dielectric loss is observed with increasing concentration of LDH. This case is similar to the probe technique used to study the dielectric behavior of polyolefins.<sup>121,122</sup> In the case considered here, the SDBS molecules are predominantly located or adsorbed at the LDH layers. So BDS here probes the molecular mobility of segments located in an interfacial area close to the LDH sheets because the dielectric loss of pure polypropylene is by orders of magnitude lower and so the matrix of the nanocomposite can be regarded as dielectrically invisible. In order to prove this directly a sample with SDBS and PP (without LDH) should be synthesized and measured. Unfortunately, no stable

samples of this kind can be prepared because the SDBS molecules will migrate, aggregate or even phase separate.

### **Dynamic glass transition ( $\beta$ -relaxation)**

In the following first the  $\beta$ -relaxation process is analyzed in detail. Compared to pure polypropylene for the nanocomposites the position of the  $\beta$ -relaxation is shifted by ca. 30 K to lower temperatures (see Figure 46). This leads to the conclusion that the molecular mobility in the interfacial region between the LDH layers and the matrix is higher than that in the bulk unfilled PP. This corresponds to a decreased glass transition temperature in that interfacial region compared to pure PP. Usually the model function of Havriliak-Negami (HN)<sup>87-89</sup> is used to analyze relaxation processes quantitatively (Eq. 31). Because of the fact that pure PP has only a weak dielectric response, it was difficult to fit the HN function in the frequency domain to the data unambiguously. For this reason, the dielectric spectra were analyzed in the temperature domain where Gaussians were fitted to the data (Eq. 32), in order to determine the mean relaxation rates at different temperatures. The method was described in detail in Ref 91. It was shown that the analysis carried out in the frequency and the temperature domain leads to identical results.<sup>91</sup> A similar method of data analysis in the temperature domain based on the HN-function is published elsewhere.<sup>123</sup>

Figure 47 displays the dielectric loss of the nanocomposite PP16 at  $T = 273.2$  K versus frequency. At higher frequencies a well defined loss peak can be observed (see also Figure 45). A more careful inspection of this peak shows that it has a pronounced low frequency contribution which originates from a further relaxation process. A fit of the data by only one HN-function results in a parameter set with unreasonable values. In principle the data can be described by fitting a superposition of two HN-functions to the data (see Figure 47). Unfortunately this procedure results in highly scattered parameter values especially for the frequency position of the low frequency relaxation process. Therefore, like for pure polypropylene, for the nanocomposites the isochronal plots are analyzed where two Gaussians were fitted to the data. An example for this procedure is given in Figure 48. This strategy of data analysis leads to stable fitting results. Moreover, for pure polypropylene and its nanocomposites a consistent evaluation strategy is employed.

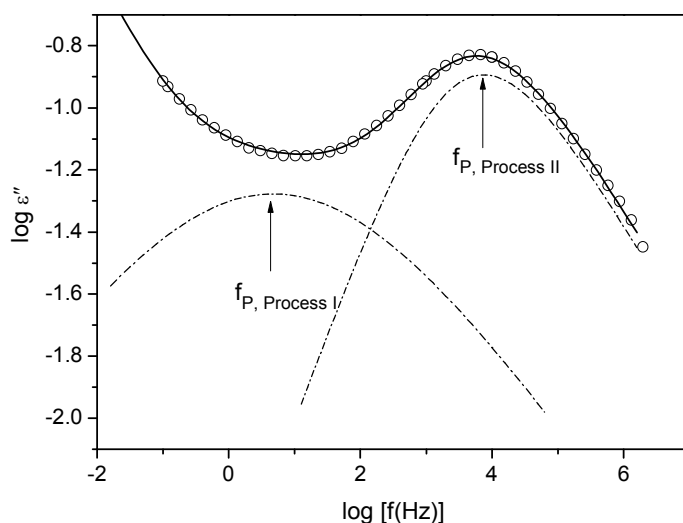


**Figure 47.** Dielectric loss vs. frequency for the sample PP16 at  $T = 273.2$  K. The solid line is a fit of two HN-functions to the data including a conductivity contribution. The dashed-dotted lines correspond to individual relaxation processes. For details see text.

The two processes observed for the nanocomposites are assigned to different regions of the molecular mobility of PP segments depending on the distance from the surface of the LDH sheets.<sup>124,125</sup> There are only few literatures which consider adsorption of surfactant to the layers of the nanofiller. In the presence of most intercalates the alkyl tails are desorbed from the surface of the nanoparticles and mixed with the polymer segments.<sup>124</sup> Room temperature NMR studies show that the disorder and the relaxation rates increase from the polar head group to the methyl terminus of the surfactant.<sup>124,125</sup> In the case considered here a similar picture is assumed. Process I appearing at lower frequencies is assigned to the PP segments in close proximity of the LDH layers. Their mobility is hindered by the strong adsorption of the polar head group of the surfactants at the LDH layers. A similar result is found for poly(ethylene oxide)/laponite nanocomposites by NMR.<sup>126</sup> Process II at higher frequencies is related to the fluctuations of the PP segments at a farer distance from the LDH sheets. Moreover, Lonkar et al. have proposed a model where the grafted units of maleic anhydride react with the sulfonate end of the surfactant.<sup>127</sup> This model is in the line with the arguments discussed above. Moreover, it is worthy to note that a similar assignment is used to describe the relaxation behavior of PE/Mg-AL-LDH nanocomposites.<sup>22</sup> There might be a possibility that PP-g-MAH also contributes to Process II, unfortunately no sample was available to

prove this. However, there is no influence of the grafted polymer which is proved for PE/LDH nanocomposites in Chapter 6.

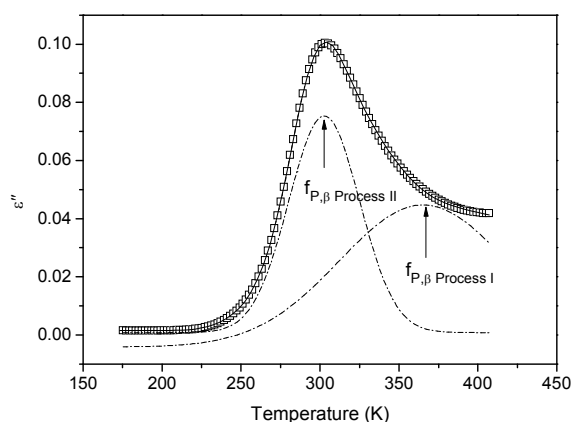


**Figure 48.** Dielectric loss versus temperature for the sample PP12 at a fixed frequency of  $2.95 \cdot 10^5$  Hz. The solid line is the fit of the superposition of two Gaussians to the data were the dashed dotted lines give the individual contributions. Typical values of the regression coefficients for the fits are  $r^2=0.999$ .

The relaxation map for pure polypropylene and the corresponding nanocomposites is given in Figure 49. For each data set of the  $\beta$ -relaxation, the temperature dependence of the relaxation rate is curved when plotted versus  $1/T$ . The data can be well described by the VFTH equation (Eq. 2). The fragility parameter was also determined using Eq. 3 for comparison of molecular mobility of the nanocomposites as compared to bulk PP.

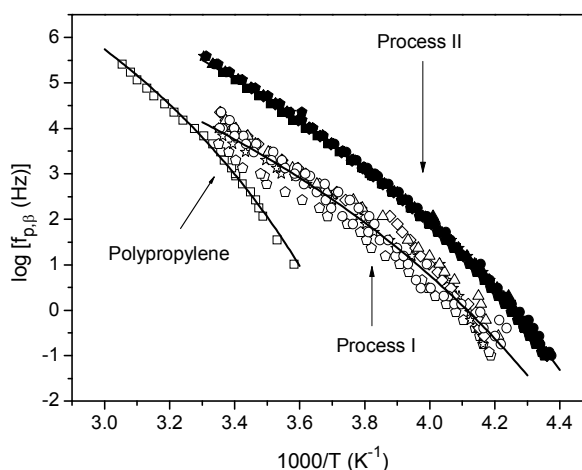


**Figure 49.** Relaxation rates ( $f_{p,\beta}$ ) vs.  $1000/T$  for pure polypropylene and both the relaxation processes for the nanocomposites. Pure PP (squares), open symbols (Process I) and closed symbols (Process II), PP2 (circles), PP4 (triangles), PP6 (inverted triangles), PP8 (rhombus), PP12 (stars) and PP16 (pentagons). The solid lines are fits of the VFTH Equation to the different data sets. For the fitting procedure see the text.



Figure 49 shows firstly that the relaxation rates of the nanocomposites collapse in the same curve for all concentrations of the nanofiller. This is true for both relaxation processes although the data for process I show a larger scatter. Secondly, the temperature dependence of the relaxation rate for the  $\beta$ -relaxation of pure polypropylene is strongly different from that of the two processes observed for the nanocomposites showing a different curvature when plotted versus  $1/T$  and different values for the Vogel temperature. This indicates that a different glassy dynamics takes place for the nanocomposites in comparison to pure polypropylene. This is discussed in more detail in the following section.

For the fit of the relaxation rate by the VFTH-equation a value of 12 was fixed for the log of the pre-exponential factor to reduce the number of free fit parameter. For the nanocomposites the relaxation rates do not depend on the concentration of the nano-filler. Therefore for the fitting of the VFTH equation the values for all concentration were used in a common analysis. This procedure results in average values for  $A_0$  and  $T_0$  with high statistical significance. The obtained VFT fit parameters for pure PP and processes I and II observed for the nanocomposites are shown in the following table.

**Table 6.** Estimated VFT parameters for Pure PP and processes I and II with fixed  $\log [f_\infty (\text{Hz})] = 12$ .  $D$  is the fragility parameter and  $T_g^{\text{diel}}$  is the dielectric glass transition temperature (see text)

	$\log [f_\infty(\text{Hz})]$	$A_0$ (K)	$T_0$ (K)	$T_g^{\text{diel}}$ (K)	$D$
<b>PP</b>	12	803	205	277	9
<b>Process I</b>	12	1307	$134 \pm 5$	252	22.5
<b>Process II</b>	12	955	$155 \pm 2$	242	14.2

There is a large difference in the estimated values of the VFT parameters of bulk polypropylene and that of the nanocomposites. For pure PP the molecular mobility across the whole matrix is measured whereas for the nanocomposites the interfacial region between the LDH layers and the polypropylene matrix is selectively monitored. From the VFT parameters a dielectric glass transition temperature can be calculated for instance by  $T_g^{\text{diel}} = T (f_p = 10 \text{ Hz})$  (see Table 6). The dielectric glass transition temperature for polypropylene located in the interfacial area is by more than 20 K lower than that of the bulk. This downshift in  $T_g^{\text{diel}}$  is accompanied by a stronger behavior of the whole relaxation

processes compared to pure PP. These differences point to a difference in the physical structure of polypropylene in the bulk and polypropylene located in the interfacial area. A more careful inspection of the estimated parameters for relaxation process I and II reveal that there is also a difference between these two modes. The Vogel temperature of process I is 20 K lower than that of process II. Moreover, process I behaves more fragile. These findings lead also to a 10 K higher dielectric glass transition temperature for process I. Hence, one has to conclude that the molecular dynamics in the interfacial region around the LDH sheets is also different. A temperature dependence of the relaxation rates according to the VFT equation is regarded as a sign of glassy dynamics. Therefore, it is concluded that both of the observed relaxation processes are due to a dynamic glass transition in spatial regions with different distance to the LDH layers. As mentioned in Chapter 2, to have a signature as a glass transition the spatial extent of these regions should be in the order of 1 to 3 nm. So it is further concluded that the thickness or the extension of the interfacial region into the bulk matrix is about the same length scale.

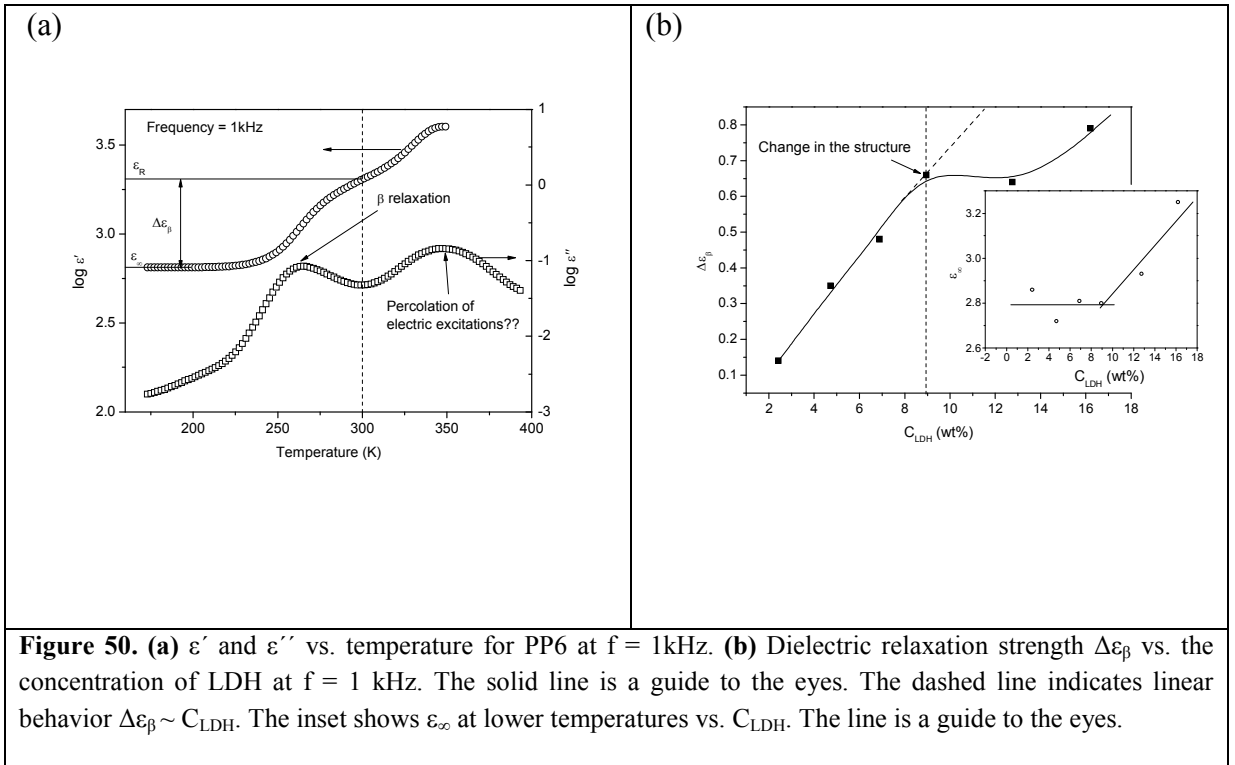


**Figure 50. (a)**  $\epsilon'$  and  $\epsilon''$  vs. temperature for PP6 at  $f = 1$  kHz. **(b)** Dielectric relaxation strength  $\Delta\epsilon_\beta$  vs. the concentration of LDH at  $f = 1$  kHz. The solid line is a guide to the eyes. The dashed line indicates linear behavior  $\Delta\epsilon_\beta \sim C_{LDH}$ . The inset shows  $\epsilon_\infty$  at lower temperatures vs.  $C_{LDH}$ . The line is a guide to the eyes.

The dielectric strength of the  $\beta$ -relaxation  $\Delta\epsilon_\beta = \epsilon_R - \epsilon_\infty$  is estimated as follows (see Figure 50a). The real part of the complex dielectric function is plotted versus temperatures at a fixed frequency of 1 kHz.  $\epsilon_\infty$  is taken as value of  $\epsilon'$  at the lowest temperatures. To minimize the influence of the high temperature percolation process  $\epsilon_R$  is taken as the value of the dielectric

permittivity where the dielectric loss  $\epsilon''$  shows the minimum between the  $\beta$ -relaxation and the high temperature mode.

$\Delta\epsilon_\beta$  is plotted versus the concentration of LDH in Figure 50b. At low concentrations of LDH  $\Delta\epsilon_\beta$  varies linearly with  $C_{LDH}$  as expected from Eq. 1. This linear dependence proves the increasing number of SDBS molecules. There is a change in this linear behavior for concentrations higher than 8.95% which may be due to some structural changes because of high loading of LDH in the polymer. For such high concentration of LDH the nanoparticle cannot arrange independently from each other. The inset of Figure 50b shows that  $\epsilon_\infty$  is nearly constant up to same concentration of LDH and increases for PP12 and PP16, which can be taken as an additional indication for a change of the structure at higher loadings. The presence of rigid amorphous fraction (RAF) at the interface of the polymer and LDH cannot also be neglected. As at higher concentrations the amount of LDH increases the interfacial area. A detailed discussion about RAF is given later in this chapter.

### $\gamma$ -relaxation

In the temperature range between 190 K and 230 K the dielectric spectra show a further relaxation process which is called  $\gamma$ -relaxation (Figure 51). It corresponds to the localized fluctuations within the amorphous regions. The analysis of the  $\gamma$ -relaxation was performed by fitting the HN function to the data. It is characterized by a symmetric peak with  $\beta$  values between 0.2 and 0.45. The estimated relaxation rates ( $f_{p,\gamma}$ ) were plotted versus inverse temperature (Figure 52).

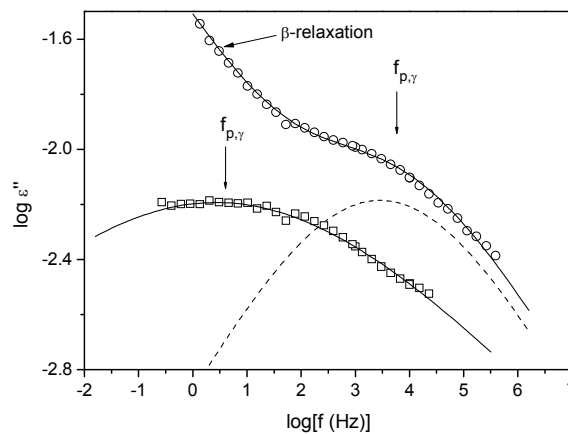


**Figure 51.** Dielectric loss  $\epsilon''$  versus frequency  $f$  showing the  $\gamma$ -relaxation for the sample PP16 nanocomposite at temperatures 193 K (squares) and 223 K (circles). The solid lines represent the HN fits to the data; dotted line is the contribution to the  $\gamma$ -relaxation at 223 K.

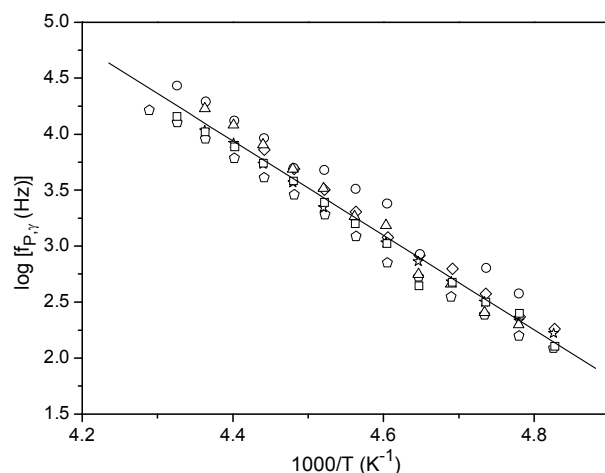


**Figure 52.** Relaxation rate versus inverse of the temperature for ZnAl LDH nanocomposites: PP2 (squares), PP4 (circles); PP6 (triangles), PP8 (rhombus), PP12 (stars), PP16 (pentagons). Solid line is a linear fit to the data.

Figure 52 shows that the temperature dependence of the relaxation rate for the  $\gamma$ -relaxation follows the Arrhenius Eq. 1 as expected.

The relaxation rate values for all the nanocomposites are collapsing into one chart and there is no difference due to the composition. The estimated activation energies are between 77 and 94 kJ/mol.

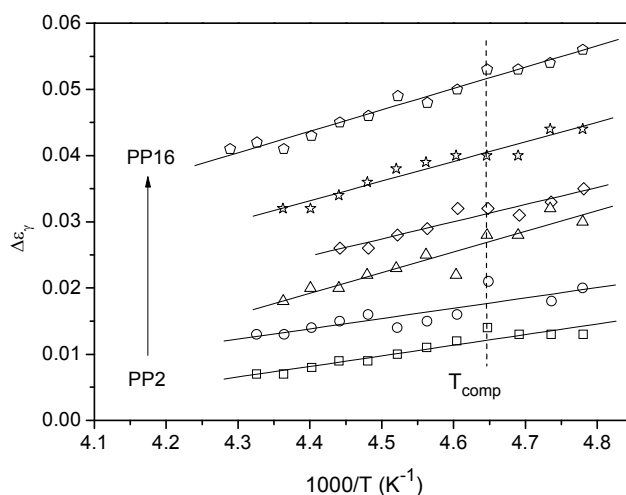
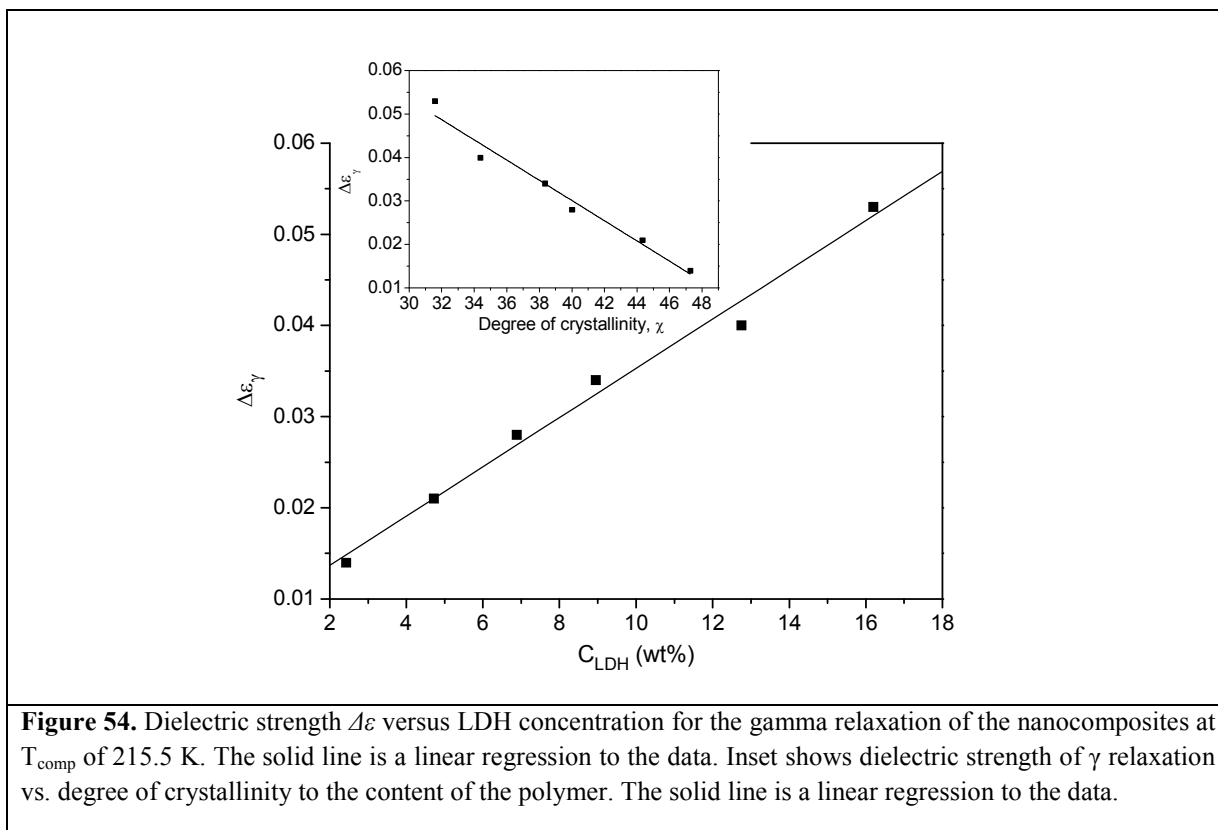


**Figure 53.** Dielectric strength  $\Delta\epsilon_{\gamma}$  versus inverse temperature for the  $\gamma$ -relaxation: PP2 (squares), PP4 (circles); PP6 (triangles), PP8 (inverted triangles), PP12 (stars), PP16 (pentagons). Lines are linear regressions to the corresponding data.

The  $\gamma$ -relaxation is a phenomenon related to the amorphous domains of the polymer matrix. From the analysis of the data the dielectric strength  $\Delta\epsilon_\gamma$  for the  $\gamma$ -relaxation is obtained for each concentration and plotted versus inverse temperature (Figure 53). With increasing content of the nanofiller,  $\Delta\epsilon_\gamma$  increases. As discussed above with increasing content of LDH the degree of crystallization decreases and therefore the relative amount of the amorphous phase increases. This line of argumentation is supported by the linear dependence of  $\Delta\epsilon_\gamma$  on the  $C_{LDH}$  (see Figure 54).

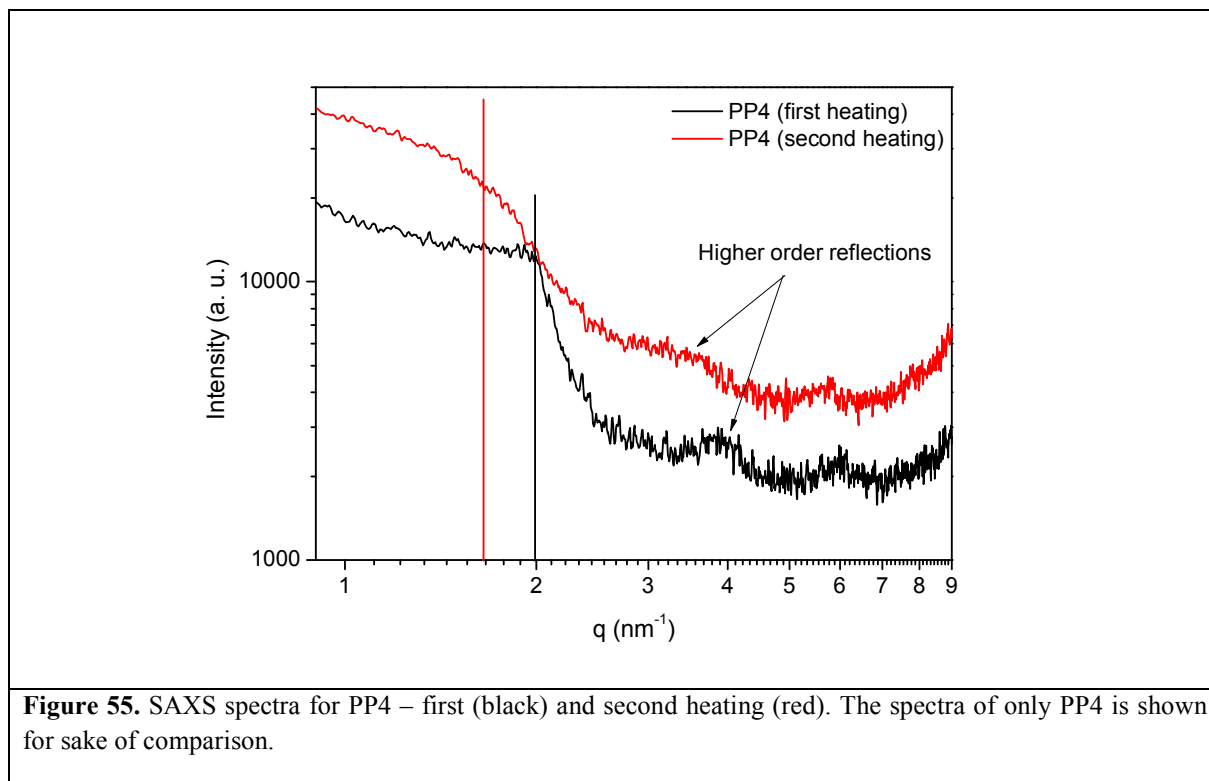


If the  $\gamma$ -relaxation occurs only in the amorphous part of the polymer, then the dielectric strength associated to this process should increase as the crystallinity decreases. The degree of crystallinity ( $\chi$ ) obtained from WAXS is plotted in the inset of Figure 54. The inset of Figure 54 confirms that the dielectric strength decreases as the sample becomes more amorphous. Therefore, this observation supports the hypothesis that the  $\gamma$ -relaxation takes place in the amorphous part of the polymer matrix.

### ***Second heating (BDS)***

In addition to the results discussed in detail above, BDS measurements were carried out during cooling (393 K to 173 K) and second subsequent heating (173 K to 453 K). The samples after this measurement were also measured by in house SAXS. A change in the molecular dynamics was observed due to the heating process.

First the SAXS results will be discussed shortly.



The low  $q$  value reflection which is related to mainly LDH is symmetrically broadened for PP4 and also the peak position has shifted to further lower  $q$  values as compared to first heating spectra. From SAXS analysis for first heating samples, it was concluded that the nanocomposites have a dominantly intercalated morphology. However, it is known that a symmetric broadening of the peak is related to decrease in stack size and hence more exfoliated morphology. Moreover, also the shift of  $q_{\text{peak}}$  to lower value indicates an increase in the  $d$ -spacing between the LDH sheets. These two conclusions hint to a dominantly exfoliated morphology of the nanocomposites formed during the second heating. Further BDS investigations will highlight these findings from SAXS.

Figure 56a shows the dielectric loss versus temperature for the second heating at 1 kHz. The findings are drastically different as compared to the first heating. The process at higher temperatures does not appear anymore. As already mentioned, its origin might be due to the

water trapped in the crystal structure of LDH (percolation of electric excitations) has evaporated during the heating and so the disappearance of the process.

With increasing concentration of the nano-filler the temperature shifts to lower values until it reaches a plateau for the concentrations higher than 6%. The temperature where the dynamic glass transition is detected changes dramatically at lower concentrations.

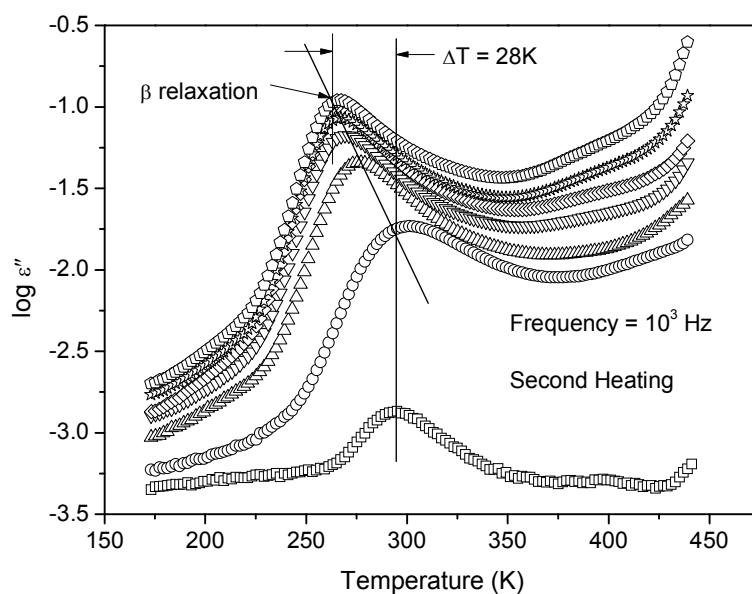
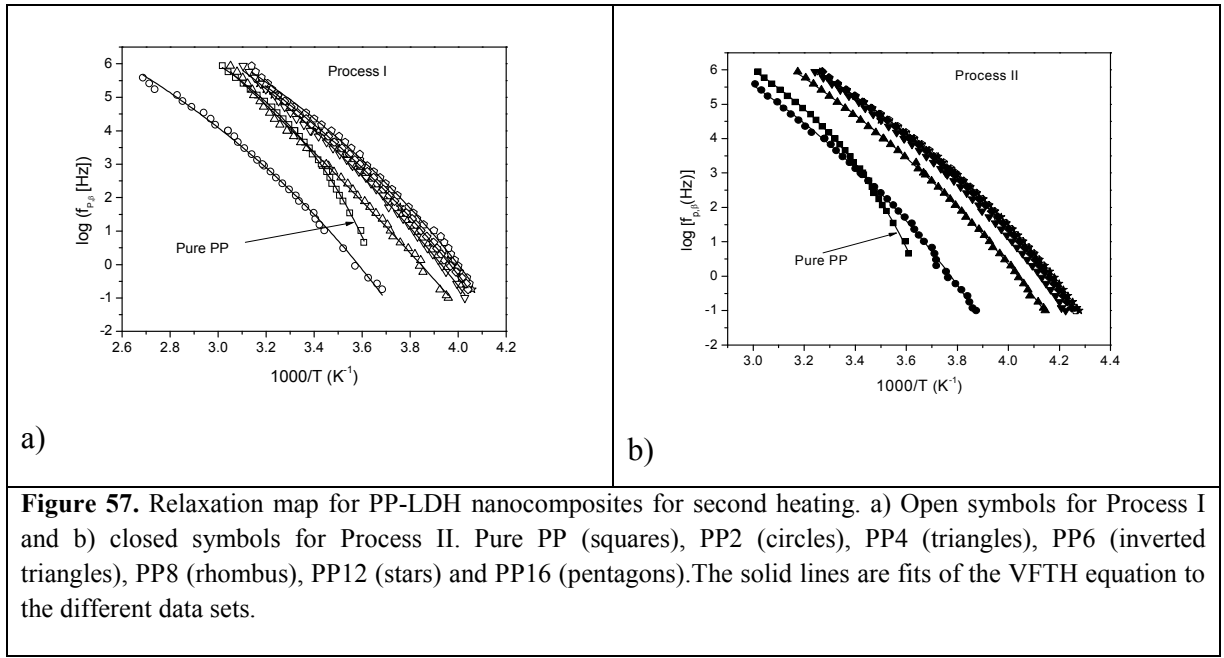


**Figure 56.** Dielectric loss  $\varepsilon''$  versus temperature  $T$  at a frequency of 1 kHz (second heating) for PP (squares) and different nanocomposites: PP2 (circles), PP4 (triangles), PP6 (inverted triangles), PP8 (rhombus), PP12 (stars) and PP16 (pentagons).

As discussed for first heating, the increase in dielectric loss is due to the increase in the polar molecules i.e. SBDS. The polar head group of this bulky anionic molecule interacts with the LDH sheet and the alkyl tail forms a common phase with the PP segments.



A similar fitting procedure as for first heating (fitting in temperature domain, Eq. 32) was employed for the analysis of the relaxation spectra for second heating.

**Table 7. VFT parameters for Processes I & II.**

	<b>Process I</b>				<b>Process II</b>			
<b>Sample Codes</b>	<b><math>\log[f_{\infty}(\text{Hz})]</math></b>	<b><math>A_0</math> (K)</b>	<b><math>T_0</math> (K)</b>	<b><math>T_g^{\text{diel}}</math> (K)</b>	<b><math>\log[f_{\infty}(\text{Hz})]</math></b>	<b><math>A_0</math> (K)</b>	<b><math>T_0</math> (K)</b>	<b><math>T_g^{\text{diel}}</math> (K)</b>
PP	-	-	-	-	11	461	229	276
PP2	12	1256	174	279	12	1153	175	265
PP4	12	986	178	260	12	1264	156	247
PP6	12	931	177	255	12	1076	160	243
PP8	12	942	173	252	12	1071	159	240
PP12	12	974	170	252	12	1041	159	239
PP16	12	917	173	250	12	994	162	239

Figure 57 (a) and (b) shows the relaxation map for the corresponding nanocomposites for process I and II respectively. As it can be seen from Figure 57, process I which corresponds to the fluctuations of the molecules close to LDH, PP2 occurs at higher temperatures as



compared to pure PP. The other compositions occur at temperature lower than pure PP. Similarly, process II occurs at lower temperatures as compared to pure PP for all the nanocomposites. In both the cases, the temperature dependence of the mean relaxation rates becomes concentration independent after PP6 as they all nearly collapse with each other.

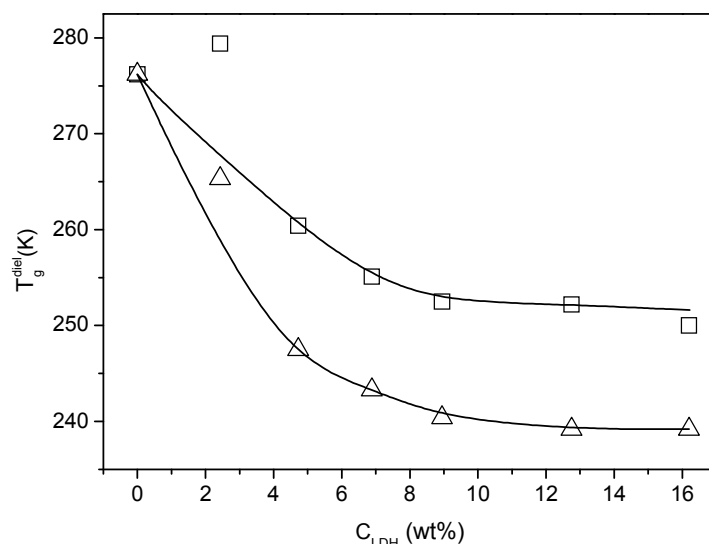


**Figure 58.** The dependence of the  $T_g^{diel}$  on the content of LDH for process I (squares) and process II (triangles). The solid lines are guide for the eyes.

Figure 58 shows the dependence of the change in  $T_g^{diel}$  as a function of LDH content for process I and II due to second heating.

This result gives the following model of the nanocomposites.

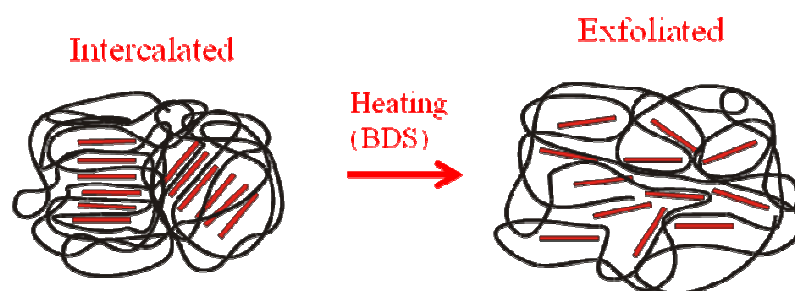


**Figure 59.** Change in nanocomposites morphology, due to the heating scan during BDS measurement. It should be noted that always a combination of the morphologies exist with a domination of one type.

The schematic representation of the influence of a heating scan on the nanocomposites morphology is shown in Figure 59. Such a model answers the different molecular dynamical

behavior of the nanocomposites as compared to first heating. Due to the heating, the intercalated order of the LDH is disturbed and thus they delaminate. This is also clear from the decrease in  $T_g^{\text{diel}}$  values. From earlier discussions, it is known that the head group of the SDBS molecules is attached to the LDH and the alkyl tail to the PP segments. Such a delamination process allows the SDBS to disperse in the polymer matrix. So the SDBS acts like a plasticizer and thus the processes occur at lower temperatures as compared to pure PP. In other words, the molecular mobility of the probed SDBS molecules increases. At higher concentrations, due to high amount of LDH (100 nm X 10 nm size), the molecular mobility of the delaminated nanocomposite is restricted and so it becomes concentration independent after PP6. In order to further prove this theory of process I and II additional thermal analysis is done. A presence of an immobilized polymer layer close to LDH is proved.

#### **5.4 Extended thermal investigations using Temperature Modulated DSC**

Obtaining information about different phase transitions in the polymers needs experimental methods which are sensitive to the dynamics of the polymer chains and which can be easily applied to multicomponent systems. Differential scanning calorimetry (DSC) is such a technique, and it is widely used to characterize polymer nanocomposites. Changes in crystallization, melting and glass transition behavior can be detected and have been reported frequently.<sup>22,35,36,128,133</sup> However, so far only minor attention has been paid to deduce the existence of an interphase in inorganic/polymer nanocomposites from DSC curves. Privalko et al.<sup>129,130</sup> used specific heat capacity to identify a fraction of reduced mobility in nanocomposites. Pissis et al.<sup>131,132</sup> applied different relaxation experiments like dielectric spectroscopy and TSDC (thermally stimulated depolarization current) to determine an immobilized fraction in the nanocomposites as a function of the nanofiller concentration. The existence of a rigid amorphous fraction in poly(methyl methacrylate) (PMMA)/SiO<sub>2</sub> nanocomposites based on heat capacity measurements at the glass transition of the polymer has already been shown.<sup>104</sup> The immobilized polymer layer around the particles was estimated to be about 2 nm thick. Wurm et al.<sup>47</sup> employed TMDSC (temperature modulated differential scanning calorimeter) and studied the retarded crystallization in Polyamide/Layered Silicates nanocomposites due to an immobilized interphase.

In this section, an extended investigation of Polypropylene/LDH nanocomposites is presented. A detailed thermal analysis is presented to support the previous conclusions drawn by employing various complementary characterization methods.<sup>133</sup> Here TMDSC is

employed to investigate the glass transition of the nanocomposites in detail and a detailed comparison is made with dielectric results. Each method will provide a different window to look at different aspects of the investigated process.

Heat capacity curves were obtained using a PerkinElmer PYRIS Diamond DSC. Initially samples were cooled to 223 K. Precise heat capacity at  $T_g$  was determined from the following StepScan differential scanning calorimetry (SSDSC) run, a special variant of temperature modulated DSC. Measurements were performed using samples of about 20 mg, 2 K steps at heating rate 6 K/min and isotherms of about 1.5 min.<sup>104,105</sup> This gives a frequency of the measurement 1/110s. The temperature range was from 223 K (below  $T_g$ ) to 523 K (above  $T_m$ ).

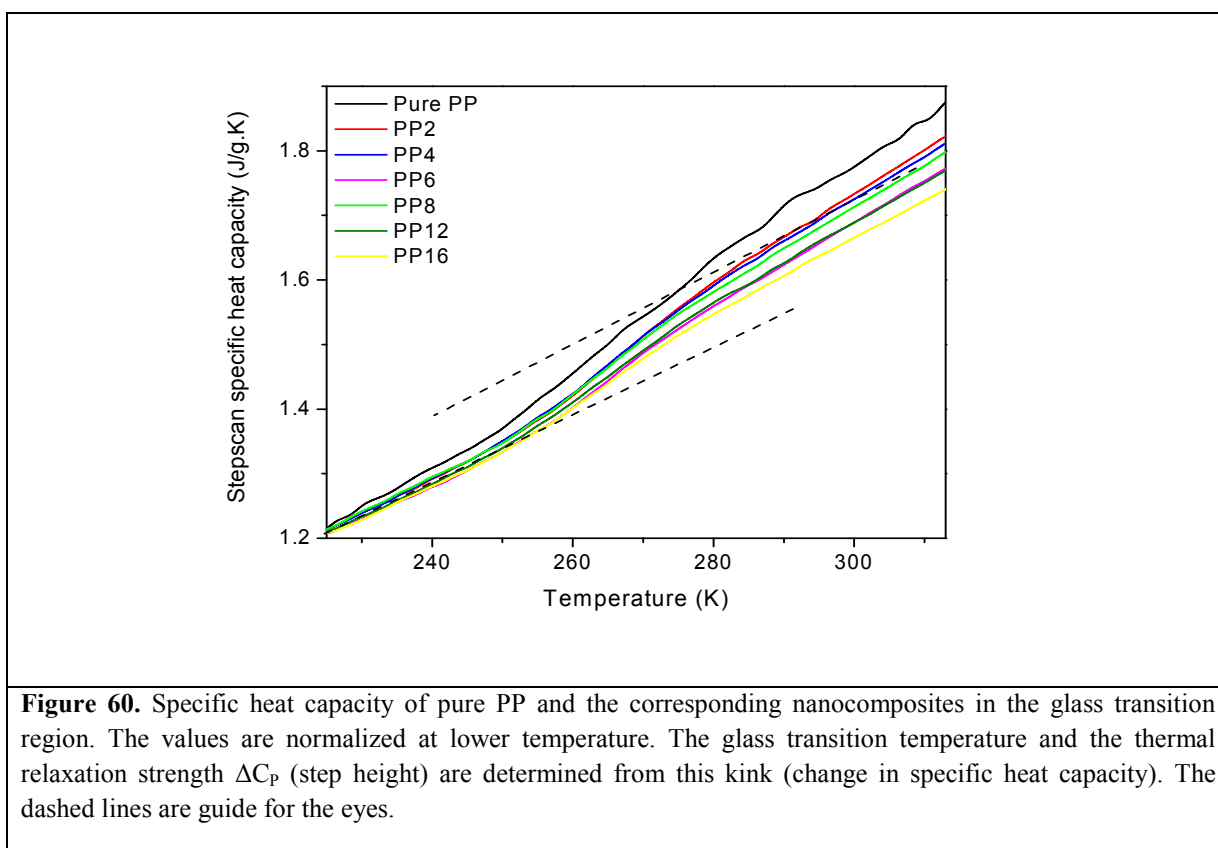
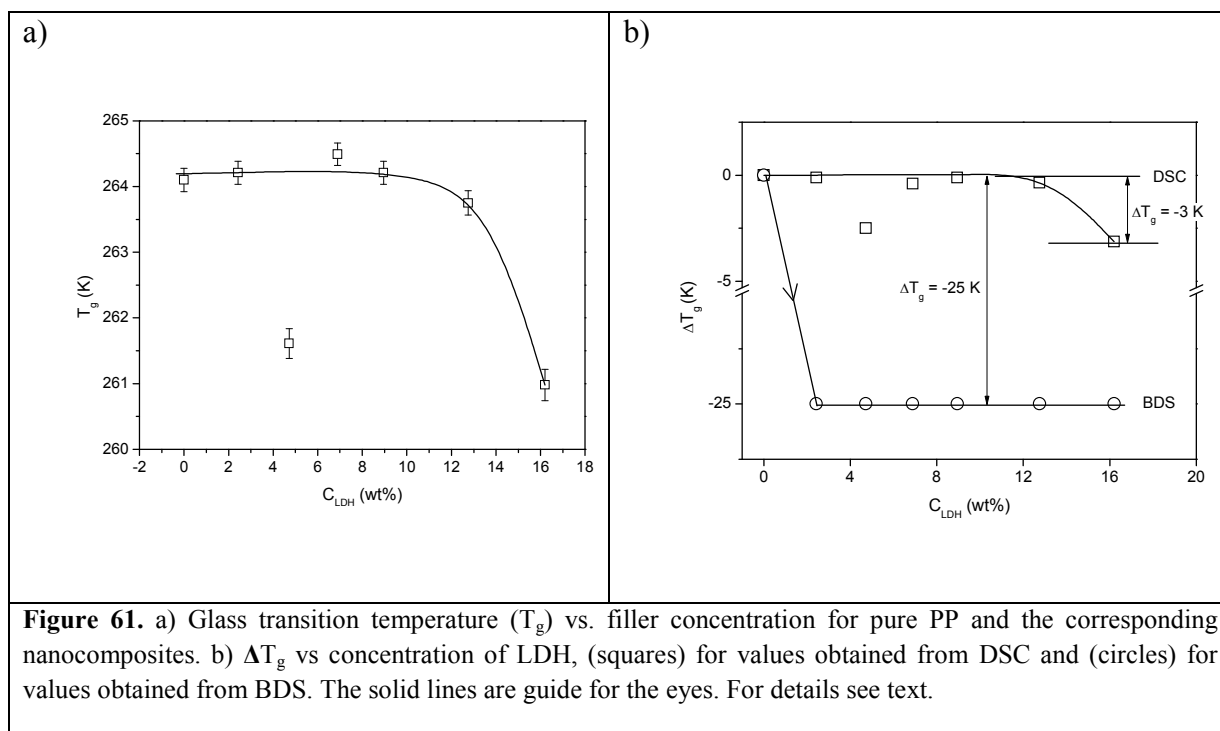


Figure 60 shows the specific heat capacity versus temperature for pure PP and the nanocomposites in the glass transition region. The  $T_g$  and the thermal relaxation strength are calculated by the procedure described in Chapter 4, section 4.2.2.1. The glass transition temperatures ( $T_g$ ) determined from the inflection are plotted against the filler concentration in Figure 61a.  $T_g$  is nearly constant up to PP12, which is also in agreement with the glassy dynamics observed in BDS results. A slight reduction in  $T_g$  is seen for PP16, which can be due to plasticization effect by higher concentration of LDH in the polymer matrix. For sake

of comparison, in Figure 61b,  $\Delta T_g$  ( $T_g^{\text{Nanocomposites}} - T_g^{\text{Pure}}$ ) values are plotted as a function of concentration of LDH and also compared with the  $\Delta T_g^{\text{BDS}}$ . From the dielectric results two relaxation processes were identified, one originating from molecules close to LDH (Process I) and the other from molecules farther from LDH sheets (Process II). Both processes followed glassy dynamics and for sake of comparison the  $T_g$  value from Process I is used in Figure 61b. For more details see Ref 133.



**Figure 61.** a) Glass transition temperature ( $T_g$ ) vs. filler concentration for pure PP and the corresponding nanocomposites. b)  $\Delta T_g$  vs. concentration of LDH, (squares) for values obtained from DSC and (circles) for values obtained from BDS. The solid lines are guide for the eyes. For details see text.

To discuss the glass transition phenomena in more detail, the step height ( $\Delta C_p$ ) is plotted as a function of the concentration of LDH in Figure 62.

$\Delta C_p$  can be calculated directly from the curves as described for the pure polymer above. Comparison of the  $\Delta C_p$  values for differently filled samples requires normalization to the polymer mass fraction.  $\Delta C_p$  reduces up to around 9% LDH and then it becomes nearly constant (Figure 62). This can be explained by the following consideration: The geometry and size of the LDH filler, there is a possibility that the molecules close to the LDH sheets are strongly adhered to the LDH. So it restricts the fluctuations of the molecules, resulting in decreased relaxation strength as more segments are immobilized in the vicinity of the LDH sheets. At higher concentration of LDH, the immobilization is saturated and so the thermal relaxation strength becomes nearly constant. This also agrees with the result obtained from BDS. Process I (molecular fluctuations close to LDH) occurs at higher temperatures and lower frequencies (higher relaxation time) as compared to Process II (molecular fluctuations

farther from LDH). This phenomenon of reduction in thermal relaxation strength is explained further below.

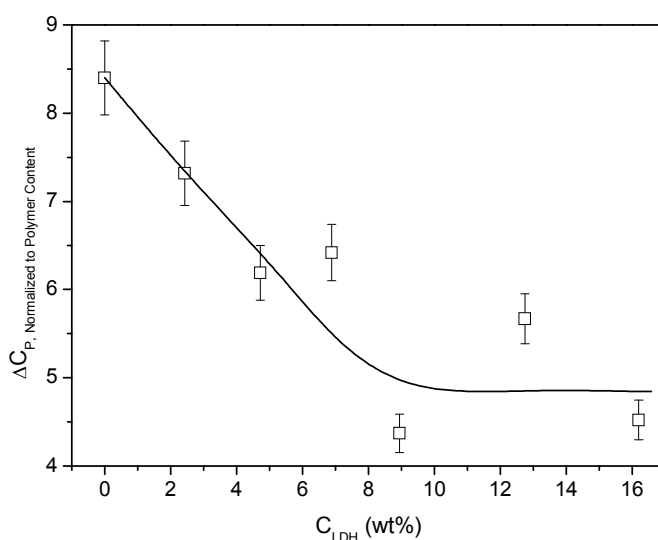


**Figure 62.** Thermal relaxation strength ( $\Delta C_p$ ) normalized to polymer mass fraction plotted as a function of the concentration of the LDH. The solid line is guide for the eyes.

It is a known fact that there exists a rigid amorphous fraction (RAF) in semi-crystalline polymers. Usually, the RAF exists at the interface of crystal and amorphous phase as a result of the immobilization of a polymer chain due to the crystal.<sup>134</sup> There is debate on whether the crystal melts first and then RAF devitrifies or the RAF devitrifies before the crystal melts. It cannot be answered easily because these two things often happen in the same temperature range. Also, the RAF fraction sometimes exists at the surface of the nano-filler in case of polymer based nanocomposites material.

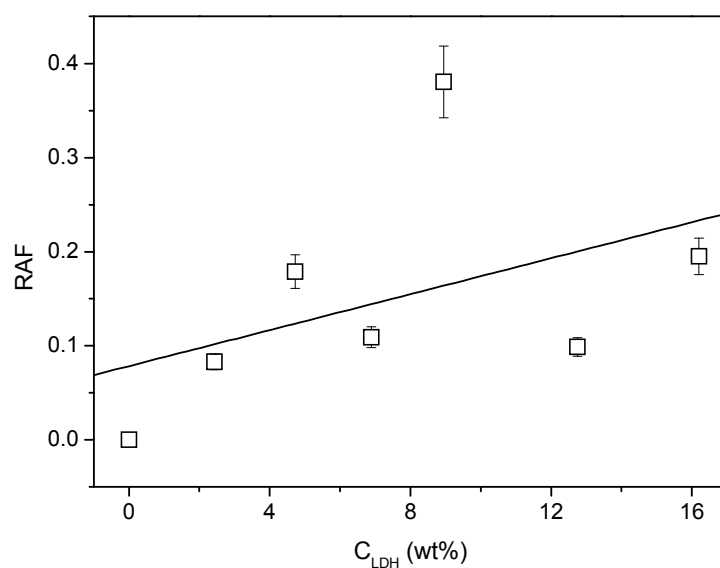


**Figure 63.** Rigid amorphous fraction (RAF) vs. content of LDH. The solid line is a linear regression to the data.

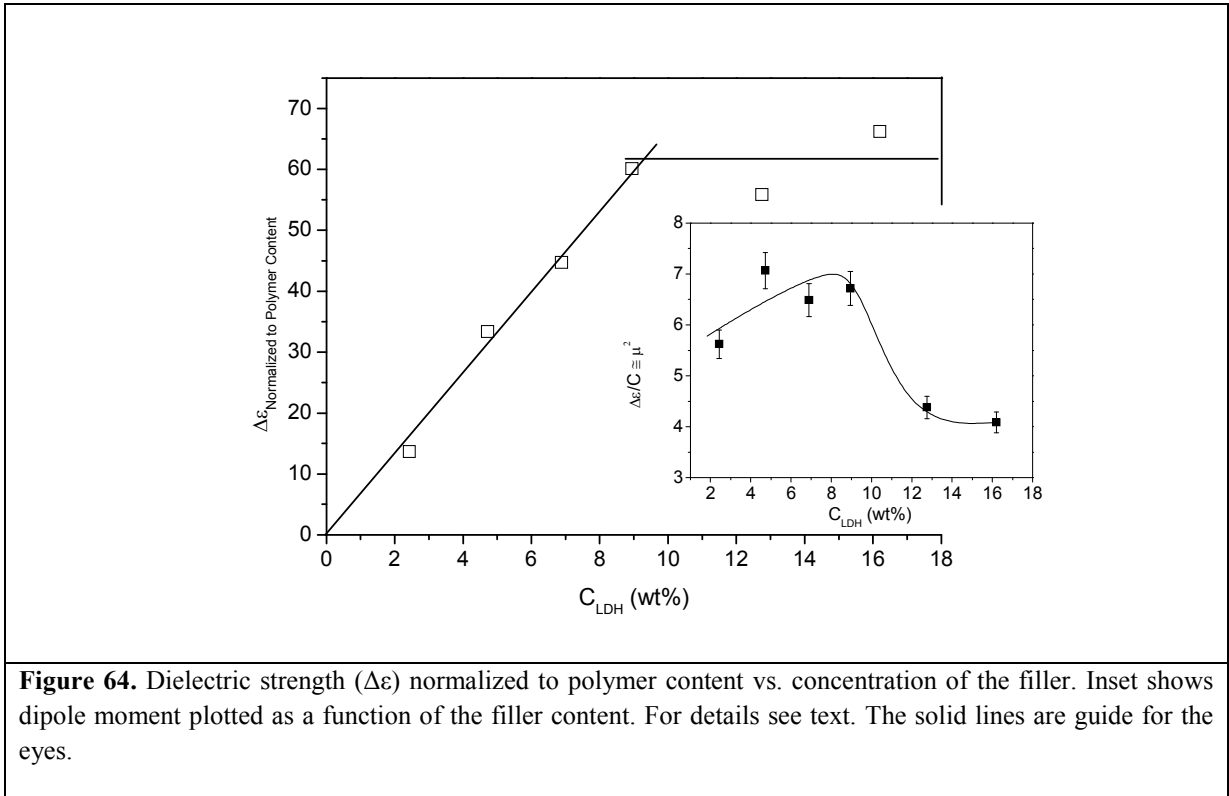
A formula has been well established for the determination of RAF in semicrystalline polymers based on accurate heat capacity measurement as described by Wunderlich, see Ref 134.

$$RAF = 1 - \text{filler content} - \Delta C_P / \Delta C_{P, \text{Pure}}$$

**(44)**

From Figure 63, the RAF which is calculated by using Eq. 44 increases as a function of concentration of LDH. This means that a larger amount of segments belonging to the amorphous part of the sample are immobilized with increasing content of LDH.

### Dielectric Strength ( $\Delta\epsilon$ )



As it was reported that the dielectric strength increases as a function of filler concentration, mainly due to the increase in the amount of the bulky polar molecule SDBS.<sup>133</sup> The content of SDBS is proportional to the LDH concentration. So the following can be derived from Eq. 17.

$\frac{\Delta\epsilon}{C} \approx \mu^2$	<b>(45)</b>
--	-------------

C can be related to N/V (from Eq. 17), as it is related to the amount of SDBS which in turn is proportional to the content of LDH.

As BDS probes the molecular fluctuations, which is completely different than DSC, an increase in dielectric strength and so the dipole moment is found up to PP8. For higher concentrations, the dielectric strength becomes nearly constant. There exists an immobilized phase at higher concentrations which is now also probed by BDS. So, the same material characteristic is explained using two different methods, viz. DSC and BDS.

Polyethylene is another class of material belonging to Polyolefins which finds applications commercially. Nanocomposites based on PE/ZnAl-LDH were also investigated with a similar approach as for PP/ZnAl-LDH described in the previous chapter.

### 6.1 Homogeneity and SAXS analysis of the nanocomposites

As mentioned in section 5.1, the most important point to be considered for establishing structure property relationships of nanocomposites is the homogeneous distribution of the nanofiller in the polymer matrix. Similar to PP/LDH, SAXS measurements at BESSY<sup>102</sup> was performed to investigate this question and presented exemplarily for PE16 in Figure 65 (solid curves, positions of measurements at the sample are shown in the inset). The finding of nearly collapsing scattering pattern is at the one hand side a strong indication for a homogeneous dispersion of O-LDH in the polymer matrix on macroscopic length scales ( $> 1$  mm). But on the other side due to the size of the nano objects (LDH stacks), the compound is inhomogeneous on microscopic length scales ( $< 1$  micro meter) and consists of a mixture of intercalated and exfoliated structures.

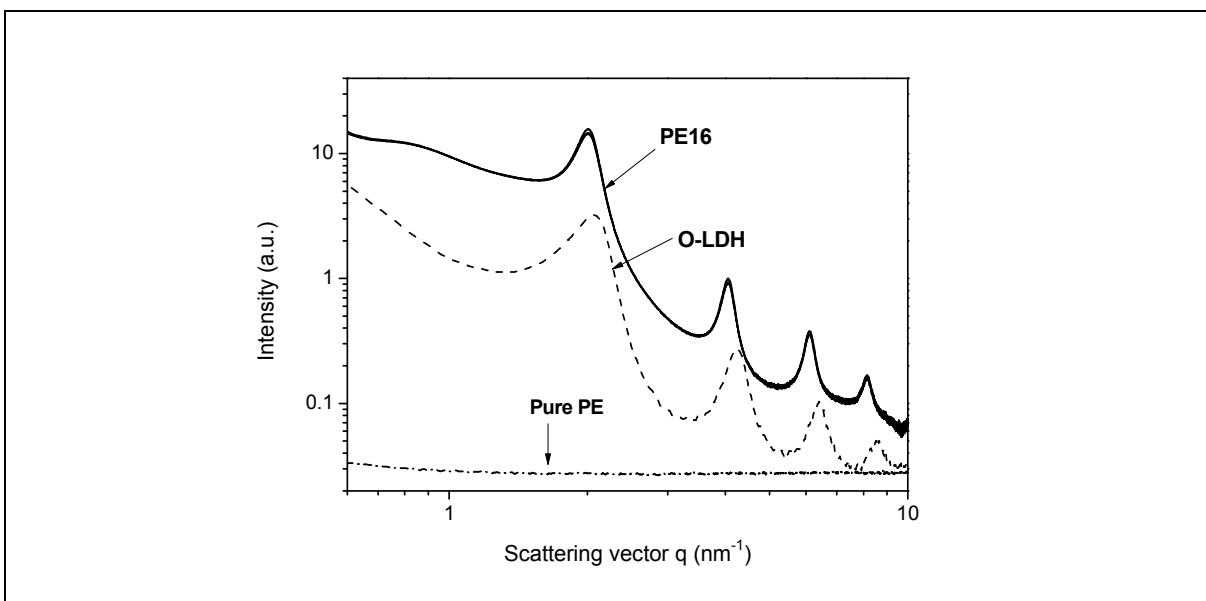


**Figure 65.** Overlay of five synchrotron SAXS curves from a disk sample of PE16 with a diameter of 30 mm (solid lines). The five positions for SAXS measurements using an X-ray beam size of 0.1 mm were randomly distributed on the disk-shaped sample. Sum of 4 Gaussians were fitted to the data (dotted line). SAXS curves of the O-LDH and the pristine PE (dashed and dash-dotted line, respectively).

An analysis of the SAXS data for nanocomposites was carried out in a similar way as for pure LDH. In this case, four equidistant located Gaussians were fitted with the first



maximum at  $2.01 \text{ nm}^{-1}$  (Figure 65, dashed curve). This position corresponds to a lamellar repeat unit of 3.12 nm and hints to a slight expansion of the layers in comparison to the O-LDH (2.94 nm). A similar expansion is reported for PP-ZnAl-LDH (Chapter 5) nanocomposites.<sup>133</sup> The reason is the intercalation of polymer chain segments into the interlayer region of LDH due to strong shear forces during extrusion (sample preparation). To determine the stack size of the LDH layers, the peak widths (Gaussian fits) were calculated to be  $0.56 \text{ nm}^{-1}$  to  $0.34 \text{ nm}^{-1}$ . Therefore,  $l_c$  is in the range of 11.2 nm to 18.5 nm, which is equivalent to 4 to 6 layers. This indicates an intercalated morphology of the nanocomposites. It can be also observed in TEM image in Figure 66. This is also in agreement with the sharp higher order reflections observed for the nanocomposite.

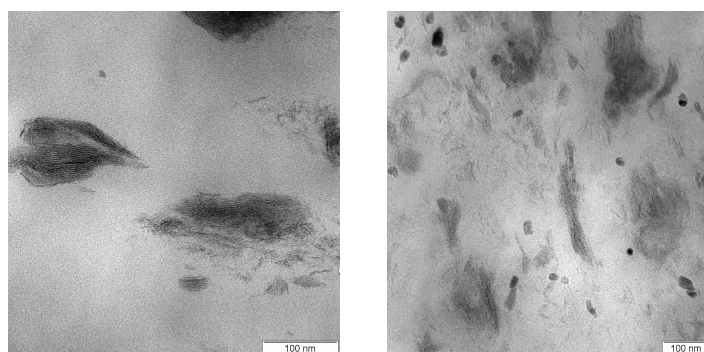
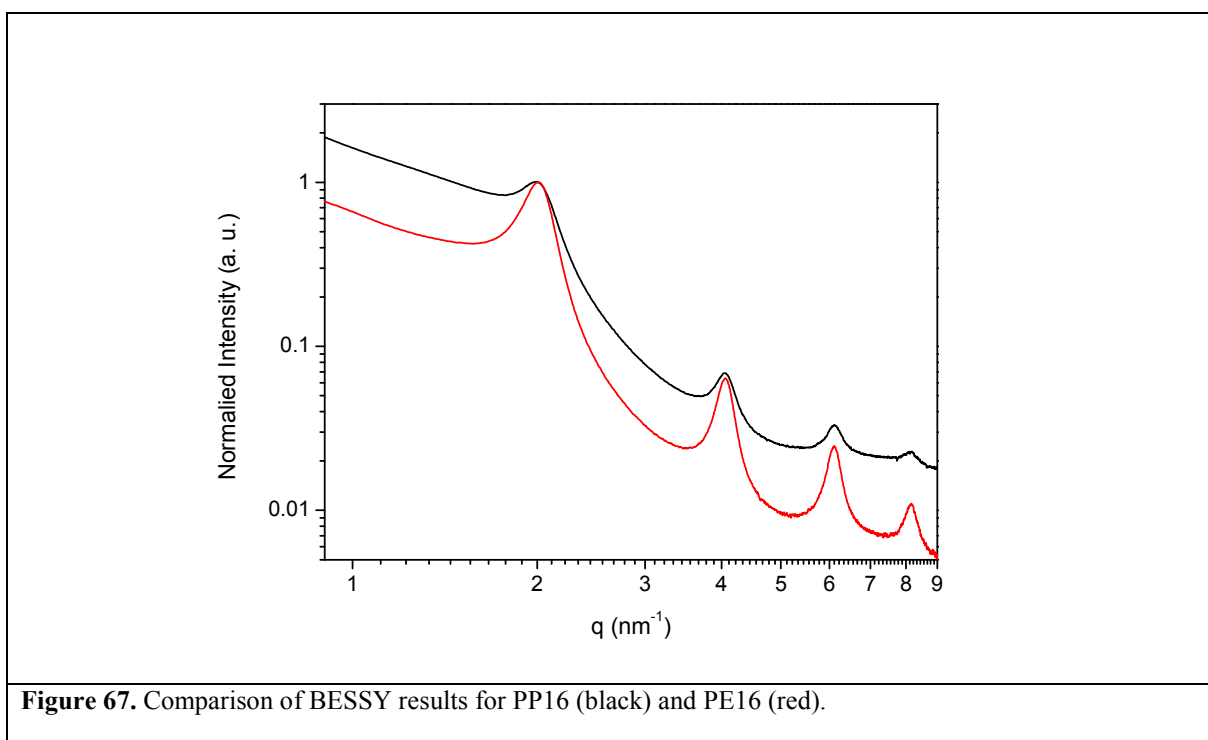


**Figure 66.** TEM (LEO 912) images for PE2 (left) and PE12 (right) at a resolution of 100nm, 120 kV acceleration voltage.

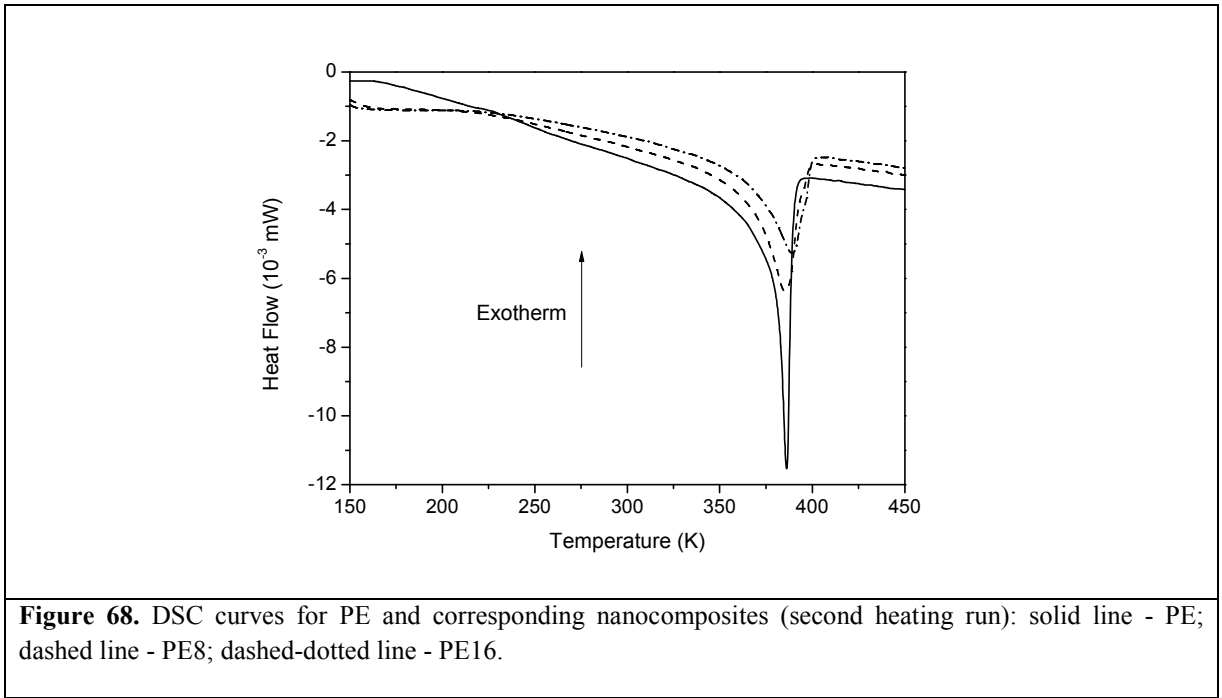
### ***Comparison of BESSY data for PP and PE nanocomposites***

Figure 67 gives a comparison for the BESSY data of PP16 and PE16. The peaks for PE16 are more pronounced than PP16. This hints that the relative degree of exfoliation is higher for PP16 as compared to PE16. The MFI for PP (8 g/10 min) is higher than PE (3.52 g/10 min) or in other words the melt viscosity for PP is lower than that of PE. This could probably be the reason that the LDH could easily diffuse through the melt during processing (melt extrusion). However, this depends also on the screw speed and the processing temperature, which in both the cases are same.



## **6.2 Investigation of degree of crystallinity using DSC and WAXS**

Figure 68 compares the DSC curves for the second heating run for PE, PE8 and PE16. A melting transition indicated by a peak at  $T_{\text{melt}} \sim 386$  K is observed.



In the inset Figure 69 of melting ( $\Delta H_{\text{melt}}$ ) and crystallization ( $\Delta H_{\text{crys}}$ ) enthalpies are plotted versus the concentration of LDH. The enthalpies are estimated by determining the areas below the crystalline and melting peaks (For the sake of comparison the absolute values of  $\Delta H_{\text{melt}}$  and  $\Delta H_{\text{crys}}$  are plotted in the inset of Figure 69). As the polymer fraction decreases with increasing LDH concentration, the enthalpy values have to be normalized to the content of the polymer.

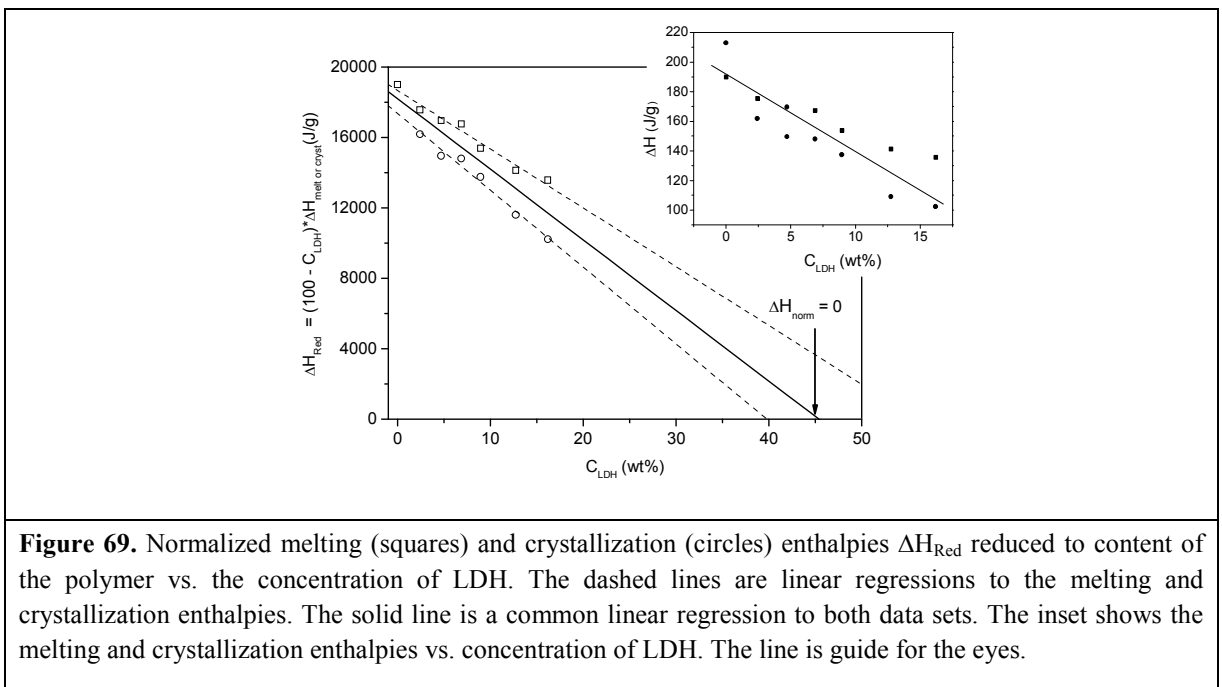


**Table 8.** Compilation of the investigated nanocomposite samples (thermal data). (Here first and second melting is from DSC measurement).

Sample Information		1. Melting (1. heating)		Crystallization (cooling)		2. Melting (2. heating)	
Code	LDH (wt%)	T <sub>m</sub> (K)	$\Delta H_{\text{melt}}$ (J/g)	T <sub>c</sub> (K)	$\Delta H_{\text{crys}}$ (J/g)	T <sub>m</sub> (K)	$\Delta H_{\text{melt}}$ (J/g)
PE	0	386	217	373	-190	386	213
PE2	2.43	383	156	371	-180	383	166
PE4	4.72	383	149	371	-178	382	157
PE6	6.89	382	161	372	-180	382	159
PE8	8.95	385	142	375	-169	3855	151
PE12	12.75	381	123	377	-162	389	133
PE16	16.20	392	122	378	-162	389	122

The normalized enthalpy values  $\Delta H_{\text{Red}}$  also decrease linearly with increasing concentration of LDH where a similar dependence is obtained for melting and crystallization. This indicates that the degree of crystallization decreases with increasing the content of LDH. The normalized enthalpy is extrapolated to zero value which results in a critical concentration of LDH of ca. 45 wt% a value much lower than 100 wt%. For higher concentrations than these critical ones, the crystallization of PE will be completely suppressed. A similar behavior was observed for nanocomposites based on polyethylene containing MgAl-LDH,<sup>22</sup> polypropylene containing ZnAl-LDH (Chapter 5). It should be noted that for other systems, an increase of crystallization rate and also more perfect crystals were observed for low concentrations of nanofiller. It was argued that the nanoparticles can act as additional nucleation sites.<sup>135,136</sup> So the observed behavior might depend in detail on the type of system studied. WAXS is in addition employed to estimate the degree of crystallinity for the nanocomposites. The observed dependence on the concentration of LDH estimated by WAXS is compared with the data obtained from the DSC experiments.

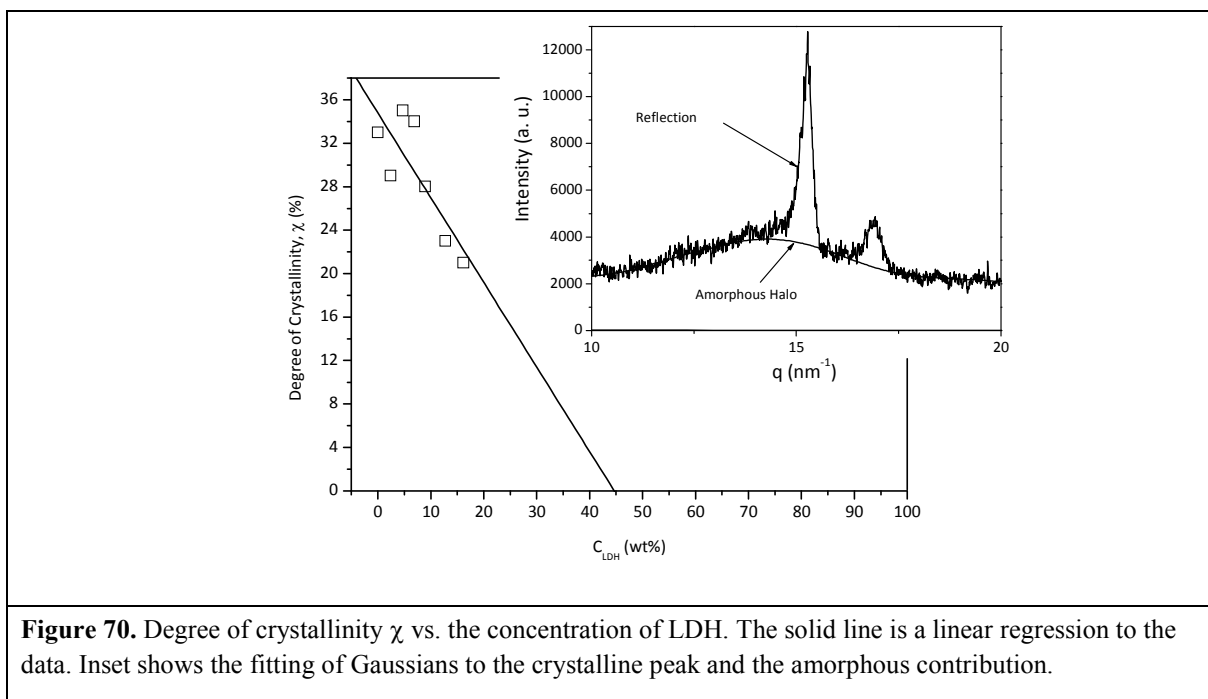
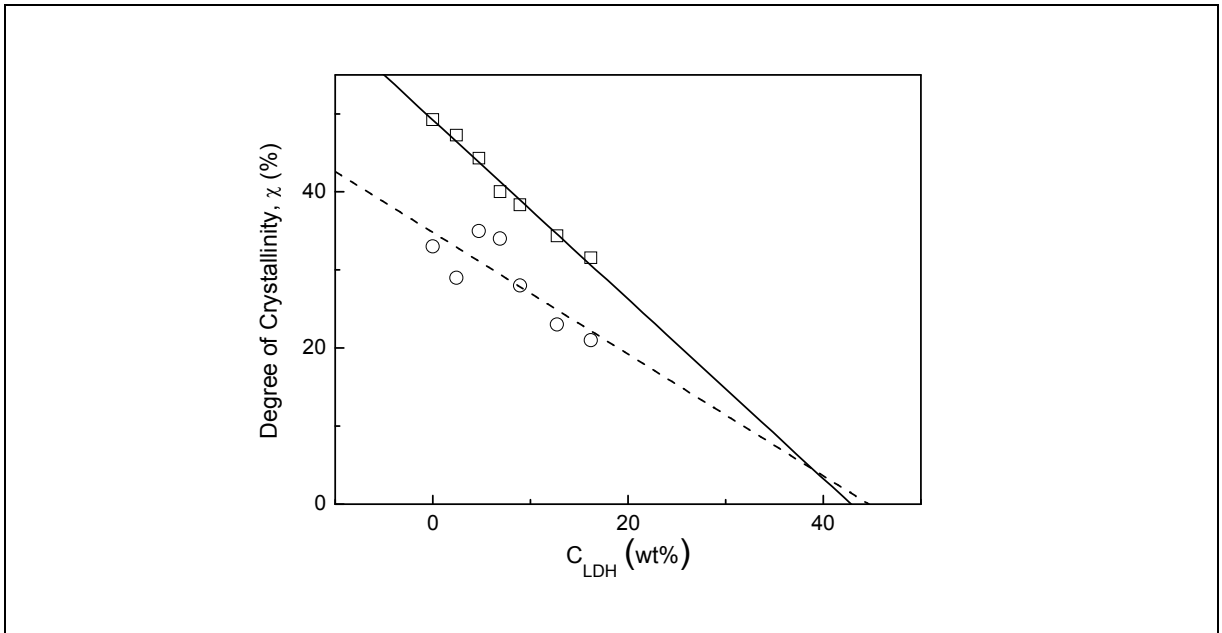


Figure 70 shows that  $\chi$  decreases with increasing concentration of LDH in agreement with the DSC results. The extrapolation of the  $\chi$  to zero gives a concentration of ca. 45 wt % of LDH where there are no crystallites presents in the polymer. This limiting value estimated from WAXS measurements is equal to the value obtained by DSC (45 wt %). This is a strong conclusion, due to the fact that both the techniques DSC and WAXS measure slightly different aspects of the same phenomenon. In case of DSC, the measured enthalpy changes are related to the crystalline structure whereas, for WAXS direct information of the molecular structure is obtained by X-ray diffraction. Even for WAXS absolute values can depend on the employed method of analysis.



**Figure 71.** Comparison of the degree of crystallinity changes as a function of the LDH content for PP/LDH (squares) and PE/LDH (circles) nanocomposites. The solid and dashed lines are linear regression to the data.

Figure 71 presents the comparison of the changes in the degree of crystallinity as a function of LDH content for PP/LDH and PE/LDH nanocomposites. The percentage crystallinity is lower in PE/LDH nanocomposites as compared to PP/LDH.

### 6.3 Dielectric relaxation spectroscopy (BDS)

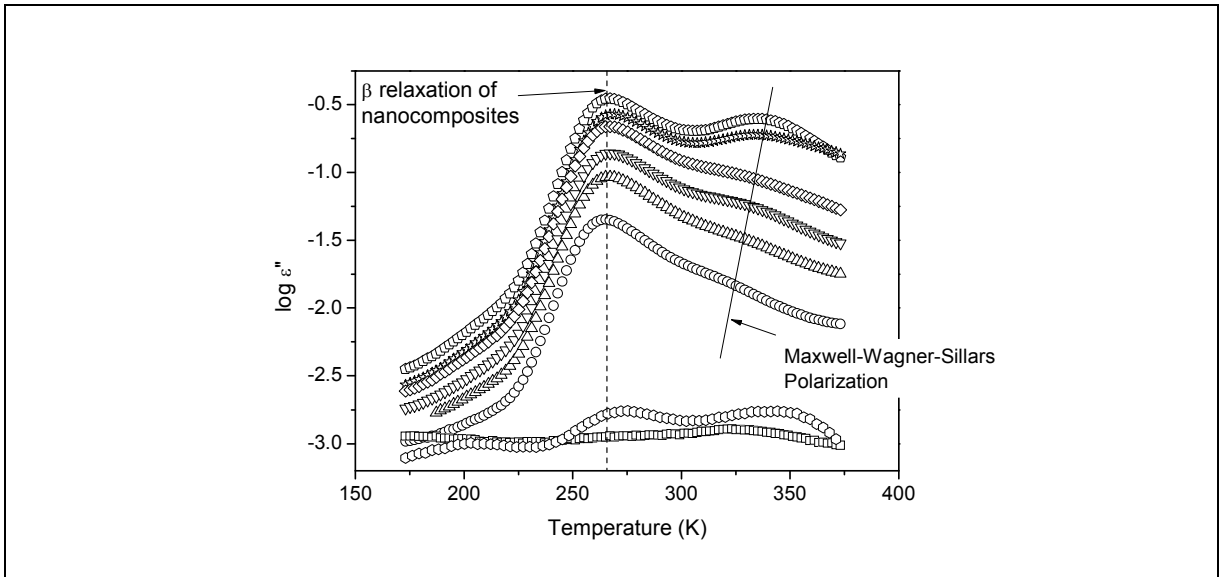


**Figure 72.** Dielectric loss  $\epsilon''$  versus temperature  $T$  at a frequency of 1 kHz for PE (squares), PE-g-MAH (hexagons) and different nanocomposites: PE2 (circles), PE4 (triangles), PE6 (inverted triangles), PE8 (rhombus), PE12 (stars) and PE16 (pentagons).

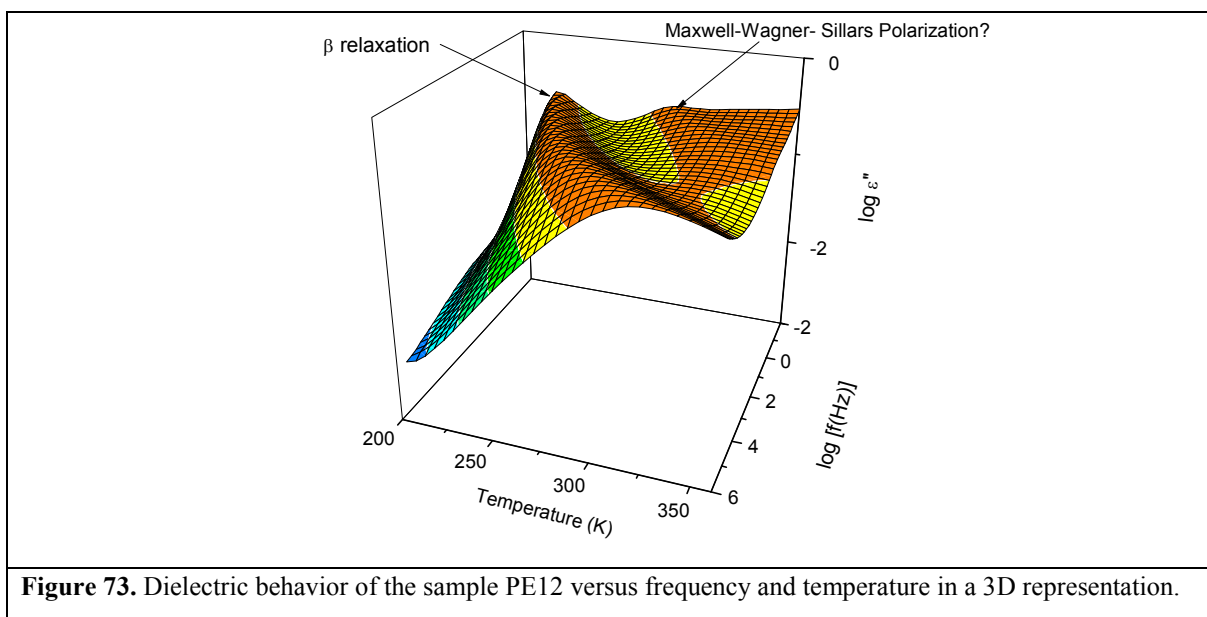
Figure 72 shows the dielectric behavior of the nanocomposites in the temperature domain at fixed frequency of 1 kHz in dependence on the concentration of LDH. The symmetry in the repeating unit of polyethylene leads to no intrinsic dipole moment. This results in a very weak dielectric response of pure PE due to impurities and defects. Therefore, besides other approaches the dielectric probe technique was used to study the molecular dynamics of polyolefins in detail.<sup>121</sup> The isochronal spectra of pure PE and PE-g-MAH (polyethylene grafted maleic anhydride) show several weak relaxation processes. A weak process is observed at high temperature which is termed as  $\alpha_c$  relaxation. It is related to molecular fluctuations in the crystalline lamella. Its molecular nature is still under discussion. Probably this process is due to a rotational-translation of chain segments assisted by a chain twisting.<sup>137-139</sup>

In case of the nanocomposites at temperature around 275 K amorphous process related to segmental fluctuations (cooperative glass transition) in the disordered regions of PE is observed. An additional process is observed at higher temperatures which is also present in case of pure PE and PE-g-MAH. Its intensity increases and its position shifts with increasing concentration. This might indicate that this process is related to the presence of the nanofiller. At the first glance this peak might be assigned to  $\alpha_c$  relaxation, however it becomes more pronounced with increasing concentration of LDH. But the degree of crystallinity reduces as a function of LDH (Figure 70), so this process cannot be related to  $\alpha_c$  relaxation. This also indicates that its origin is not from PE-g-MAH. One other possibility might be percolation of electric excitations similar to PP/LDH (Chapter 5), however this cannot be the case here, as this process is frequency dependent (Figure 73). Other possibility might be an interfacial polarization process (Maxwell-Wagner-Sillars polarization).<sup>140</sup> Generally, such a process is caused by (partial) blocking of charge carriers at internal surfaces or interfaces of different phases having different values of the dielectric permittivity and/or conductivity at a mesoscopic length scale (The blocking of charges at the electrodes is called electrode polarization). So for the nanocomposite one may speculate that the charge carriers are blocked by the nanoparticles causing a Maxwell-Wagner-Sillars polarization.

As compared to pure PE, a strong increase in the intensity of the  $\beta$ -relaxation with increasing concentration of LDH is observed which is similar to PP/LDH (Chapter 5). The increase in the measured dielectric loss with the concentration of LDH is due to an increase in the concentration of polar molecules (SDBS). Similar to PP/LDH, the SDBS molecules are predominantly located or adsorbed at the LDH layers. So BDS here probes the molecular

mobility of segments located in an interfacial area close to the LDH sheets because the dielectric loss of pure polyethylene is by orders of magnitude lower and so the matrix of the nanocomposite can be regarded as dielectrically invisible.

Figure 73 shows the dielectric spectra for the nanocomposite PE12 also in a 3D representation. At lower temperature/higher frequency the  $\beta$ -relaxation is observed like for pure PE. Its intensity is strongly increased compared to that of pure PE as discussed above. At higher temperature/lower frequency the MWS polarization is observed which is not a relaxation process. The MWS polarization is very weak and so it was difficult to analyze it.



### Dynamic glass transition

In the following first the  $\beta$ -relaxation process is analyzed in detail. As usual the model function of Haviriliak-Negami (HN) (Eq. 31) is used to analyze relaxation processes quantitatively.



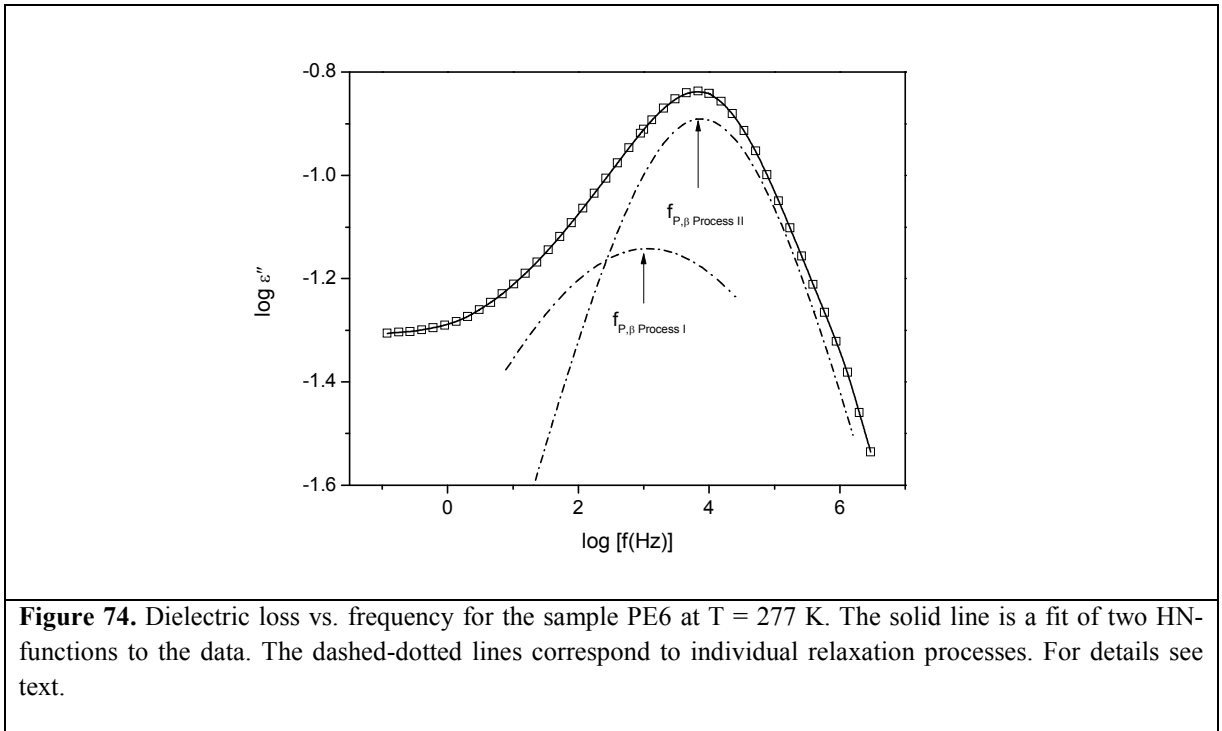
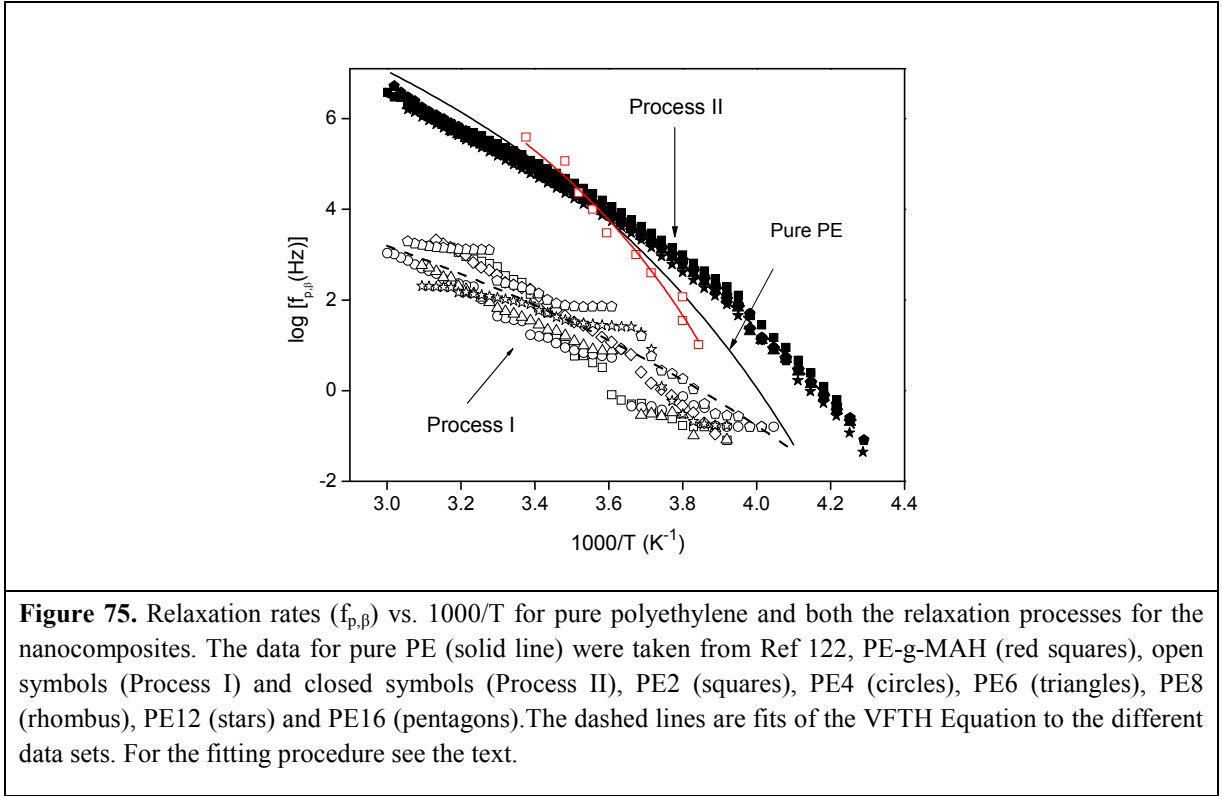


Figure 74 displays the dielectric loss of the nanocomposite PE6 versus frequency at T = 277 K. At higher frequencies a well defined loss peak can be observed (see also Figure 72). A more careful inspection of this peak shows that it has a pronounced low frequency contribution which originates from a further relaxation process. A fit of the data by only one HN-function results in a parameter set with unreasonable values. Therefore, the spectra were analyzed by fitting two HN-functions to the data (see Figure 74).

Process I appearing at lower frequencies and is assigned to the PE segments in close proximity of the LDH layers. Their mobility is hindered by the strong adsorption of the polar head group of the surfactants at the LDH layers. Process II at higher frequencies is related to the fluctuations of the PE segments at a distance farther from the LDH sheets. PE-g-MAH does not have any influence on the relaxation processes, as its dynamics is close to pure PE and the amount of maleic anhydride (MAH) (polar group) present in the nanocomposite is too low (around 1% by wt.) to affect the dynamics of the system. This can also be concluded by the increase in the intensity of the dielectric loss (log scale) for the nanocomposites as compared to that of PE-g-MAH (Figure 72).



The relaxation map for pure polyethylene<sup>122</sup> and the corresponding nanocomposites is given in Figure 75. For each data set of the  $\beta$ -relaxation, the temperature dependence of the relaxation rate is curved when plotted versus  $1/T$ . The data can be well described by the VFTH equation (Eq. 2),<sup>68-70</sup>

Figure 75 shows firstly that the data of the nanocomposites collapse on the same curve for all concentrations of the nanofiller for each process as also indicated by the raw spectra (see Figure 72). The estimated relaxation rates for process I show a higher scatter due to the ill-defined peak structure. Secondly, the temperature dependence of the relaxation rate for the  $\beta$ -relaxation of pure polyethylene is strongly different from that for the two processes observed for the nanocomposites showing a different curvature when plotted versus  $1/T$  and therefore different values for the Vogel temperature. Bearing in mind that selectively the molecular dynamics in the interfacial area between the nanoparticle and the polymer matrix is monitored this indicates that a different glassy dynamics takes place at the interfacial layer of the polymer and the LDH in comparison to pure polyethylene. In order to discuss more about the temperature dependencies of the relaxation rates of both the processes, the VFT equation is fitted to the data and a value of 12 was fixed for the pre-exponential factor to reduce the number of free fit parameter. Moreover, the derivative technique<sup>78-81</sup> is applied

and compared with the VFT fit parameters. This is discussed in more detail in the following section.

As discussed above for the nanocomposites the relaxation rates do not depend on the concentration of the nanofiller. Therefore, for the fitting of the VFT equation the data for all concentration were used in a common analysis. This procedure results in average values for  $A_0$  and  $T_0$  with a high statistical significance. The obtained VFT parameters for processes I and II observed for the nanocomposites are shown in Table 9, whereas for pure PE the parameters were obtained from Ref 122.

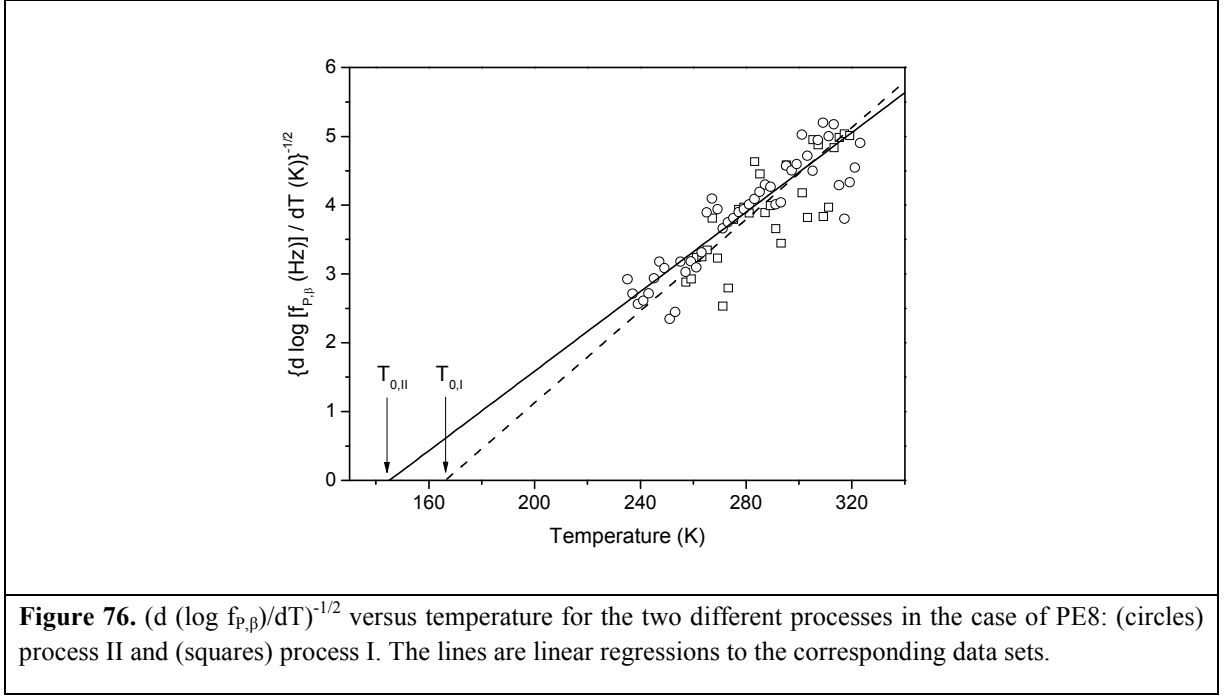
**Table 9.** Estimated VFT parameters for Pure PE and processes I and II with fixed  $\log [f_\infty (\text{Hz})] = 12$ .  $D$  is the fragility parameter and  $T_g^{\text{diel}}$  is the dielectric glass transition temperature (see text).

	$\log [f_\infty(\text{Hz})]$	$A_0$ (K)	$T_0$ (K)	$T_g^{\text{diel}}$ (K)	$D$
<b>PE</b>	12	914	182	250	11.5
<b>Process I</b>	12	851	$160 \pm 5$	260	12.2
<b>Process II</b>	12	955	$147 \pm 2$	240	14.9

There is a large difference in the estimated values of the VFT parameters of bulk polyethylene and that of the nanocomposites. For pure PE the molecular mobility across the whole matrix is measured whereas for the nanocomposites the interfacial region between the LDH layers and the polyethylene matrix is selectively monitored. From the VFT parameters a dielectric glass transition temperature can be calculated for instance by  $T_g^{\text{diel}} = T (f_p = 10 \text{ Hz})$  (see Table 9). The dielectric glass transition temperature for polyethylene located in the interfacial area is by more than 20 K lower than that of the bulk. This decrease in  $T_g^{\text{diel}}$  is accompanied by a stronger behavior of the whole relaxation processes compared to pure PE. These differences point to a difference in the physical structure of polyethylene in the bulk and polyethylene located in the interfacial area.

A more careful inspection of the estimated parameters for relaxation process I and II reveal that there is also a difference between these two modes. The Vogel temperature of process I is 15 K higher than that of process II and the fragility of process II is higher than process I. So this indicates different glassy dynamics for both the processes. A temperature dependence of the relaxation rates according to the VFT equation is regarded as a sign of glassy dynamics. Therefore, it is concluded that both of the observed relaxation processes are due to a dynamic glass transition in spatial regions with different distance to the LDH layers. The

thickness or the extension of the interfacial region (process I) and the region farther from the LDH (process II) is about the length scale 1 - 3 nm.<sup>77</sup>



For a more detailed analysis of the temperature dependence of the relaxation rates a derivative method is applied.<sup>141</sup> This method is sensitive to the functional form of  $f_p(T)$ , irrespective of the prefactor. For a dependency according to the VFTH equation one get,

$\left[ \frac{d(\log f_p)}{dT} \right]^{-1/2} = A^{-1/2} (T - T_0)$	<b>(46)</b>
---	-------------

This theoretical equation is used for the present experimental values in a plot of  $[d(\log f_p)/dT]^{-1/2}$  versus  $T$ , the VFT behaviour shows a straight line (see Figure 76). All the experimental can be well described by straight lines which again prove that the temperature dependence of the relaxation rates of both the processes is VFT like. This supports the conclusion that both the processes show glassy dynamics. The Vogel temperature  $T_0$  can be estimated by extrapolating the straight line to zero. So the estimated  $T_0$  are 166 K (Process I) and 145 K (Process II). These values are approximately equal to the values obtained by VFT fitting (see Table 9). The other VFTH parameters  $\log f_\infty$  and  $A$  are obtained by fitting VFTH equation to corresponding  $f_p$  data while keeping  $T_0$  fixed and is displayed in Table 10.

**Table 10.** Estimated VFT parameters for processes I and II using derivative technique. Average values are displayed here. The values for pure PE are obtained from the literature.<sup>122</sup>  $D$  is the fragility parameter and  $T_g^{\text{diel}}$  is the dielectric glass transition temperature (see text).

	$\log [f_\infty(\text{Hz})]$	$A_0$ (K)	$T_0$ (K)	$D$
<b>PE</b>	12.7	851.2	182	10.77
<b>Process I</b>	7.6	693.3	$166 \pm 5$	9.62
<b>Process II</b>	12.2	927.6	$145 \pm 2$	14.73

The difference in the estimated Vogel temperature is around 20 K for both the processes. This analysis indicates that the temperature dependence of the relaxation rates of both the processes is quite different characterized by different slopes of both the regression lines. This further supports the conclusion that the molecular dynamics in the interfacial area around the LDH sheets is quite different.

From Figure 75, it is known that the temperature dependence of both the processes is independent of the concentration. So this indicates that with increasing content of LDH, the relaxation mechanism does not change, only the amount of interfacial region increases. Simultaneously, the derivative technique can also be used considering all the concentrations of LDH.

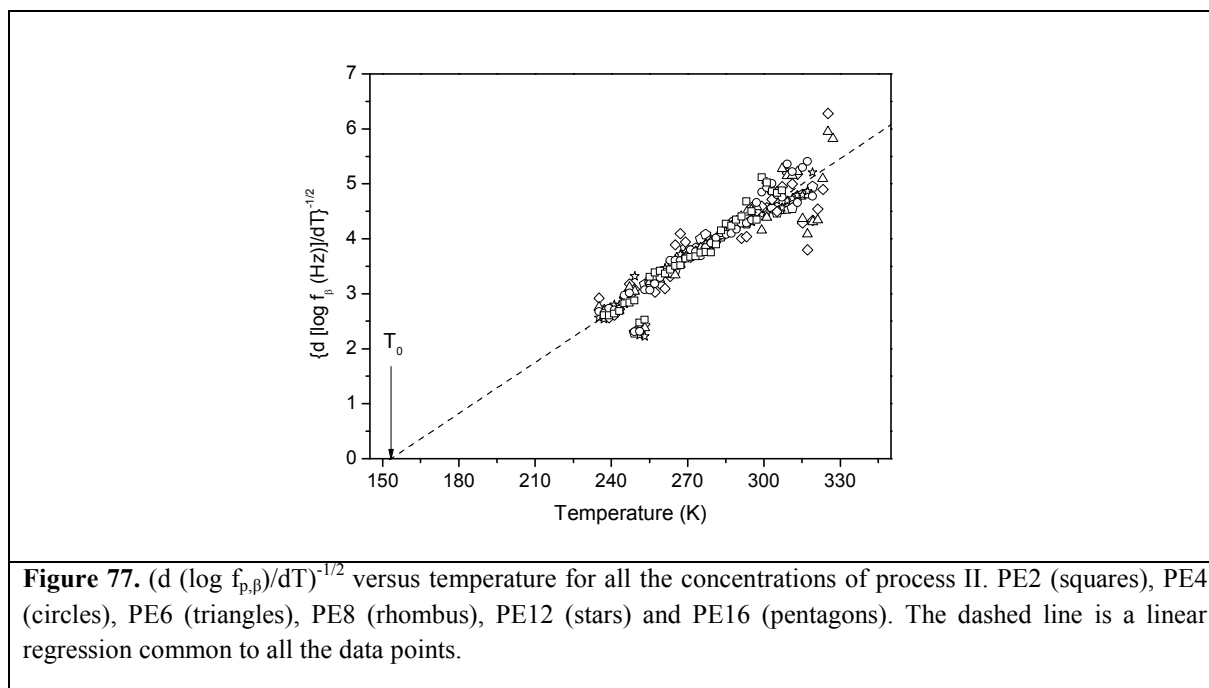
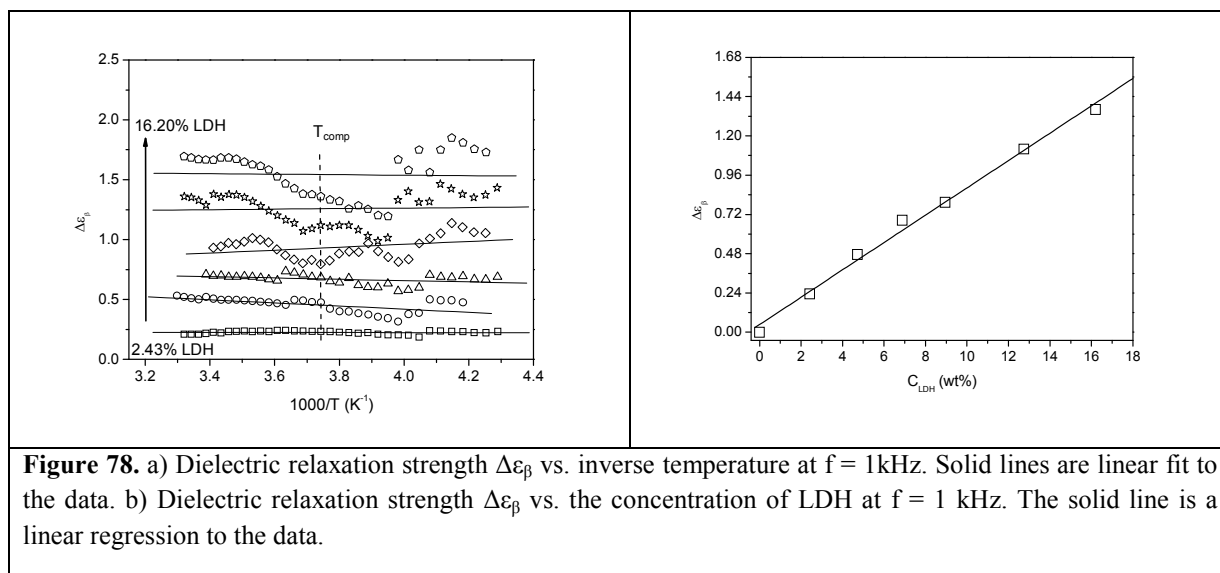


Figure 77 shows the derivative technique applied to all the concentrations of LDH (Process

II). They all collapse in a single line. The average Vogel temperature is estimated by extrapolating the straight line to zero. This procedure increases the statistical relevance of the estimated mean values of  $T_0$ . Using the errors of the slope and the intersection resulting from joint linear regression a maximal error is calculated for  $T_0$ . The maximal error is essentially smaller than the difference in the estimated Vogel temperatures.

For the dielectric strength the Debye theory generalized by Kirkwood and Fröhlich holds as presented in Eq. 17. The estimated dielectric strength for individual processes of the dynamic glass transition shows a large scatter (Figure 78a). So the sum of both the dielectric strengths,  $\Delta\epsilon_\beta = \Delta\epsilon_I + \Delta\epsilon_{II}$  is obtained by fitting two HN functions.



The dielectric strength of the  $\beta$ -relaxation  $\Delta\epsilon_\beta$  is estimated from HN function.  $\Delta\epsilon_\beta$  is plotted versus the concentration of LDH in Figure 78b. The  $\Delta\epsilon_\beta$  varies linearly with  $C_{LDH}$  as expected. This linear dependence proves the increasing number of SDBS molecules.

As no glass transition phenomena can be detected as reported in Ref 142, no RAF discussions can be presented for PE/LDH nanocomposites.

Commercialization of PLA because it is a bio-degradable polymer has been done in past few years. Improving its flame retardancy by incorporating LDH so that it finds more household applications is a research interest around the globe. This chapter explores the morphological findings of PLA-LDH and PLA-MWCNT nanocomposites.

### 7.1 MgAl-LDH based Polylactide Nanocomposites

The characterization of MgAl-LDH by SAXS and PLA by BDS is already described in Chapter 4. The analysis of the nanocomposites by the different characterization techniques is explained in this section.

#### 7.1.1 Homogeneity of the nanocomposites

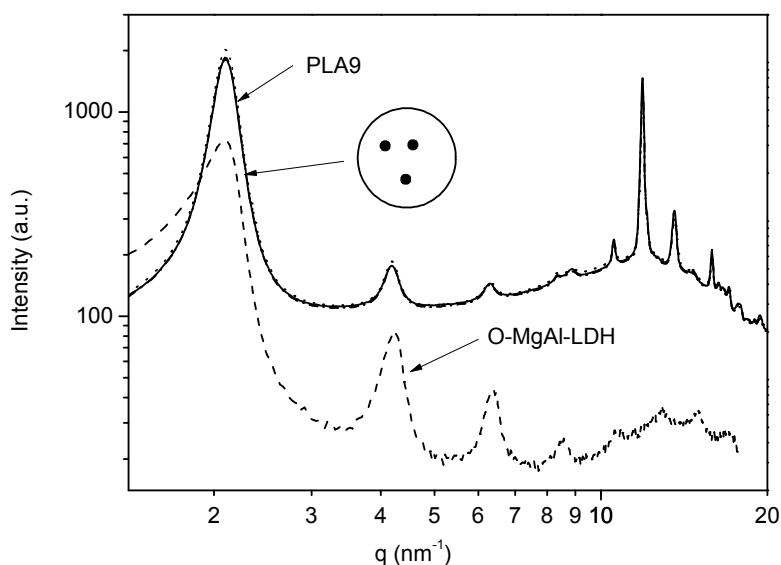


**Figure 79.** Overlay of three synchrotron SAXS curves from a disc sample of PLA9 with a diameter of 30 mm (solid, dotted and dashed-dotted lines). The dashed line shows the curve for organically modified LDH. A sum of Gaussians were fitted to the data.

As explained in the previous two chapters (sections 5.1 and 6.1), homogeneity of the nanocomposites on a macro scale is the first thing that needs to be analyzed. In this case too, it is done employing SAXS with a microfocus using synchrotron radiation at the  $\mu$ SpotBeamline of BESSYII.<sup>102</sup> In this case, it was measured at three different positions of the samples having a diameter of more than 30 mm where the spot diameter of the X-ray

beam was 0.1 mm. All the individual SAXS pattern nearly collapse into one chart as shown exemplarily for PLA9 in Figure 79 (solid, dotted and dashed-dotted curves, positions of measurements at the sample are shown in the inset). This again proves a homogeneous dispersion of O-LDH in the polymer matrix on macroscopic length scales ( $> 1$  mm). Similar to SAXS analysis for pure LDH and other nanocomposites, it was carried out for PLA-LDH too. After fitting Gaussians, the lamellar repeat unit  $d$  was found out to be 3 nm hinting to a slight expansion due to the intercalation of the polymer segments. This result is the same as the previously studied nanocomposites.<sup>128,133</sup> The stack size was determined from the widths of the peaks and the  $l_c$  was calculated to be 25.63 nm which is equivalent to around 6 – 7 layers.

### 7.1.2 Investigations by DSC and WAXS

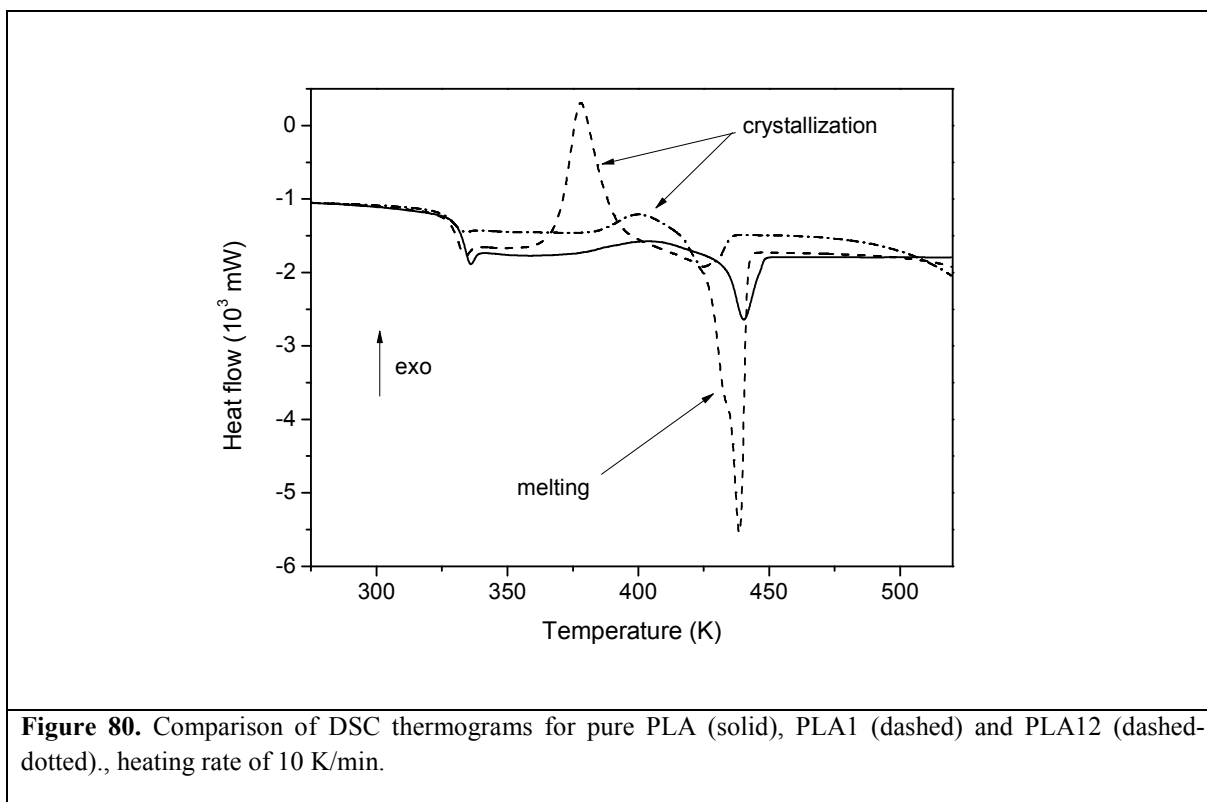
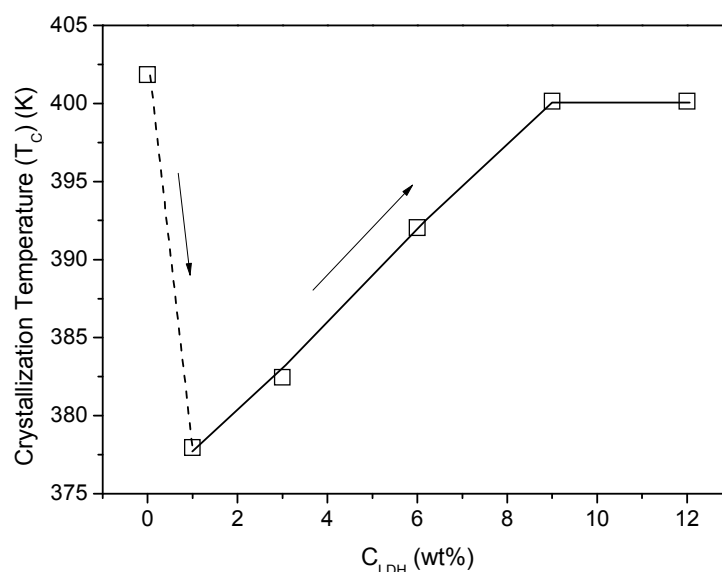


Figure 80 compares the DSC curves for second heating run for pure PLA, PLA1 and PLA12. A glass transition, crystallization and melting are observed. An interesting fact is observed in this case as compared to LDH based nanocomposites of the polyolefins (PP and PE). Comparison of thermograms of the nanocomposites to pure PLA shows a different crystallization and melting behavior. For PLA1, there is a sudden increase in the crystallization and melting enthalpies. Moreover, the crystallization temperature decreases



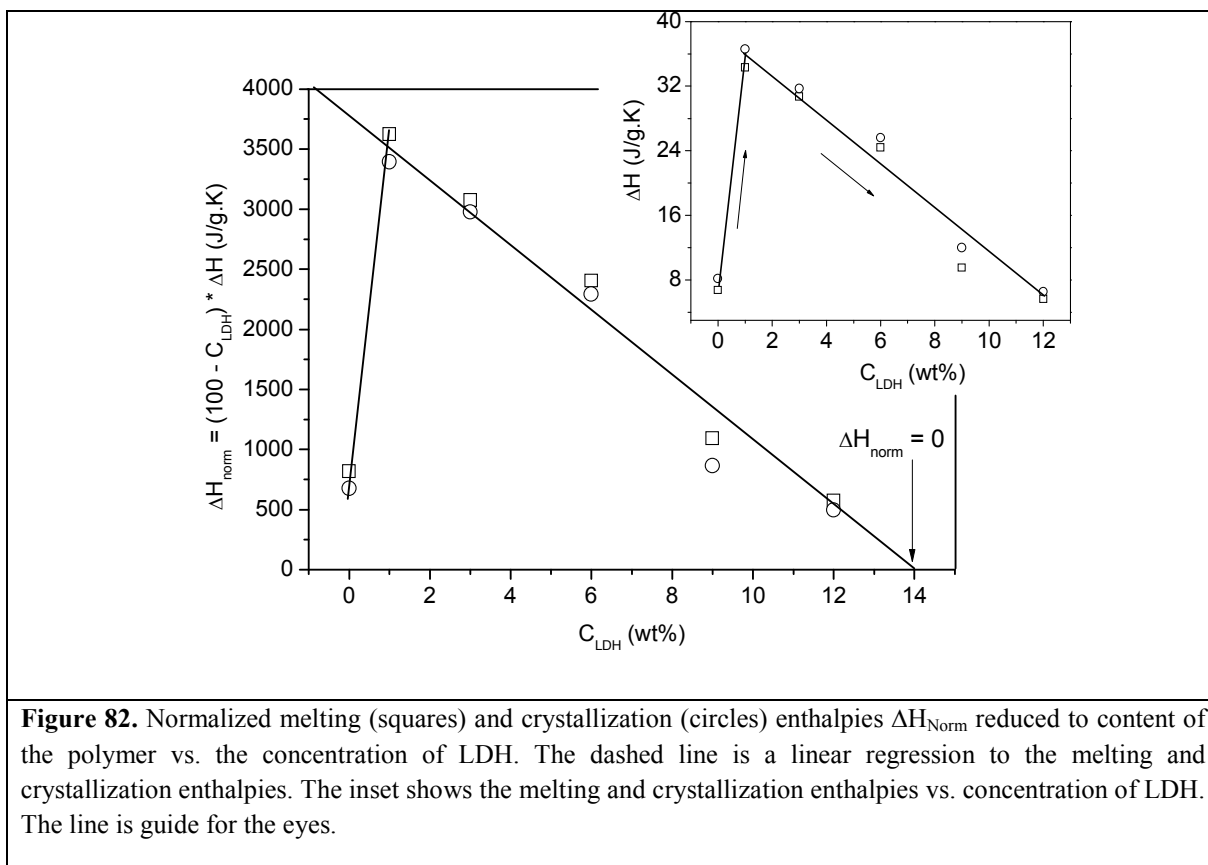
drastically for PLA1 as compared to the pure polymer. For PLA12, the thermogram looks nearly same as pure PLA only with a slight decrease in the melting temperature.



**Figure 81.** Crystallization temperature ( $T_c$ ) vs. the concentration of LDH.

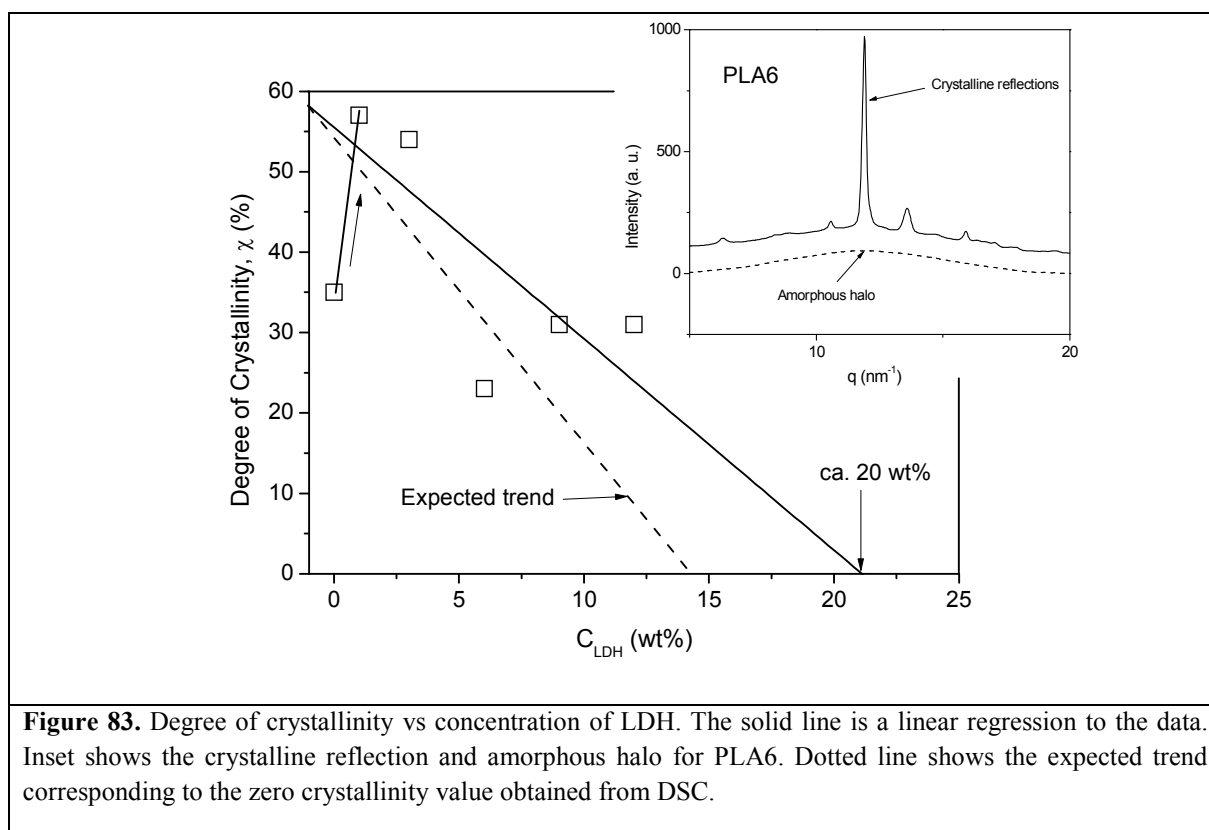
Figure 81 shows the dependence of the crystallization temperature on the concentration of LDH in the nanocomposites. It is interesting to observe that the crystallization temperature decreases drastically for PLA1 and then again increase till it becomes nearly a plateau at around PLA9. This result compared with Figure 80 indicates that at low concentrations, LDH acts as a nucleating agent which promotes crystallization. It was shown, by Tsuji et al. that morphology of PLA (L type, which is used in the present case) strongly depends on the processing conditions and the annealing temperatures.<sup>143</sup> Pilla et al. showed that on addition of recycled wood fiber, the crystallinity of PLA increased.<sup>144</sup> In the present case, melt mixing (melting) and compression pressing sheets (annealing) supports the crystallization behavior. After PLA1, the crystallization temperature increases which could mean that the increase in the amount of LDH content now sterically hinders the crystallization. This is explained in detail in the next section. However, in order to fully understand the crystallization behavior, a detailed analysis employing calorimetric techniques needs to be done.

Figure 82 presents the dependence of the crystallization and melting enthalpies as a function of the LDH content.



In the inset of Figure 82, melting ( $\Delta H_{\text{melt}}$ ) and crystallization ( $\Delta H_{\text{crys}}$ ) enthalpies are plotted versus the concentration of LDH. (For sake of comparison the values of  $\Delta H_{\text{melt}}$  and  $\Delta H_{\text{crys}}$  are plotted.) Both the quantities decrease with increasing concentration of LDH because the amount of polymer decreases with increasing content of LDH. Also this normalized enthalpy values  $\Delta H_{\text{Norm}}$  first increase for PLA1 and then decreases linearly with increasing concentration of LDH where a similar dependence is obtained for melting and crystallization. Taking the enthalpy values as a measure for the degree of crystallization this indicates that it first increases for PLA1 and then decreases with increasing the content of LDH. This observation can be compared with the discussion above related to the crystallization temperature. The extrapolation of normalized enthalpy to zero value results in a critical concentration of LDH of ca. 14-wt%. For concentrations above this value, the crystallization of PLA will be completely suppressed. This might be the reason that the crystallization temperature reaches a plateau at for PLA9 and PLA12, as the higher amount of LDH completely suppresses the crystallinity, and so after ca. 14-wt% no crystallinity will be observed.

WAXS was also employed to determine the degree of crystallinity ( $\chi$ ). As shown in the inset of Figure 83, the amorphous halo was subtracted by using software named EVA V1.2 (Bruker-AXS, Karlsruhe, Germany). The database of this software has non-crystalline spectra of various materials which are then used for a particular material to subtract the amorphous halo.



From WAXS measurements too, it is estimated that the crystallinity for PLA1 is higher than pure PLA. After the subtraction of background, Gaussians were fitted in order to determine the area below the crystalline reflection and amorphous halo. The degree of crystallinity is then determined using the Eq. 37, like for PP and PE and plotted against the concentration of LDH. The extrapolation of the trend to zero crystallinity shows that ca. 20 wt% of LDH, the crystallinity of PLA can be completely suppressed. This value is little higher than determined by DSC (14 wt%). Such a difference can be accounted to the scatter in the WAXS data as can be seen in Figure 83.

## Additional Thermal Investigations

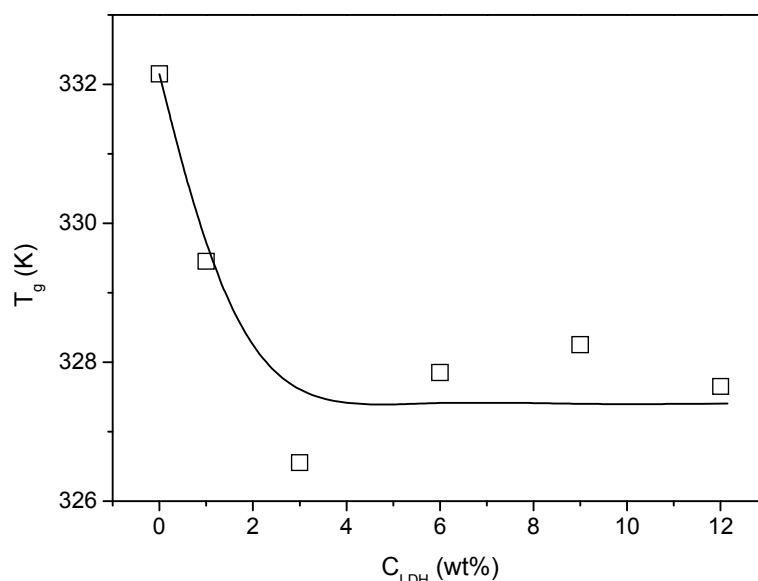
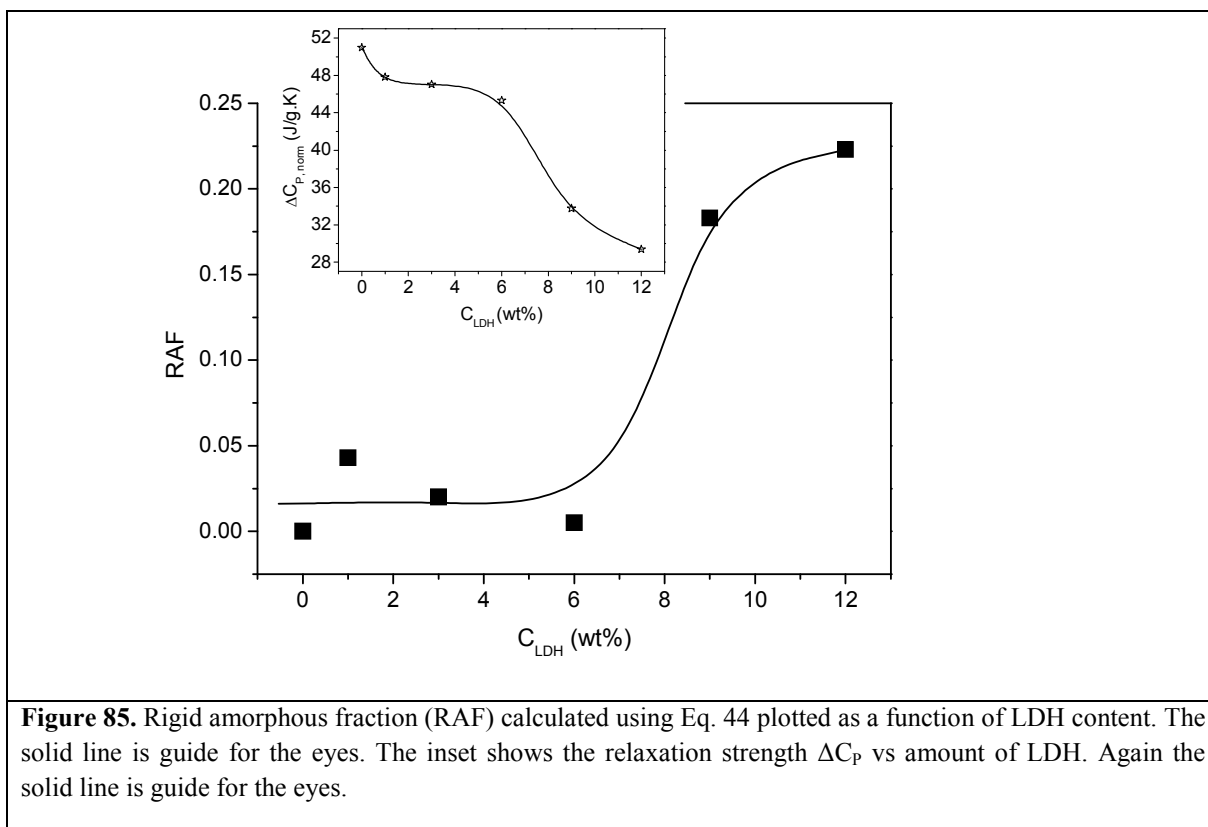


**Figure 84.** Thermal glass transition temperature dependence as a function of LDH content.

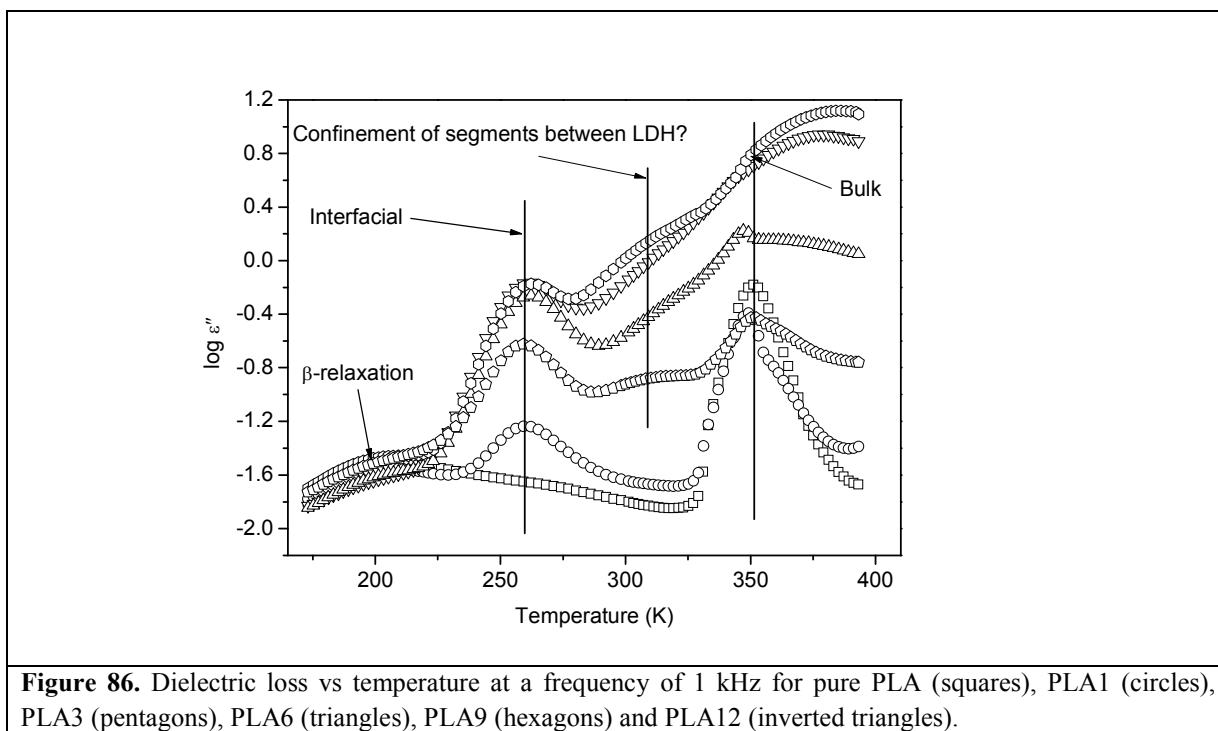
Figure 84 shows the dependence of the thermal glass transition temperature on the content of LDH. The glass transition temperature at first decreases and then becomes nearly constant. The reduction in the  $T_g$  values for PLA1 and PLA3 as compared to PLA can be assigned to an increase in the free volume of the matrix. This is possible if some amount of SDBS molecules are dispersed in the matrix. At higher concentrations, the amount of LDH increases which fills up the free volume making the  $T_g$  values nearly constant. PLA contains a C=O bond in the backbone, so unlike PP and PE based nanocomposites, this bond can interact with the LDH sheets directly (not through SDBS). Due to this steric hindrance is created and possibly the SDBS molecules are dispersed in the bulk matrix.



From Figure 85, the RAF calculated from Eq. 44 is nearly constant up to PLA6 which then increases drastically for PLA9 and further for PLA12. With increasing amount of LDH, the polymer segments in the amorphous phase are more restricted at the interface of the LDH sheets. This also confirms the observed changes in the glass transition temperatures. The present case is different from the findings for PP/LDH. In case of PLA, there exists a C=O bond in the main chain. This is a preferential site for the LDH to interact with the polymer, which in case of the non polar PP is not possible. For PP/LDH the interaction with LDH was via. SDBS and mostly not through polymer segments directly. So that might be the reason for a very gradual increase in the RAF (see Figure 63) as compared to a drastic change in case of PLA/LDH. As discussed above the relaxation strength  $\Delta C_p$  is related to the amount of amorphous phase. This observation displayed in the inset of Figure 85 additionally proves the point of RAF. Even in case of the relaxation strength it is nearly constant upto PLA6 and it then drastically reduces for PLA9 and PLA12. This again proves that in spite of a decrease in crystallinity, the relaxation strength reduces clearly indicating an increase of rigid amorphous fraction. Such a drastic change in the amorphous fraction as a function of LDH is due to the increased surface area-volume ratio or in other words an increased interfacial area.

So a possibility of having a dominated exfoliated morphology cannot be denied. Further BDS results will clarify the investigations.

### 7.1.3 Dielectric Spectroscopy Investigations

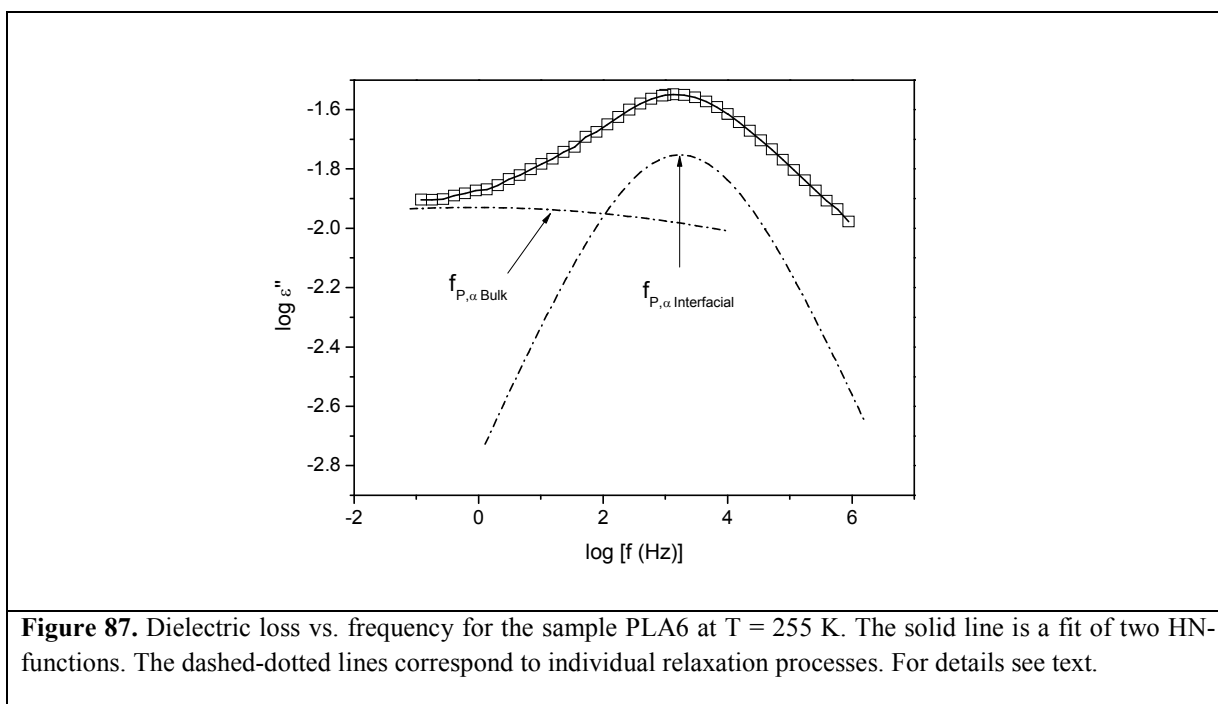


For the present analysis, the nomenclature of amorphous polymer is followed, i.e. for dynamic glass transition  $\alpha$ -relaxation and for localized fluctuations  $\beta$ -relaxation. The BDS measurements were carried out in a frequency range of  $10^{-1}$  to  $10^6$  Hz, and in a temperature range of 173 to 413 K. As discussed about pure PLA in section 4.2.3, two relaxation processes were identified: At higher temperatures (lower frequencies),  $\alpha$ -relaxation which corresponds to dynamic glass transition or polymer segmental fluctuations, whereas at lower temperatures (higher frequencies),  $\beta$ -relaxation related to localized fluctuations in the polymer chain. The latter is most probably related to the fluctuations of the C=O group present in the main polymer chain. For polymers like PLA, which has a polar group in the backbone, an additional process termed as normal mode is also observed.<sup>145</sup> It is related to the fluctuations of the entire polymer chain and occurs at very high temperatures (above  $T_m$ ). However, in the present case such a normal mode was not observed. In case of the nanocomposites an additional process is observed termed as interfacial. Similar to PP/LDH and PE/LDH, this interfacial process originates from fluctuations of the molecules close to the LDH sheets; however the bulk process originates mainly from the polymer matrix. A substantial increase in the intensity of the two processes (interfacial and bulk) is observed in

Figure 86 which is due to the increase in the amount of polar group as a function of LDH. This can be related to the increase in the amount of SDBS. The polar head group of SDBS is attached to the LDH sheets, whereas in some cases the SDBS might also desorb from PLA and act as a plasticizer. This also proves the initial reduction in calorimetric  $T_g$  values (Figure 84). Considering the interaction of LDH with PLA, it would be two fold, one through SDBS and other directly with C=O. The interfacial process is mainly related to the fluctuations of the SDBS, however a preferential interaction of C=O with the LDH cannot be denied which might also contribute to this process. The bulk process is nevertheless mainly related to the fluctuations of the PLA segments (C=O bond). Some contribution can also be from SDBS which might be dispersed in the matrix. The dielectric behavior of PLA based LDH nanocomposites is different from PP and PE. This is mainly due to a dielectrically visible polymer matrix (PLA). Other than the above discussed processes, an additional process is observed for concentrations above PLA3. The origin of this process needs further investigations and so it is still under discussion.

### Analysis of Interfacial and Bulk like Processes

In the present case too, the HN function (Eq. 31) was fitted to the measured data.



At higher frequencies a well defined loss peak can be observed (see Figure 86). A more careful inspection of this peak shows that it has a pronounced low frequency contribution which originates from a further relaxation process. A fit of the data by only one HN-function

results in a parameter set with unreasonable values. Therefore, the spectra were analyzed by fitting two HN-functions to the data (see Figure 87).

The interfacial process appearing at lower frequencies is assigned to the PLA segments in close proximity of the LDH layers. Their mobility is hindered by the strong adsorption of the polar head group of the surfactants and also the C=O bond from the polymer to the LDH layers. Bulk process at higher frequencies is related to the fluctuations originating from PLA matrix which is not observed in case of PP and PE.

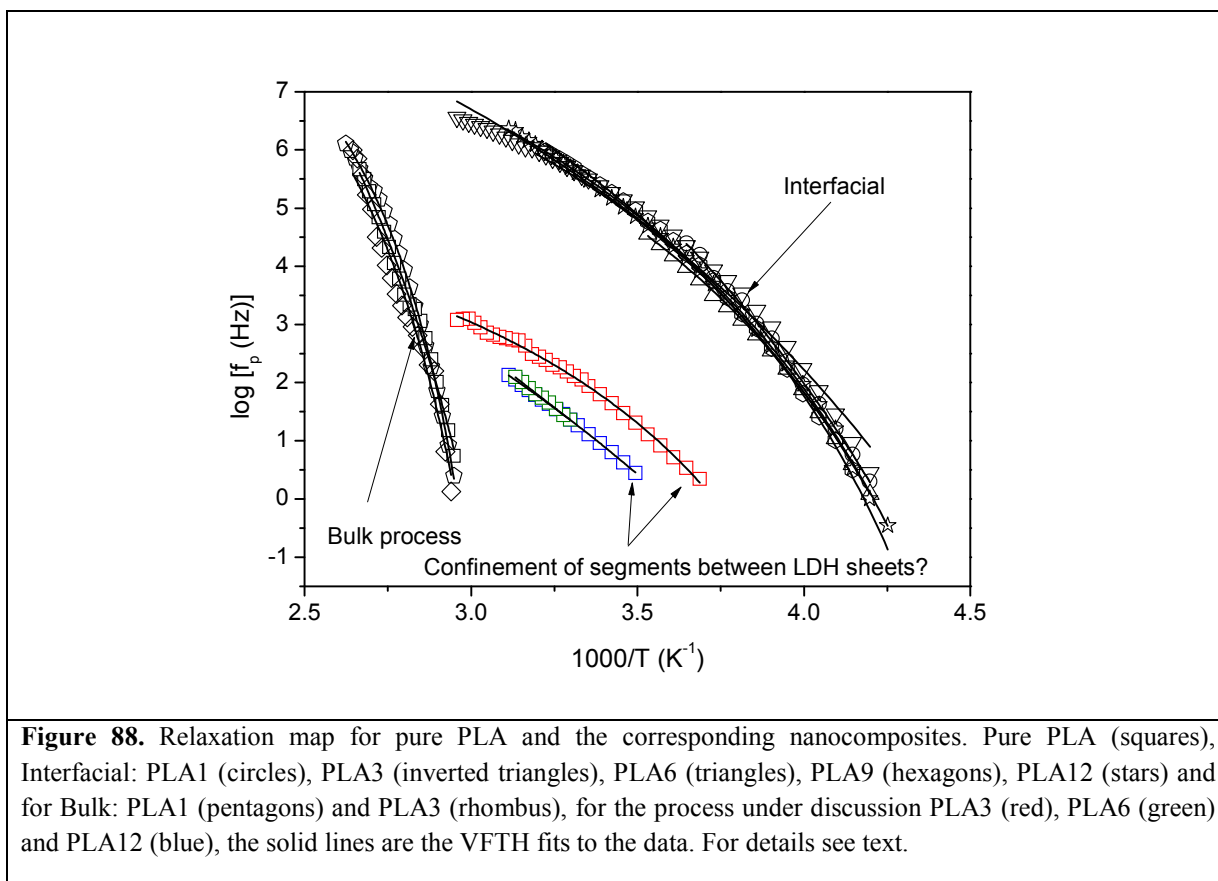


Figure 88 displays the relaxation map for pure PLA and corresponding nanocomposites. The temperature dependence of the relaxation rates is curved and well described by the VFTH function. The VFTH fit parameters are given in Table 11. Both the processes identified follow the glassy dynamics. It was possible to analyze the Bulk process for PLA1 and PLA3; it collapses well with the  $\alpha$ -relaxation of pure PLA. This indicates that the origin of such a process is from segmental fluctuations of the polymer matrix and it does not show any influence of the nano-filler. The interfacial process occurs in a temperature range lower than bulk polymer and it is concentration independent. Moreover, its curvature is very much different than bulk process or in other words the fragility parameter;  $D$  is higher in case of



the interfacial process. This is due to an increased molecular mobility for molecules close to LDH sheets. For higher concentration i.e. PLA6, PLA9 and PLA12; it was possible to analyze only the interfacial process. This could be due to the overlapping of the bulk process with high temperature conductivity. The other possibility is that the morphology is predominantly delaminated and so LDH sheets are completely dispersed in the polymer matrix making the bulk like behavior difficult to be analyzed by HN function. Overlapping of the interfacial and bulk process can also not be neglected.

An additional process is observed which is still under discussion. The temperature dependence of the relaxation rates of this process is also curved and follows glassy dynamics. At first instance, this process probably originates from the fluctuations of the polymer segments confined between intercalated LDH sheets. However, further investigations needs to be done to fully understand its origin.

**Table 11. VFT fit parameters for pure PLA, interfacial and bulk processes.**

	<b>Interfacial</b>					<b>Bulk</b>				
<b>Sample Codes</b>	<b>log[f<sub>∞</sub>(Hz)]</b>	<b>A<sub>0</sub> (K)</b>	<b>T<sub>0</sub> (K)</b>	<b>T<sub>g</sub><sup>diel</sup> (K)</b>	<b>D</b>	<b>log[f<sub>∞</sub>(Hz)]</b>	<b>A<sub>0</sub> (K)</b>	<b>T<sub>0</sub> (K)</b>	<b>T<sub>g</sub><sup>diel</sup> (K)</b>	<b>D</b>
<b>PLA</b>	-	-	-	-	-	12	487.1	297	339	3.8
<b>PLA1</b>	12	789.8	170	237	10.6	12	555.6	289	336	4.4
<b>PLA3</b>	12	965.7	151	237	14.7	12	545.1	293	340	4.3
<b>PLA6</b>	12	888.2	163	237	12.5	-	-	-	-	-
<b>PLA9</b>	12	842.5	167	238	11.6	-	-	-	-	-
<b>PLA12</b>	12	889.9	164	238	12.4	-	-	-	-	-

### ***β-relaxation***

Other than these processes, a β-relaxation was also identified in the present case. This process is related to localized fluctuations, such as a side group or part of the main polymer chain. In case of PLA, C=O exists in the main chain and hence this process can be related to its rotational or transitional fluctuations.<sup>111</sup> The HN function was fitted to the β-relaxation and the mean relaxation rates were estimated.

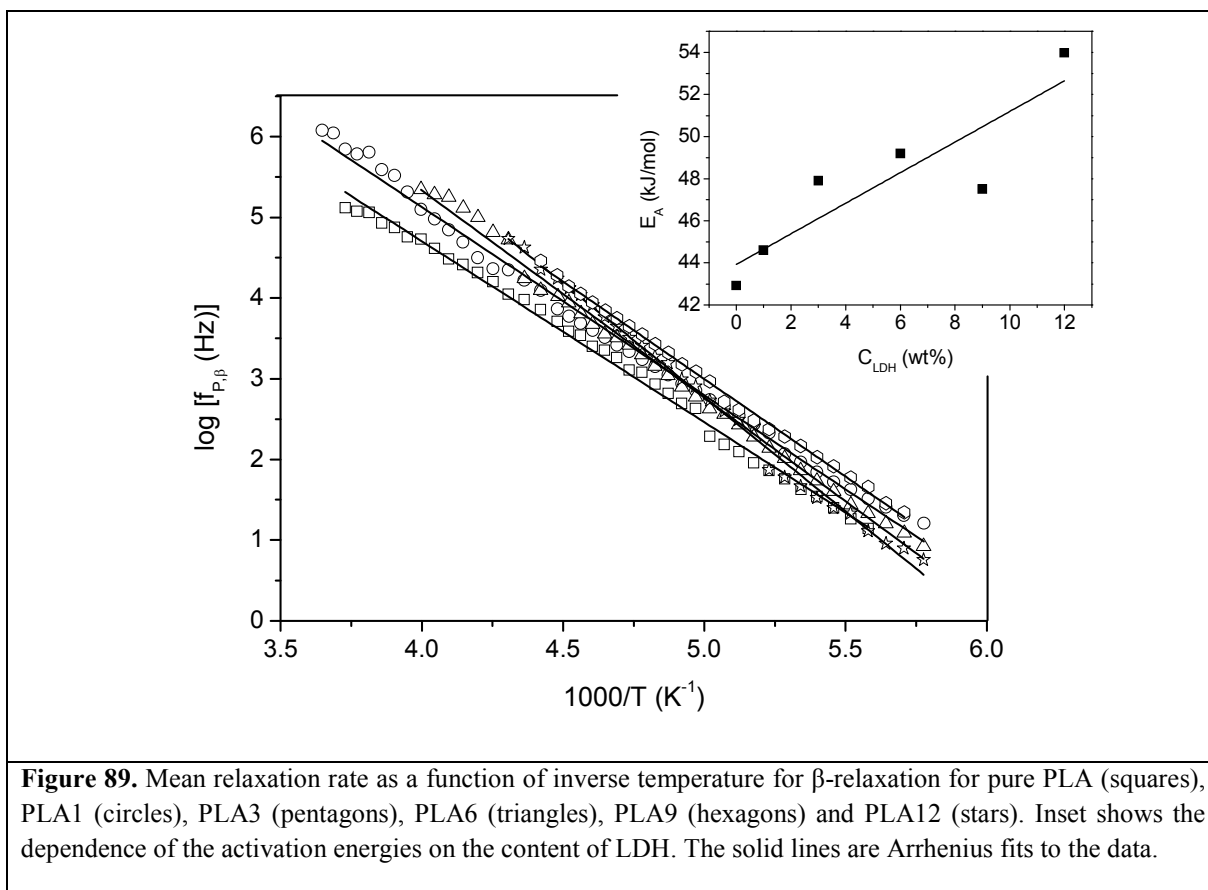
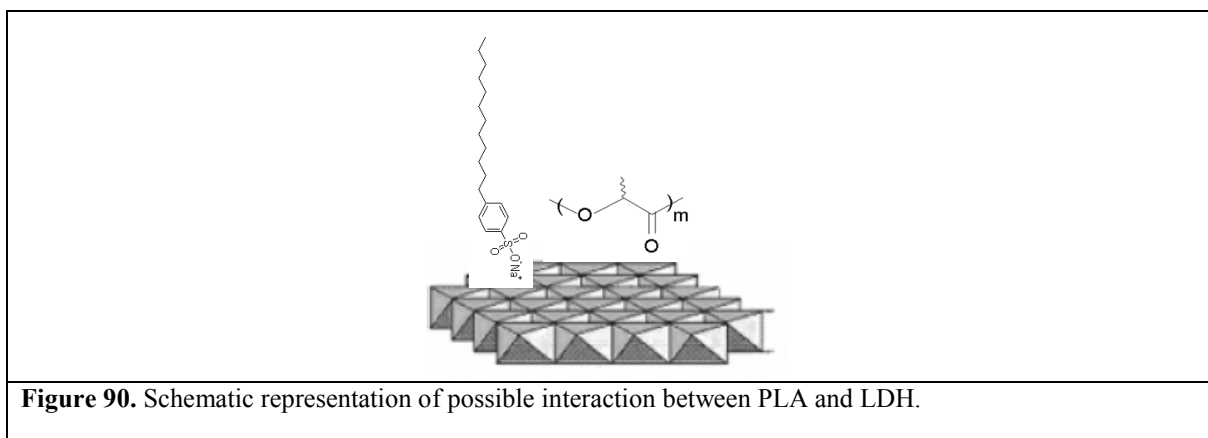


Figure 89 shows the relaxation map for  $\beta$ -relaxation and its mean relaxation rate varies linearly as a function of the inverse temperature. It is described by Arrhenius function (Eq. 1), and the activation energies are then calculated from the slopes of the fits. The inset of Figure 89 shows the plot of activation energies as a function of LDH content. There is a clear increase in the values of the activation energies with increasing concentration of LDH. This indicates that the fluctuations of the C=O is hindered with increasing LDH in the polymer. The following picture can be drawn:

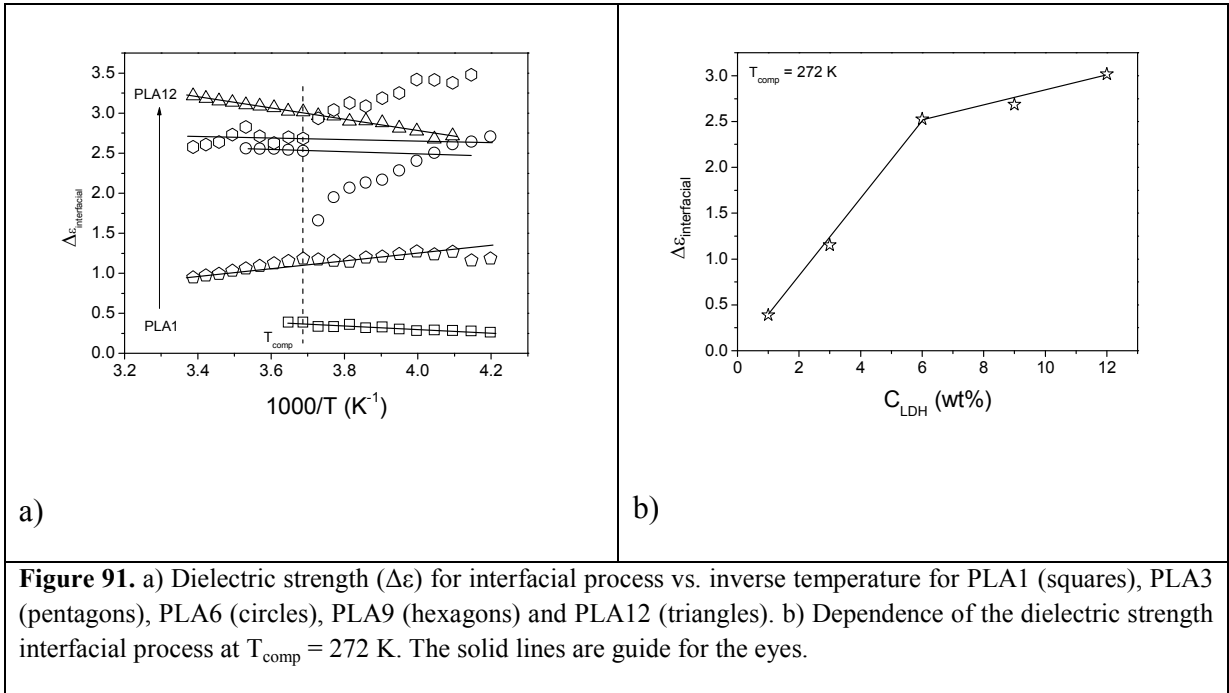


Taking into consideration the schematic representation of Figure 90, the following conclusion can be derived. With increasing LDH content the amount of PLA reduces, however the increase in activation energies indicates an increase in interfacial area of the nanocomposites. This hints again to a possibly exfoliated morphology, as due to delamination of the LDH sheets more interfaces are formed and the interaction between C=O and PLA is encouraged. The fluctuations of SDBS at the interface of LDH might also contribute to the  $\beta$ -relaxation, however the chances are few as the size of this molecule is around 2.5 nm. Such a length corresponds to glassy dynamics.<sup>77</sup> Some contributions might be from the fluctuations of the polar head group of the SDBS. The following table gives the Arrhenius fit parameters.

**Table 12. Calculated Arrhenius fit parameters.**

Sample name	$\log [f_{\infty} \text{ (Hz)}]$	$E_A \text{ (kJ/mol)}$
PLA	13.6	42.9
PLA1	14.4	44.6
PLA3	13.5	47.9
PLA6	15.6	49.2
PLA9	15.3	47.6
PLA12	16.9	53.9

### Dielectric strength ( $\Delta\epsilon$ )



The dielectric strength for the interfacial process is plotted as a function of inverse temperature in Figure 91a. The values increase as a function of LDH content, which is due to the increase in the amount of SDBS. From Figure 91b, it can be seen that the dependence of the dielectric strength at a comparison temperature ( $T_{\text{comp}}$ ) of 272 K changes slope after PLA6. This indicates a change in the morphology such as aggregation of LDH sheets at higher concentrations. Aggregation can trap some amount of LDH which cannot be probed by BDS. Such a finding is also evident from the thermal investigations explained for concentrations above PLA6, 1) nearly constant  $T_g$  values (Figure 84), 2) drastic decrease in the thermal relaxation strength (Inset, Figure 85) and 3) increase in the amount of RAF (Figure 85).

## 7.2 Nanocomposites based on PLA and Carbon Nanotubes

Carbon nanotubes (CNT) are employed for nanocomposites due to their exceptional improvement in electrical and mechanical properties of the polymer.<sup>146,147</sup> Compared to carbon black the electrical conductivity can be improved by lower content of CNT. The reason is the high aspect ratio (ratio of length to diameter) of CNT compared to more spherical carbon black particles.<sup>148,149</sup> So this high aspect ratios (100 – 1000) enable electrical percolation of the CNT within polymers. CNTs have exceptional mechanical

properties, e.g. tensile strength of 20 GPa and moduli of the order of 1 TPa. However, the CNT/polymer interaction is necessary to improve the load transfer at the interface. For this a homogeneous dispersion of the CNT in the polymer matrix has to be improved. This is quite difficult due to the intermolecular van der Waals interactions between the nanotubes which encourage aggregation. In most cases, melt mixing is employed for the preparation of the nanocomposites, since aggregate formation can be minimized by appropriate application of shear during processing.

### 7.2.1 Preliminary BDS Investigations

BDS is employed to investigate the percolation structure. For sinusoidal electric fields, the complex conductivity is related to complex dielectric function by the following equation:

$\sigma^*(\omega) = i\omega\epsilon_0\epsilon^*(\omega)$	<b>(47)</b>
--	-------------

where,  $\sigma^*(\omega)$  is the complex conductivity, given by  $\sigma^*(\omega) = \sigma'(\omega) + i\sigma''(\omega)$  where,  $\sigma'$  and  $\sigma''$  are the real and imaginary part of the complex conductivity respectively. The real part of the conductivity is related to the imaginary part of the dielectric function in the following way:

$\sigma'(\omega) = \omega\epsilon_0\epsilon''(\omega)$	<b>(48)</b>
--	-------------

Measured over large frequency and temperature range it enables to analyze the underlying mechanisms of charge transport. At higher frequencies, the charge carriers are driven by the external electric field over distances corresponding to atomic length scales, while in the direct current (DC) limit of  $\omega \rightarrow 0$  they propagate on some percolation path from one side of the sample to the other side. Thus, with decreasing frequency a length scale is involved going from microscopic to macroscopic dimensions.<sup>150</sup>

In disordered systems like polymers the charge transport takes place due to hopping conduction. The motion of a charge in disordered systems is accompanied by an electrical relaxation. A hop to a new site can lead to a successful charge transport only if the polarization cloud follows otherwise it will jump back. This mutual electric relaxation requires a relaxation time  $\tau_\sigma$ . For  $\omega \ll 1/\tau_\sigma$ , it supports the charge transport and causes a contribution to the electrical relaxation which increases with decreasing frequency. This is called the Debye-Hückel-Falkenhagen theory.<sup>151,152</sup>

The real part of the conductivity  $\sigma'$  has a plateau which corresponds to the DC conductivity ( $\sigma_{DC}$ ) on the low frequency side which bends off at a certain critical frequency  $\omega_c$  and results for  $\omega \gg \omega_c$  in a power law dependence of the type  $\sigma' \sim \omega^s$  ( $s \leq 1$ ).

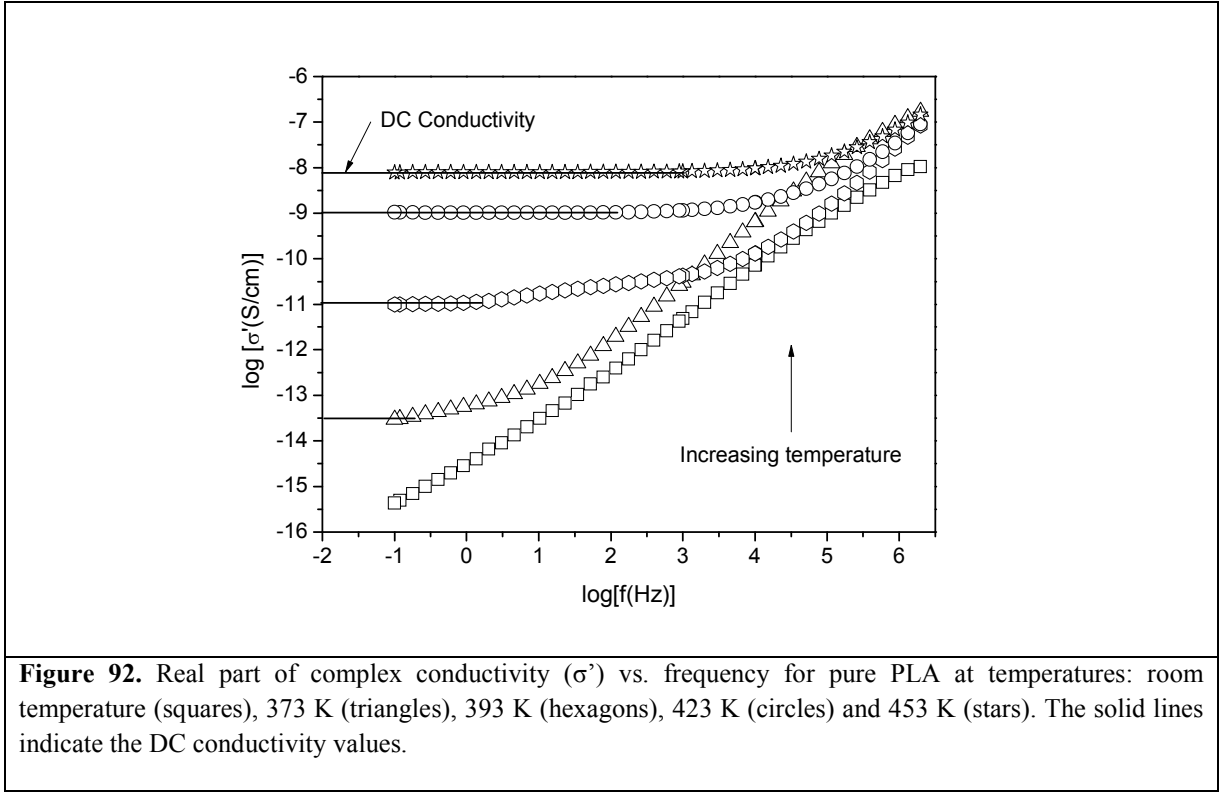
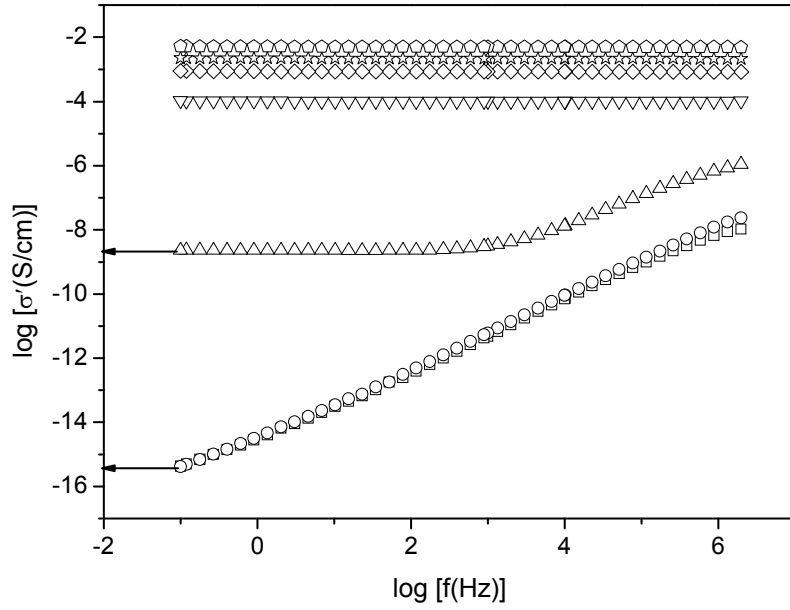


Figure 92 shows the dependence of the real part of the conductivity for pure PLA at various measured temperatures over a frequency range. After 373 K, a DC conductivity plateau is observed, the value of which is obtained by extrapolation of this plateau on Y-axis. As expected, it increases with temperature as the charge carriers become mobile and they move freely within the sample. The length scale involved with increasing DC conductivity values goes from microscopic to macroscopic.

With the understanding of the theory mentioned above, PLA based CNT nanocomposites with various compositions were investigated employing BDS at room temperature and in a frequency range of  $10^{-1}$  to  $10^6$  Hz.



**Figure 93.** Real part of the complex conductivity ( $\sigma'$ ) vs frequency at room temperature for various compositions of the nanocomposites. Pure PLA (squares), PLAC0.1 (circles), PLAC0.5 (triangles), PLAC1 (inverted triangles), PLAC2 (rhombuses), PLAC4 (stars) and PLAC8 (pentagons).

Figure 93 shows the dependence of the real part of complex conductivity ( $\sigma'$ ) as a function of dielectric frequency. For PLAC0.1, no conductivity is observed, as due to very low amount of CNT present no aggregation is observed. But in case of PLAC0.5, a DC conductivity ( $\sigma_{DC}$ ) plateau is observed. Above these concentrations, only DC conductivity is observed. This indicates that the conductivity takes place across the sample measured (macroscopic). The reason in this case is the aggregation of the CNTs, which forms a percolating network across which the charge carriers hop and thus DC conductivity is observed at concentrations above 0.5 wt%. The following equation describes the dependence of DC conductivity ( $\sigma_{DC}$ ) on filler content ( $C$ ) near the percolation threshold  $C_c$  percolation in two component systems.<sup>149</sup>

For concentrations of the fillers above the percolation threshold ( $C > C_c$ ),

$$\sigma_{DC} = \sigma_{0A} \left( \frac{C_A - C_c}{1 - C_c} \right)^t \quad (49)$$

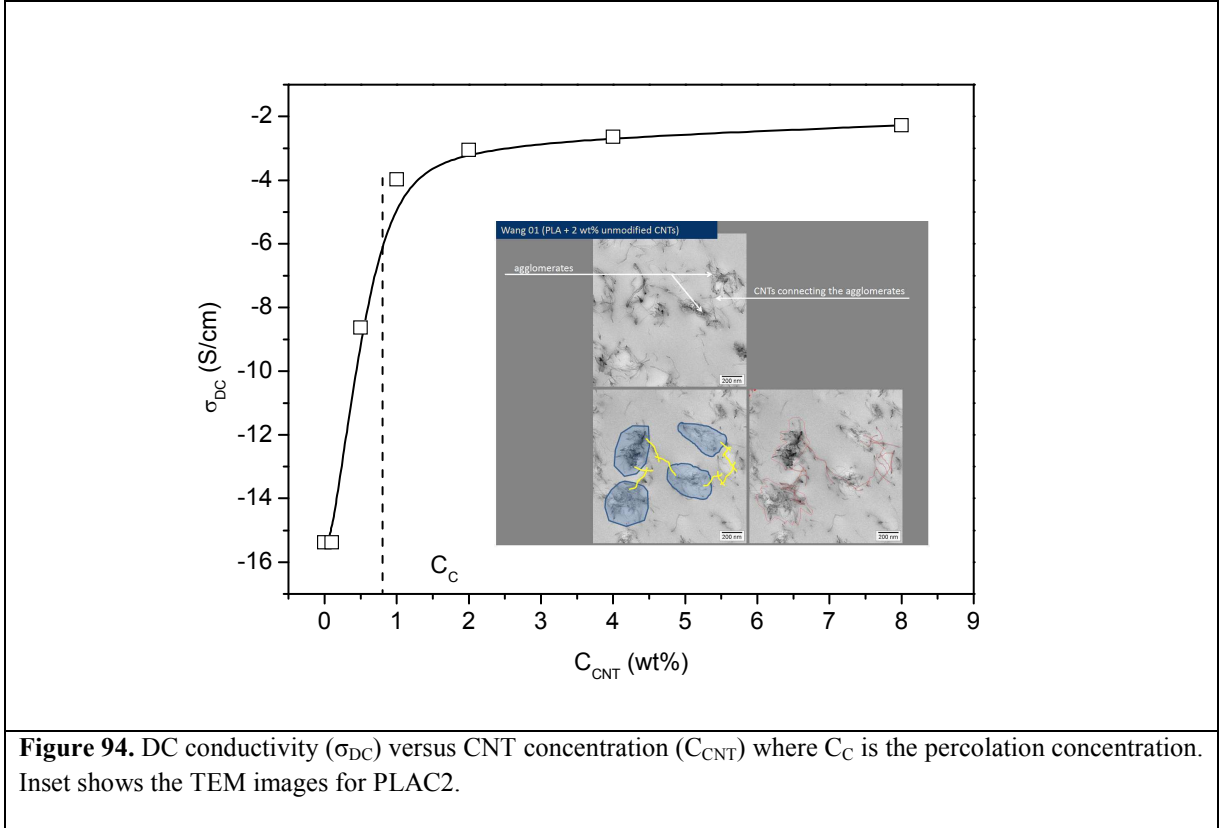
$C_A$  is the volume concentration of the conductive agglomerates contributing to the percolation network,  $t$  is an exponent, and  $\sigma_{0A}$  is the conductivity of agglomerates formed by

CNTs. The DC conductivity below the percolation threshold  $C_c$  ( $C < C_c$ ) as a function of agglomerate concentration is given by,

$\sigma_{DC} = \sigma_{0M} \left( \frac{C_c - C_A}{C_c} \right)^{-s} \quad (50)$	
--	--

$\sigma_{0M}$  is the conductivity of the polymer matrix.

In the present case, a percolation representation is given for PLA/CNT nanocomposites.



From Figure 94, it can be estimated that the percolation occurs between 0.5 and 1 wt%. For concentrations above that the CNTs form a percolating network and only conductivity can be observed. It can be seen from the TEM image in the inset how the CNTs form networks to promote conductivity. However, a more detailed analysis will be done employing X-ray scattering and DSC to investigate this further. The exact value of  $C_c$  cannot be predicted as samples with very low concentrations are difficult to prepare and hence prove the power law dependences (Eq. 49 and 50). Comparing the different nanocomposites it has to be taken into consideration that no universal picture can be drawn; each nanocomposite has to be treated individually with respect to its components (polymer, filler, chemical modification, or other additives) and preparation (filler modification, dispersion, processing).



Nanocomposites were prepared in a two step procedure by melt mixing of polymer and layered double hydroxides (LDH) where maleic anhydride grafted PP and PE was used as compatibilizer for PP/LDH and PE/LDH. LDH have been modified by sodium dodecylbenzene sulfonate (SDBS) as a surfactant. Nanocomposites were also prepared employing PLA and CNT by melt mixing.

The homogenous distribution on the mm length scale of the nanoparticles inside the polymer matrix across the whole macroscopic sample area was investigated at the synchrotron micro focus beamline  $\mu$ Spot (BESSY II of the Helmholtz Centre Berlin for Materials and Energy). The results show collapsing of 3 and 5 spectra with each other for PLA/LDH and PP/LDH & PE/LDH respectively, measured with a spot of 0.1 mm at different locations over the 30 mm sample indicating complete homogeneity of the nanocomposite.

Small angle X-ray scattering (SAXS) analysis indicates a nearly equal stack size of O-LDH for nanocomposites as compared to pure O-LDH. It is concluded that the LDH layers in the nanocomposites are intercalated in the polymer matrix. Average number of LDH layers in the nanocomposites is calculated.

The thermal properties of the nanocomposites were investigated by differential scanning calorimetry. Both the melting and crystallization enthalpies decrease with increasing concentration of LDH. Reduced to the content of the polymer, the phase transition enthalpies  $\Delta H_{\text{Red}}$  decreases linearly with the concentration of the nanofiller. The extrapolation of  $\Delta H_{\text{Red}}$  to zero leads to a limiting concentration of ca. 40 wt% and 45 wt% LDH for PP and PE respectively where the crystallization should be completely suppressed by the presence of the nanoparticles. This was also confirmed by WAXS investigations, where Gaussians were fitted to the crystalline reflections and the amorphous halo, and the area below the peaks were calculated and used to determine the degree of crystallinity. This also decreased linearly and extrapolation of the trend to zero crystallinity led to estimations of values of wt% LDH which was in agreement with the DSC results. PLA/LDH based nanocomposites showed an increase in crystallinity at first (PLA1) and then a linear decrease as a function of LDH content. Again the extrapolation of this linear trend to zero enthalpy estimated a limiting concentration of 14 wt% of LDH. The increase in the crystallinity for low concentration is also observed by WAXS, however the limiting concentration was determined to be approximately 20 wt%. Such a difference is attributed to the scatter in the

WAXS results. An increase in the amount of rigid amorphous fraction (RAF) was calculated for both the nanocomposites. This is due to the fact that the polymer molecules close to the LDH sheets are sterically hindered which reduces their mobility which is investigated by BDS. The presence of the immobilized layer is also confirmed by  $\Delta C_p$ , which is the relaxation strength and related to the amount of amorphous fraction in the nanocomposites.

For PP/LDH and PE/LDH, the intensity of the  $\beta$ -relaxation (dynamic glass transition) increases strongly with increase in concentration of LDH for the nanocomposites. This increase in the dielectric relaxation strength of the dynamic glass temperature is related to the increase in the concentration of the quite polar SDBS surfactant molecules which increases with the concentration of LDH. The surfactants are adsorbed onto the LDH layers and its alkyl tails form a common phase with the PP and PE segments close to the nanoparticles. Therefore, a detailed investigation of the  $\beta$ -relaxation provides information about the molecular mobility and structure in the interfacial area between the LDH layers and the matrix polymer. It was shown that the peak of the  $\beta$ -relaxation consists of two processes. These processes are assigned to regions of different molecular mobility at different distances from the LDH nanofillers. The temperature dependence of the relaxation rates of both processes follows the Vogel-Fulcher-Tammann-Hesse formula which indicates glassy dynamics. The difference in the corresponding glass temperatures measured by the ideal glass transition or Vogel temperature  $T_0$  is about 20 K and 15 K for PP and PE respectively. The low frequency component of the  $\beta$ -relaxation of the nanocomposites is assigned to polymer segments in a close proximity of the LDH because the SDBS molecules are strongly adsorbed at the surfaces of the nanofiller and have therefore a strongly reduced molecular mobility. The high frequency process of the  $\beta$ -relaxation is related to polymer segments at a farther distance from the LDH layers. The higher molecular mobility can be related to three facts. Firstly to plasticization of the alkyl tail of the SDBS surfactants terminated with a methyl group. This methyl group is sterically demanding than  $\text{CH}_2$  units present in PE and PP and introduce more free volume leading to a higher molecular mobility. Secondly, the packing density of the PP and PE segments can be lower, close to the LDH layers leading also to a higher mobility. Thirdly, the SAXS data shows that polymer chains are intercalated inside the layers. This can be regarded as confinement for it, which should lead according to the literature to a decrease of molecular mobility.<sup>41,153</sup>

The derivative technique was applied for PE/LDH  $[d(\log f_p)/dT]^{-1/2}$  in order to confirm the glassy dynamics behavior of both the processes. The Vogel temperature  $T_0$  was determined

and compared to the values estimated by the VFTH fit.

For PP/LDH, the concentration dependence of the dielectric strength for the  $\beta$ -relaxation changes strongly for a loading higher than 10 wt%. This is probably due to the fact that for high filler concentrations the LDH sheets (or small LDH stacks) cannot arrange independently from each other. Therefore an optimal filler loading can be deduced from that dependence to be in that case below 10 wt%. For PE/LDH, the dielectric strength varies linearly as a function of concentration of LDH. In PP/LDH an additional  $\gamma$ -relaxation process was observed which is related to the localized fluctuations of the amorphous domains. The temperature dependence of the relaxation rates of the  $\gamma$ -relaxation follows the Arrhenius equation with activation energy of around 81 kJ/mol independent on the concentration of LDH. The relaxation strength of the  $\gamma$ -process increases with the concentration of the nanofiller. As the  $\gamma$ -relaxation is related to localized fluctuation in the amorphous regions of polypropylene, it is concluded that the content of the amorphous phase increases with increasing concentration of LDH. This is confirmed by a linear dependence of  $\Delta\epsilon_\gamma$  on the roughly estimated degree of crystallization.

The BDS investigations for PLA/LDH also identified various relaxation processes. However, in addition to the dynamic glass transition ( $\alpha$ -relaxation, in this case), a  $\beta$ -relaxation process related to localized fluctuations was also identified. This latter relaxation process might be related to the fluctuations of the C=O bond of the main chain. These processes are analyzed in detail. Similar to PP and PE nanocomposites, there is a strong increase in the intensity of the dielectric loss which is due to the increase in the amount of the surfactant SDBS. In case of PLA/LDH, the C=O group also possibly interacts with the LDH. Two processes which follow glassy dynamics were identified, however, the process related to molecules farther from LDH was only observed for low concentrations. At higher concentration only interfacial process, related to molecules close to LDH was identified. This hints to an increased interfacial area as a function of LDH content. This point is further proved by analyzing the  $\beta$ -relaxation and estimating their activation energies by Arrhenius function. The value of the activation energies increased from pure PLA (42 kJ/mol) to around 54 kJ/mol for highest concentration. The fluctuation of C=O is more restricted with concentration of LDH, again hinting to increased interfacial area. All this leads to a conclusion that probably in this case the nanocomposites are predominantly exfoliated as compared to PP/LDH and PE/LDH which are more intercalated.

The PLA/CNT nanocomposites showed that between 0.5 and 1 wt% of CNT, a percolating network of the nanotubes is formed which leads to DC conductivity. This is due to the high aspect ratio of the CNTs and also the van der Waals interaction between the nanotubes which forms a network leading to conductivity. A more detailed analysis needs to be done in order to characterize them.

### **Future Outlook**

This thesis presents the results and analysis of the nanocomposites mainly LDH based by using various complementary characterization methods. This is done successfully for the materials mentioned in this work. As a future outlook, various other polymers which are of commercial interest with various types of LDH (NiAl, CoAl etc.) can be investigated by using these well established characterization techniques. Other than LDH, various other fillers such as carbon nanotubes, silica particles (functionalized), graphene sheets etc. can also be employed for preparing various nanocomposites. The structure-property relationships of these different nanocomposites need to be investigated in order to derive generalized models.

Other than the techniques mentioned in this thesis, a comparison of BDS results with mechanical analysis like Dynamic Mechanical Analyzer (DMA) and Rheology can also be employed and compared. From industry point of view, mechanical properties are always of interest.

## References

---

- (1) Manson, J. A.; Sperling, L. H. *Polymer Blends and composites* Plenum Press, N.Y. **1976**.
- (2) LeBaron, P.C.; Wang, Z.; Pinnavaia, T.J. *Appl. Clay Sci.* **1999**, *15*, 11.
- (3) Novak, B.M. *Adv. Mater.* **1993**, *5*, 422.
- (4) Alexandre, M.; Dubois, P. *Mater. Sci. Eng.* **2000**, *28*, 1.
- (5) Krishnamoorti, R.; Vaia, R. A. *Polymer Nanocomposites*, In *ACS. Symp. Ser., Vol. 804*, Washington, DC, **2002**.
- (6) Ray, S. S.; Okamoto, M. *Prog. Polym. Sci.* **2003**, *28*, 1539.
- (7) Nalwa, H. S. *Handbook of Organic-Inorganic Hybrid Materials and Nanocomposites*; American Scientific Publishers: Stevenson Ranch, CA, **2003**; Vol. 2.
- (8) Leuteritz, A.; Kretschmar, B.; Pospiech, D.; Costa, R.F.; Wagenknecht, U.; Heinrich, G. *Industry-relevant preparation, characterization and applications of polymer nanocomposites* In: *Polymeric nanostructures and their applications*, Nalwa, H.S. Ed. American Scientific Publishers: Los Angeles, **2007**.
- (9) Vaia, R. A.; Giannelis, E. P. *MRS Bull.* **2001**, *26*, 394.
- (10) Davis, S. R.; Brough, A. R.; Atkinson, A. *J. Non-Cryst. Solids* **2003**, *315*, 197.
- (11) Fragiadakis, D.; Pissis, P.; Bokobza, L. *Polymer* **2005**, *46*, 6001.
- (12) Hooper, J. B.; Schweitzer, K. S. *Macromolecules* **2005**, *38*, 8850.
- (13) Böhning, M.; Goering, H.; Fritz, A.; Brzezinka, K. W.; Turkey, G.; Schönhals A.; Schartel B. *Macromolecules* **2005**, *38*, 2764.
- (14) Jancar, J.; Douglas, J. F.; Starr, F. W.; Kumar, S. K.; Cassagnau, P.; Lesser, A. J.; Sternstein, S. S.; Buehler, M. J. *Polymer* **2010**, *51*, 3321.
- (15) Hussain, F.; Hojjati, M.; Okamoto, M.; Gorga, R. E. *Journal of Composite Materials*, **2007**, *40*, 1511.
- (16) Giannelis, E. P.; Krishnamoorti, R.; Manias, E. *Adv. Poly. Sci.* **1999**, *138*, 107.
- (17) K. Pielichowski et al., *Adv. Poly. Sci.*, **2006**, *201*, 225.
- (18) Kunag, Y.; Zhao, L.; Zhang, S.; Zhang, F.; Dong, M.; Xu, S. *Materials*, **2010**, *3*, 5220.
- (19) Spiess, H. W. *Macromolecules* **2010**, *43*, 5479.
- (20) Costa, F. R.; Saphiannikova, M.; Wagenknecht, U.; Heinrich, G. *Adv. Polym. Sci.* **2008**, *210*, 101.
- (21) Xu, Z.P.; Braterman, P.S. *J. Mater. Chem.* **2003**, *13*, 268.

- 
- (22) Schönhals, A.; Goering, H.; Costa, F. R.; Wagenknecht, U.; Heinrich, G. *Macromolecules* **2009**, *42*, 4165.
- (23) Iijima, Sumio, *Nature (London, United Kingdom)*, **1991**, *354*, 6348.
- (24) Ajayan, P. M. and Zhou, O. Z., *Carbon Nanotubes*, **2001**, *80*, 391.
- (25) Krause, B; Ritschel, M; Täschner, C; Oswald, S; Gruner, W; Leonhardt, A; *Compos Sci Technol* **2010**, *70*, 151.
- (26) Giannelis, E. P. *Adv. Mater.*, **1996**, *8*, 29.
- (27) Gilman, J. W.; Jackson, C. L.; Morgan, A. B.; Harris, R, Jr. *Chem. Mater.*, **2000**, *12*, 1866.
- (28) Ray, S. S., *J. Ind. Eng. Chem.* **2006**, *12*, 811.
- (29) Heilmann, A. *Polymer Films with Embedded Metal Nanoparticles*, Springer, Berlin, **2003**.
- (30) Xie, X. L.; Mai, Y. W.; Zhou, X. P.; *Mater. Sci. Eng. Res.* **2005**, *49*, 89.
- (31) Bernholc, J.; Brenner, D.; Nardelli, M. B.; Meunier, V.; Roland, C. *Annu. Rev. Mater. Res.* **2002**, *32*, 347.
- (32) Moniruzzaman, M.; Winey, K. I. *Macromolecules* **2006**, *39*, 5194.
- (33) Lichtenhan, J. D.; Schwab, J. J.; Reinerth, W. A. *Chem. Innov.* **2001**, *31*, 3.
- (34) Joshi, M.; Butola, B. S. *J. Macromol. Sci. B Polym. Rev.* **2004**, *C44*, 389.
- (35) Hao, N.; Böhning, M.; Goering H.; Schönhals, A. *Macromolecules* **2007**, *40*, 2955.
- (36) Hao, N.; Böhning, M.; Schönhals, A. *Macromolecules* **2007**, *40*, 9672.
- (37) Hao, N.; Böhning, M.; Schönhals, A. *Macromolecules* **2010**, *43*, 9417.
- (38) Preschilla, N.; Sivalingam, G.; Abdul Rasheed, A.S.; Tyagi, S.; Biswas, A.; Bellare, J. *Polymer*, **2008**, *49*, 4285.
- (39) Davis, R. D.; Bur, A. J.; McBrearty, M.; Lee, Y. H.; Gilman, J. W.; Start, P. R. *Polymer* **2004**, *45*, 6487.
- (40) Ding, Y.; Pawlus, S.; Sokolov, A. P.; Douglas, J. F.; Karim, A.; Soles, C. L. *Macromolecules* **2009**, *42*, 3201.
- (41) Anastasiadis, S. H.; Karatasos, K.; Vlachos, G.; Manias, E.; Giannelis, E. P. *Phys. Rev. Lett.* **2000**, *84*, 915.
- (42) Schwartz, G. A.; Bergman, R.; Swenson, J. *J. Chem. Phys.* **2004**, *120*, 5736.
- (43) Mijovic, J.; Lee, H. K.; Kenny, J.; Mays, J. *Macromolecules* **2006**, *39*, 2172.

- 
- (44) Elmahdy, M. M.; Chrissopoulou, K.; Afratis, A.; Floudas, G.; Anastasiadis, S. H. *Macromolecules* **2006**, *39*, 5170.
- (45) Kopesky, E. T.; Haddad, T. S.; McKinley, G. H.; Cohen, R. E. *Polymer* **2005**, *46*, 4743.
- (46) Cole, K. C. *Macromolecules* **2008**, *41*, 834.
- (47) Wurm, A.; Ismail, M.; Kretzschmar, B.; Pospiech, D.; Schick, C. *Macromolecules* **2010**, *43*, 1480.
- (48) Kotal, M.; Srivastava, S. K.; Manu, S. K. *Journal of Nanoscience and Nanotechnology* **2010**, *10*, 5730.
- (49) Costa, F. R.; Abdel-Goad, M.; Wagenknecht, U.; Heinrich, G. *Polymer* **2005**, *46*, 4447.
- (50) Lee, W. D.; Im, S. S.; Lim, H. M.; Kim, K. J. *Polymer* **2006**, *47*, 1364.
- (51) Ajayan, P. M.; Stephan, O.; Colliex, C.; Trauth, D. *Science* **1994**, *265*, 1212.
- (52) Spitalsky, Z.; Tasis, D.; Papagelis, K.; Galiotis, C. *Prog. Polym. Sci.* **2010**, *35*, 357.
- (53) Coleman, J. N.; Khan, U.; Blau, W. J.; Gunko, Y. K. *Carbon* **2006**, *44*, 1624.
- (54) Sperling, L. H. *Physical Polymer Science*; John Wiley & Sons: New York, **1986**.
- (55) Hodge, I. M. *Journal of Non-Crystalline Solids* **1994**, *169*, 211.
- (56) Schönhals, A and Kremer, F. Amorphous Polymers In: Matyjaszewski, K and Möller, M (Eds) *Polymer Science: A Comprehensive Reference*, Vol 1, Amsterdam: Elsevier BV, **2012**, pp 201-226.
- (57) W. Kauzmann, *Chemical Reviews* **1948**, *43*, 2.
- (58) J. H. Gibbs *J. Chem. Phys.* **1956**, *25*, 185.
- (59) J. H. Gibbs, and E. A. DiMarzio, *J. Chem. Phys.* **1958**, *28*, 373.
- (60) J. H. Gibbs in *Modern Aspects of the Vitreous State*, J. D. Mackenzie (Butterworth), London, **1960**.
- (61) E. A. DiMarzio, and J. H. Gibbs, *J. Polym. Sci. A*, **1963**, *1*, 1417.
- (62) E. A. DiMarzio, *J. Res. Natl. Bur. Stds.* **1964**, *68A*, 611.
- (63) Gehlsen, M. D.; Bates, F. S. *Macromolecules* **1993**, *26*, 4122.
- (64) Demoulin, C.; Montrose, C. J.; Ostrowski, N. *Physical Review A* **1974**, *9*, 1740.
- (65) Mezei, F.; Knaak, W.; Farago, B. *Physical Review Letters* **1987**, *58*, 571.
- (66) Boehmer, R.; Kremer, F. In *Broadband Dielectric Relaxation Spectroscopy*, 1. Ed.; Kremer, F and Schönhals, A. Eds. Springer: Berlin, **2002**; Chapter 17, pp 225-286.
- (67) Kremer, F.; Schönhals, A. In *Broadband Dielectric Relaxation Spectroscopy*, 1. Ed.; Kremer, F and Schönhals, A. Eds. Verlag: Berlin, **2002**.

- 
- (68) Vogel, H. *Physikalische Zeitschrift* **1921**, 22, 645.
- (69) Fulcher, G. S. *Journal of the American Ceramic Society* **1925**, 8, 339.
- (70) Tammann, G.; Hesse, W. *Zeitschrift für Anorganische und Allgemeine Chemie* **1926**, 156, 245.
- (71) Angell, C. A. *J. Non-Cryst. Solids* **1991**, 13, 131.
- (72) Angell, C. A. *J. Res. Natl. Inst. Stand. Technol.* **1997**, 102, 171.
- (73) Kremer, F.; Schönhals, A. In *Broadband Dielectric Relaxation Spectroscopy*, 1. Ed.; Kremer, F and Schönhals, A. Eds. Verlag: Berlin, **2002**; pgs. 99 – 129.
- (74) Eyring, H. *Journal of Chemical Physics* **1936**, 4, 283.
- (75) Doolittle, A. K. *Journal of Applied Physics* **1951**, 22, 1471.
- (76) Cohen, M. H.; Turnbull, D. *Journal of Chemical Physics* **1959**, 31, 1164.
- (77) Donth, E. *J. Non-Cryst. Solids* **1982**, 53, 325.
- (78) Hempel, E.; Hempel, G.; Hensel, A.; Schick, C.; Donth, E. *J. Phys. Chem. B* **2000**, 104, 2460.
- (79) Sills, S.; Gray, T.; Overney, R.M. *J. Chem. Phys.* **2005**, 123, 134902.
- (80) Berthier, L.; Biroli, G.; Bouchaud, J.P.; Cipelletti, L.; El Masri, D.; L'Hote, D.; Ladieu, F.; Pierno, M. *Science* **2005**, 310, 1797.
- (81) Cangialosi, D.; Alegria, A.; Colmenero, J. *Phys. Rev. E* **2007**, 76, 011514.
- (82) Schönhals, A.; Kremer, F. Theory of Dielectric Relaxation Spectra in Broadband Dielectric Spectroscopy; Kremer, F.; Schönhals, A., Eds.; Springer: Berlin, **2002**; pg. 10.
- (83) Schönhals, A.; *Electrical and Dielectrical properties*, in *Polymer Testing*, 1. Ed; Grellman, W. and Seidler, S. Eds. Carl Hanser Verlag: Munich, **2007**; pg 339.
- (84) Kremer, F.; Schönhals, A. In *Broadband Dielectric Relaxation Spectroscopy*, 1. Ed.; Kremer, F and Schönhals, A. Eds. Verlag: Berlin, **2002**; pg. 226.
- (85) Cole, K. S.; Cole, R. H. *Journal of Chemical Physics* **1941**, 9, 341.
- (86) Davidson, D. W.; Cole, R. H. *Journal of Chemical Physics* **1950**, 18, 1417.
- (87) Havriliak, S.; Negami S. *Polymer* **1967**, 8, 161.
- (88) Havriliak, S.; Negami, S. *Polymer* **1969**, 10, 859.
- (89) Havriliak, S.; Negami, S. *Journal of Polymer Science Part C-Polymer Symposium* **1966**, 99.
- (90) Schönhals, A.; Kremer, F. "Analysis of Dielectric Spectra" In: F. Kremer, A. Schönhals Ed.; *Broadband Dielectric Spectroscopy*, Berlin: Springer, (**2002**) pp. 59.



- 
- (91) Hartmann, L.; Kremer, F. *J. Chem. Phys.* **2003**, *118*, 6052.
- (92) Steeman, P. A. M.; van Turnhout, J. In *Broadband Dielectric Relaxation Spectroscopy*, 1. Ed.; Kremer, F and Schönhals, A. Eds. Springer: Berlin, **2002**; pp 495-520.
- (93) Steeman, P. A. M.; Maurer, F. H. J.; Vanes, M. A. *Polymer* **1991**, *32*, 523.
- (94) Steeman, P. A. M.; Maurer, F. H. J. *Colloid and Polymer Science* **1990**, *268*, 315.
- (95) Glatter, O; and Kratky, O. *Small Angle X-ray Scattering*, Academic press, London, **1982**.
- (96) Hellweg, T. *The basic principles of the scattering experiments*. **2004**.
- (97) Stribeck, N. *X-ray scattering of soft matter*, Springer, **2007**.
- (98) Reading, M. K.; Luget, A.; Wilson, R. *Thermochimica Acta*, **1995**, *238*, 295.
- (99) Schaumburg, G. *Dielectric Newsletter* **1994**, *March*, 1.
- (100) Schaumburg, G. *Dielectric Newsletter* **1999**, *May*, 1.
- (101) Collin, R. E. *Foundations for Microwave Engineering*; McGraw-Hill: New York, **1996**.
- (102) Paris, O.; Li, C.; Siegel, S.; Weseloh, G.; Emmerling, F.; Riesemeier, H.; Erko, A.; Fratzl, P. *J. Appl. Crystallogr.* **2007**, *40*, S466.
- (103) Hammersley, A. P.; Svensson, S. O.; Hanfland, M.; Fitch, A. N.; Hausermann, D. *High Pressure Res.* **1996**, *14*, 235.
- (104) Sargsyan, A.; Tonoyan, A.; Davtyan, S.; Schick, C. *Eur. Polym. J.* **2007**, *43*, 3113.
- (105) Koh, Y. P.; McKenna, G. B.; Simon, S. L. *J. Polym. Sci., B: Polym. Phys.* **2006**, *44*, 3518.
- (106) Sarge, S. M.; Hemminger, W.; Gmelin, E.; Hohne, G. W. H.; Cammenga, H. K.; Eysel, W. *J. Therm. Anal.* **1997**, *49*, 1125.
- (107) Wang, D. Y.; Costa, F. R.; Vyalikh, A.; Leuteritz, A.; Scheler, U.; Jehnichen, D.; Wagenknecht, U.; Häussler, L.; Heinrich, G. *Chem. Mater.*, **2009**, *21*, 4490.
- (108) Burum, D. P.; Rhim, W. K.; *J. Phys. Chem.* **1979**, *71*, 944.
- (109) Costantino, U; Marmottini, F; Rocchetti, M; Vivani, R. *Eur. J. Inorg. Chem.* **1998**, *1439*, 1446.
- (110) Carraher, C. E., Jr *Polymer Chemistry: An Introduction*, 4th Ed., Marcel Dekker, NY, **1996**.
- (111) Mierzwa, M.; Floudas, G.; Dorgan, J.; Knauss, D.; Wegner, J. *Journal of Non-Crystalline Solids*, 307-310, **2002**, 296-303.
- (112) Starkweather, Jr. H. W.; Avakian, P. *Macromolecules*, **1993**, *26*, 5084.

- 
- (113) Wang, L.; He, X.; Lu, H.; Feng, J.; Xie, X.; Su, S.; Wilkie, C. A. *Polymers for advanced technologies*, **2011**, 22, 1131.
- (114) Lonjon, A.; Laffont, L.; Demont, P.; Dantras, E.; Lacabanne, C. *J. Phys. D: Appl. Phys.* **2010**, 43, 345401.
- (115) Homminga, D.; Goderis, B.; Dolbnya, I. Groeninckx, G. *Polymer* **2006**, 47, 1620.
- (116) Miltner, H.E.; Grossiord, N.; Lu, K.; Loos, J. Koning, C.E.; van Mele, B. *Macromolecules* **2008**, 41, 5753.
- (117) Pissis, P.; Laudat, J.; Daoukaki, D.; Kyritsis, A. *J. Non-Cryst. Solids* **1994**, 171, 201.
- (118) Puzenko, A.; Kozlovich, N.; Gutina, A.; Feldman, Y. *Phys. Rev. B*, **1999**, 60, 14349.
- (119) Gutina, A.; Antropova, T.; Rysiakiewicz-Pasek, E.; Virnik, K.; Feldman, Y. *Micropor. Mesopor. Materials*, **2003**, 58, 237.
- (120) Feldman, Y.; Puzenko, A.; Ryabov, Y. *Chem. Phys.* **2003**, 284, 139.
- (121) van den Berg, O.; Wübberhorst, M.; Picken S. J.; Jager, W. F. *J. Non-Cryst. Solids* **2005**, 351, 2694.
- (122) van den Berg, O.; Sengers, W. G. F.; Jager, W. F.; Picken S. J.; Wübberhorst, M. *Macromolecules* **2004**, 37, 2460.
- (123) Schlosser, E.; Schönhals, A.; Carius, H. E.; Goering, H. *Macromolecules* **1993**, 26, 6027.
- (124) Jacobs, J.D.; Koerner, H.; Heinz, H.; Farmer, B. L.; Mirau, P.; Garrett, P. H.; Vaia, R. A. *J. Phys. Chem. B* **2006**, 110, 20143.
- (125) Kubies, D.; Jérôme, R.; Grandjean, J. *Langmuir* **2002**, 18, 6159.
- (126) Lorthioir, C.; Lauprêtre, F.; Soulestin, J.; Lefebvre, J.-M. *Macromolecules* **2009**, 42, 218.
- (127) Lonkar, S. P.; Morlat-Therias, S.; Caperaa, N.; Leroux, F.; Gardette, J. L.; Singh, R. P. *Polymer* **2009**, 50, 1505.
- (128) Purohit, P. J.; Wang, D. Y.; Emmerling, F.; Thünemann, A. F.; Heinrich, G.; Schönhals, A. *Polymer*, **2012**, 53, 2245.
- (129) Privalko, V. P.; Lipatov, Y. S.; Kercha, Y. Y. *Polym. Sci. U.S.S.R.* **1970**, 12, 1520.
- (130) Lipatov, Y. S.; Privalko, V. P. *Polym. Sci. U.S.S.R.* **1972**, 14, 1843.
- (131) Fragiadakis, D.; Pissis, P. *J. Non-Cryst. Solids* **2007**, 353, 4344.
- (132) Logakis, E.; Pandis, C.; Peoglos, V.; Pissis, P.; Stergiou, C.; Pionteck, J.; Potschke, P.; Miccaronuscaron, M.; Omastova, M. *J. Polym. Sci., Part B: Polym. Phys.* **2009**, 47, 764.

- 
- (133) Purohit, P. J.; Huacuja Sanchez, J. E.; Wang, D. Y.; Emmerling, F.; Thünemann, A.; Heinrich, G.; Schönhals, A. *Macromolecules* **2011**, *44*, 4342.
- (134) Wunderlich, B. *Prog. Polym. Sci.* **2003**, *28*, 383.
- (135) Homminga, D.; Goderis, B.; Dolbnya, I.; Groeninckx, G. *Polymer* **2006**, *47*, 1620.
- (136) Miltner, H. E.; Grossiord, N.; Lu, K.; Loos, J.; Koning, C. E.; van Mele, B. *Macromolecules* **2008**, *41*, 5753.
- (137) Mansfield, M.; Boyd, R. *J. Polym. Sci. Phys. Ed.* **1978**, *16*, 1227.
- (138) Schmidt-Rohr, K.; Spiess, H. W. *Macromolecules* **1991**, *24*, 5288.
- (139) Hu, W. G.; Boeffel, C.; Schmidt-Rohr, K. *Macromolecules* **1999**, *32*, 1611.
- (140) Schönhals, A. Molecular Dynamics in Polymer Model Systems. In: *Broadband Dielectric Spectroscopy*; Kremer, F.; Schönhals, A. Eds.; Springer: Berlin, Germany, **2002**, p 35.
- (141) Schönhals A, Kremer F. Theory of Dielectric Relaxation Spectra in *Broadband Dielectric Spectroscopy*; Kremer, F.; Schönhals, A. Eds.; Springer: Berlin, **2002**; p 99.
- (142) Wunderlich, B. *J. Chem. Phys.* 1962, *37*, 2429.
- (143) Tsuji, H.; Ikada, Y. *Polymer*, **1995**, *36*, 2709.
- (144) Pilla, S.; Gong, S.; O'Neill, E.; Yang, L.; Rowell, R. M. *Journal of Applied Polymer Science*, **2008**, *111*, 37.
- (145) Bello, A.; Laredo, E.; Grimaud, M. *Journal of Non-Crystalline Solids*, **2007**, *353*, 4283.
- (146) Klüppel, M.; Schuster, R. H.; Heinrich, G. *Rubber Chem. Technol.*, **1997**, *70*, 243.
- (147) Klüppel, M. *Adv Polym Sci*, **2003**, *164*, 1.
- (148) Jiang, X.; Bin, Y.; Matsuo, M. *Polymer*, **2005**, *46*, 7418.
- (149) Pötschke, P.; Dudkin, S. J.; Alig, I. *Polymer* **2003**, *44*, 5023.
- (150) Kremer, F.; Róžański, S.A. The dielectric properties of semiconducting disordered materials, In *Broadband Dielectric Spectroscopy*; Kremer, F.; Schönhals, A. Eds.; Springer: Berlin, **2002**; pp 475.
- (151) Debye, P.; Hückel, E. *Phys Z*, **1923**, *24*, 185.
- (152) Debye, P.; Falkenhagen, H. *Phys Z*, **1928**, *29*, 401.
- (153) Schönhals A, Goering H, Schick C, Frick B, Zorn R. *J. Non-Cryst. Solids* **2005**, *351*, 2668.

## Appendix

---

### List of Symbols

$A_0$	Constant of Vogel-Fulcher Tammann Hesse equation
$C^*(\omega)$	Complex capacitance
$D, D^*(\omega)$	Dielectric displacement, complex dielectric displacement
$E, E(\omega)$	Electrical field, periodical electric field
$E_A$	Activation energy
$f$	Dielectric frequency
$f_p$	Mean relaxation rate
$f_\infty$	Frequency pre-exponential factor
$G$	Shear modulus
$P$	Polarization (dielectric relaxation)
$P_\infty$	Induced polarization.
$R$	Organic side groups
$T$	Temperature
$T_g$	Glass transition temperature
$T_0$	Vogel temperature
$w_i$	Weighting factor
$\Delta\epsilon$	Dielectric strength
$C$	Concentration
$\epsilon^*(\omega), \epsilon', \epsilon''$	complex dielectric function, real part of the complex dielectric function and imaginary part of the complex dielectric function
$\epsilon_s$	Dielectric permittivity at time zero
$\epsilon_\infty$	Dielectric permittivity at infinite time
$\chi$	Dielectric susceptibility
$\delta(t)$	Dirac delta function

$\omega$	Angular frequency
$\tau_D, \tau_{CC}, \tau_{CD}, \tau_{HN}$	Relaxation time of Debye, Cole-Cole, Cole-Davidson and Haviriliak-Negami functions
$S(q)$	Structure factor
$P(q)$	Form factor
$\rho_d$	Density of atoms
$d$	Distance between two LDH sheets
$l_c$	LDH stack size
$w$	Width of x-ray reflection peaks
$q_{peak}$	Peak position of x-ray reflections
$t, s$	Exponents
$C_c$	Percolation concentration threshold
$\sigma^*, \sigma', \sigma''$	Complex conductivity, real and imaginary part of complex conductivity
$\sigma_{DC}$	Direct current conductivity
$I_{amorphous}$	Area below amorphous halo
$I_{crystallinity}$	Area below crystalline reflection
$A_T$	Temperature amplitude
$T_c$	Crystallization temperature
$T_m$	Melting temperature
$\Delta H$	Enthalpy
$\Delta C_p$	Thermal relaxation strength
TSDC	Thermally stimulated depolarization current
DC	Direct current

## List of Abbreviations

LDH	Layered double hydroxide
-----	--------------------------

U-LDH	Unmodified LDH
O-LDH	Organically modified LDH
MWNT	Mutli-walled carbon nanotubes
SWNT	Single-walled carbon nanotubes
DWNT	Double-walled carbon nanotubes
CNT	Carbon nanotubes
ATR-IR	Attenuated total reflection infrared spectroscopy
BDS	Broadband dielectric relaxation spectroscopy
CC	Cole-Cole function
CD	Cole-Davidson function
CRR	Cooperative rearrange region
DSC	Differential scanning calorimetry
TMDSC	Temperature modulated differential scanning calorimeter
SSDSC	Stepscan differential scanning calorimetry
FTIR	Fourier transform infrared spectroscopy
SAXS, WAXS	Small- and wide- angle X-ray scattering
SDBS	Sodium dodecyl benzenesulfonate
RAF	Rigid amorphous fraction
HN	Haviriliak-Negami function
DMA	Dynamic mechanical analysis
MWS	Maxwell Wagner Sillars polarization
NMR	Nuclear magnetic resonance
PMMA	poly (methyl methacrylate)
PP	Polypropylene
PE	Polyethylene
PLA	Polylactide

PS	Polystyrene
VFTH	Vogel-Fulcher-Tammann-Hesse equation
TEM	Transmission electron microscopy
IPF	Leibniz Institute for Polymers Research, Dresden, Germany
XRD	X-ray diffraction

### List of Constants

R	Ideal gas constant = 8.314 J/mol/K.
i	Complex unit = $\sqrt{-1}$ .
$\epsilon_0$	Dielectric permittivity of free space = $8.85 \cdot 10^{-12}$ As/V/m.

## **Publications from this work:**

### **Peer-reviewed Journals**

- 1) **P. J. Purohit**, J. H. Sánchez, D. Y. Wang, F. Emmerling, A. F. Thünemann, G. Heinrich and A. Schönhals\*, Structure property relationships of Nanocomposites based on Polypropylene and Layered Double Hydroxide, **Macromolecules**, 2011, 44, 4342-4354.
- 2) **P. J. Purohit\***, D. Y. Wang, F. Emmerling, A. F. Thünemann, G. Heinrich and A. Schönhals, Arrangement of layered double hydroxide in a polyethylene matrix investigated by a combination of complementary methods, **Polymer**, 2012, 53, 2245-2254.
- 3) **P. J. Purohit**, J. H. Sánchez, D. Y. Wang, A. Wurm, C. Schick, M. H. Wagner and A. Schönhals, Detailed comparison of Thermal and Dielectric investigations of Nanocomposites based on Polypropylene and Layered Double Hydroxide, **Macromolecules**, **To be submitted**.
- 4) **P. J. Purohit**, D. Y. Wang, F. Emmerling, A. F. Thünemann, G. Heinrich, M. H. Wagner and A. Schönhals, Structure property relationships of Nanocomposites based on Polylactide and Layered Double Hydroxide, **In preparation**.

### **Conference (Talks)**

- 1) **P. J. Purohit**, J. H. Sánchez and A. Schönhals, Structure property relationships of Nanocomposites based on Polypropylene and Layered Double Hydroxides, Dielectric Bazaar, 6<sup>th</sup> International Conference on Broadband Dielectric Spectroscopy and its Applications, Madrid, Spain, September 2010.
- 2) **P. J. Purohit**, J. H. Sánchez and A. Schönhals, Structure property relationships of Nanocomposites based on Polypropylene and Layered Double Hydroxides, Spring Meeting, German Physics Society (DPG), Dresden, Germany, March 2011.
- 3) **P. J. Purohit** and A. Schönhals, Structure-Property relationships of nanocomposites based on Polyolefins and Layered Double Hydroxide, Eurofillers, Dresden, Germany, August 2011.
- 4) **P. J. Purohit** and A. Schönhals, Structure property relationships of nanocomposites based on Polylactide and Layered Double Hydroxide, International Multicomponent Polymer Conference, Kerala, India, March 2012.



### Conference (Posters)

- 1) **P. J. Purohit** and A. Schönhals, Dielectric investigation of Nanocomposites based on Poly(methyl methacrylate) and Polyhedral Oligomeric Silsesquioxanes, Spring Meeting, German Physics Society (DPG), Regensburg, Germany, March 2010.
- 2) **P. J. Purohit** and A. Schönhals, Structural investigation of Nanocomposites based on Poly(methyl methacrylate) and Polyhedral Oligomeric Silsesquioxanes, 6<sup>th</sup> International Conference on Broadband Dielectric Spectroscopy and its Applications, Madrid, Spain, September 2010.
- 3) **P. J. Purohit**, J. H. Sánchez and A. Schönhals, Structure property relationships of Nanocomposites based on Polyethylene and Layered Double Hydroxides, Spring Meeting, German Physics Society (DPG), Dresden, Germany, March 2011.
- 4) **P. J. Purohit** and A. Schönhals, Structure property relationships of nanocomposites based on Polylactide and Layered Double Hydroxide, German Physics Society (DPG), Berlin, Germany, March 2012.
- 5) **P. J. Purohit** and A. Schönhals, Investigations of nanocomposites based on Polylactide and Layered Double Hydroxide, Broadband dielectric society International conference, Leipzig, Germany, September 2012.

### Other Publications (not related to this work):

#### Book Chapter

- 1) Advances in Polyolefin Nanocomposites, Chapter 8: Polyolefin Nanocomposites with Layered Double Hydroxide, D. Y. Wang, F. R. Costa, A. Leuteritz, **P. J. Purohit**, A. Schönhals, A. Vyalikh, U. Scheler, U. Wagenknecht, B. Kutlu and G. Heinrich, CRC Press, 2011.

#### Peer-reviewed Journals

- 1) M. Ramanujam, V. Wachtendorf, **P. J. Purohit**, R. Mix, A. Schönhals, J. F. Friedrich, A detailed dielectric relaxation spectroscopy study of artificial UV weathered low density polyethylene, **Thermochimica Acta**, 2012, 530, 73-78.
- 2) **P. J. Purohit**, H. Yin, J. Falkenhagen and A. Schönhals, Dielectric investigation of Nanocomposites based on Poly(methyl methacrylate) and Polyhedral Oligomeric Silsesquioxanes, **European Polymer Journal**, To be submitted.

### Conference (Posters)

- 1) A. Schönhals and **P. J. Purohit**, Structure-Property Relationships of Polyolefine based Nanocomposites with Layered Double Hydroxides - Interplay between Matrix and

Interfacial Effects, **Presentation**, 3<sup>rd</sup> Annual Meeting VAMA TWA-33 (Polymeric Nanocomposites), Istanbul, Turkey, October 2010.

2) M. Füllbrandt, **P. J. Purohit**, and A. Schönhals, Dielectric and Thermal investigation of adsorbed Poly(vinyl acetate) on Silica particles, **Poster**, Spring Meeting, German Physics Society (DPG), Dresden, Germany, March 2011.

3) M. M. Sadeghi, **P. J. Purohit**, A. Bertin, M. Böhning and A. Schönhals, Dielectric Investigation of Nanocomposites based on Polystyrene and Polyhedral Oligomeric Silsesquioxanes, **Poster**, German Physics Society (DPG), Berlin, Germany, March 2012.

## **Declaration of Authorship**

I hereby confirm that I have authored this PhD Thesis independently and without use of other than indicated sources.



Purv J. Purohit

Berlin, 13.09.2012

## Curriculum Vitae

### Personal:

Name: Purv J. Purohit  
Date of Birth: 26<sup>th</sup> December 1983  
Place of Birth: Mumbai, India  
Nationality: Indian

### Education:

06/1986 – 03/1999	St. Francis D'Assisi High School, Mumbai, India.
09/1999 – 06/2003	SBM Polytechnic, Mumbai, India. Diploma in Plastics Engineering
09/2003 – 06/2006	MIT, University of Pune, India. Bachelor in Polymer Engineering
10/2007 – 08/2009	Joint program of Free University, Humboldt University, Technical University Berlin and University of Potsdam, Germany. Masters in Polymer Science
11/2009 – 08/2012	BAM Federal Institute for Materials Research and Testing, Berlin, Germany. PhD in Polymer Science
From 09/2012	Development Engineer at Clear Edge Filtration GmbH Geldern-Walbeck, Germany.